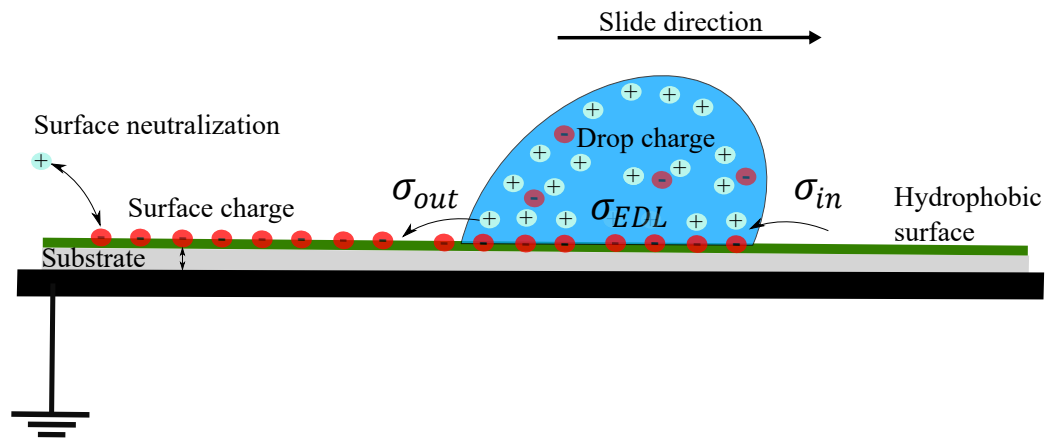


SOLID-LIQUID CONTACT ELECTRIFICATION IN SLIDING DROPS



Dissertation

zur Erlangung des Grades

"Doktor der Naturwissenschaften"

am Fachbereich Physik, Mathematik, Informatik

der Johannes Gutenberg-Universität

in Mainz

Pravash Bista

geboren in Kathmandu, Nepal

Mainz, den 07. Juni 2024

The presented work on solid-liquid contact electrification, also known as slide electrification, was supervised by Apl. Prof. Dr. Stefan Weber from March 2021 to August 2024 at the Max Planck Institute for Polymer Research.

Berichterstatter: Apl. Prof. Dr. Stefan Weber

*"The highest education is that which does not merely give us information but makes our life in harmony with all existence."
Rabindranath Tagore (1861-1941)*

Abstract

A surface in contact with a liquid is known to form an electric double layer EDL, consisting of fixed charges at the surface and a diffuse layer in the liquid. Recently, it has been observed that the moving contact line atop a hydrophobic surface can deposit some of these charges from the EDL onto the surface, leading to charge separation, also known as contact charge separation. The charge separation between the inclined hydrophobic surface and the sliding drops is known as *slide electrification*, where moving drops leave behind some surface charge. In doing so, the drops accumulate an equal and opposite charge. Lately, such charge separation processes have been utilized for energy harvesting. Furthermore, it has been shown that these separated charges can influence the motion of the sliding drop as well as the dynamic contact angle. Nevertheless, the physical understanding of the charge separation process is not complete.

This dissertation introduces two novel experimental setups to determine the relevant physical parameters in slide electrification. The *super probe* method measures the drop potential of sliding drops after a certain slide length. We use this setup to quantify the drop potential dependence on slide length and drop interval. The *subsurface probe* method measures the capacitive current resulting from charge separation. This allows us to quantify the charge separation at the receding contact line and measure surface neutralization/discharge time, which refers to the time it takes for the surface to recover by losing charges between drops, either through the substrate or the surrounding environment.

Moreover, based on the experimental observations, we develop a comprehensive model to describe the behaviour of multiple drops sliding over an inclined hydrophobic surface. The model explores the physical and chemical processes involved in building the EDL and reveals the relationship between the EDL and slide electrification. We demonstrate that charge separation occurs at the receding contact line and derive a simple relationship illustrating the dependence of charge separation on the drop charge. We find that as the drop slides down the substrate, the drop's charge compensates for

the surface charge in the EDL. When the drop charge completely compensates for the surface charge, the drop potential can reach up to kilovolts. Our model reveals that this drop potential is an amplification of the surface/zeta potential. Furthermore, we show that the substrate, along with the surrounding environment, plays a vital role in the surface neutralization time. We provide a method to determine this surface neutralization time and incorporate it into the model to describe the drop charge dependence in the drop interval.

The physical insights into slide electrification from this work provide a new window into the EDL at the solid-liquid interface. Similarly, a better understanding of the surface neutralization process helps improve the conversion of a sliding drop's kinetic energy into electrical energy.

Contents

1	Introduction	1
1.1	Overview	1
1.2	Motivation	5
1.3	Outline	9
1.4	Publications associated with this dissertation	10
2	Physical Concepts in Surface Science	11
2.1	Interface & Wetting	11
2.1.1	Surface Tension	12
2.1.2	Young-Laplace Equation	13
2.1.3	Wetting	15
2.1.4	Young’s Equation	15
2.1.5	Dynamic wetting	17
2.2	Interface & Electric double layer (EDL)	18
2.2.1	Helmholtz model	19
2.2.2	Gouy-Chapman model	20
2.2.2.1	Poisson–Boltzmann statistics of diffuse layer	20
2.2.3	Stern model	23

2.2.4	The Grahame's Equation	23
2.3	Slide electrification	24
3	Methodology	27
3.1	Electrical concepts	27
3.1.1	Electrostatics	27
3.1.2	Sensing electrical current	29
3.2	Experimental setups	31
3.2.1	Discharge current measurement	32
3.2.2	Drop voltage measurement	33
3.2.3	Mirror charge method	34
3.2.4	Numerical simulation of capacitive current	35
3.2.5	Capacitance measurements	37
3.3	Sample preparation	38
4	Parameter Exploration with Tilted Plate Experiments	40
4.1	Slide length dependent drop charge	40
4.2	Drop interval dependent drop charge	41
4.3	Surface chemistry dependent drop charge	42
4.4	Summary	44
5	Physical Model for Slide Electrification	45
5.1	Two capacitor model	45
5.2	Origin of Three-phase contact line voltage	48

5.2.1	Deriving the relation between drop charge/voltage potential and surface potential	48
5.2.2	Surface Potential beyond the linear approximation	51
5.3	Measuring surface potential	52
5.3.1	Influence of substrate thickness and salt concentration	54
5.3.2	Surface potential of different surfaces	55
5.4	Series of drop sliding down the surface	56
5.4.1	Numerical simulation	58
5.5	Energy harvesting	59
5.6	Summary	60
6	Charge Transfer Coefficient (α)	61
6.1	Quantifying surface charge densities	62
6.1.1	Surface charge density on EDL (σ_{EDL})	62
6.1.2	Surface charge density left on dry surface (σ_{out})	62
6.2	Quantifying charge transfer coefficient (α)	64
6.2.1	Charge transfer coefficient (α) behaviour with drop velocity	65
6.2.1.1	Experimental results	66
6.2.2	Charge transfer coefficient (α) behaviour with salt concentration	67
6.3	Summary	67
7	Surface Charge on Dewetted Surface & Charge Retention	69
7.1	Surface charge density (σ_{out})	70
7.2	Surface neutralization/discharge time	72
7.3	Surface charge decay length(L_{sat})	76

7.4 Summary	78
8 Conclusion & Outlook	79
Bibliography	92
List of Figures	98
Appendix	99
Curriculum vitae	101

Chapter 1

Introduction

1.1 Overview

Imagine a cold and dry winter day. You are working in your office when, out of nowhere, your colleague calls out from the lab, asking for your assistance. You rise from your chair and make your way to the door. Upon touching the door handle, a sudden electric shock goes through your fingertips. What happened? The reason is the triboelectric effect. While you walk to the door, your shoes make contact with the carpet, causing a charge separation that electrifies your body. All of a sudden, when you touch the door handle to open the door, your body discharges, giving you the sensation of an electric shock. This is a day-to-day example of the solid-solid triboelectric effect [1, 2]. But what if a liquid comes in contact with a solid? Is there charge separation in solid-liquid contact? If so, what is the physical mechanism behind this? Inspired by these questions, I studied the charge separation as polar liquid like water slide over a hydrophobic surface and explored the physical mechanism behind the process. We found that charge separation begins at the solid-liquid interface, where the surface in contact with the liquid gets charged forming an Electric Double Layer EDL, in the process. Furthermore, we discovered that various factors such as the coating, substrate, surrounding environment, and the velocity of the sliding drop significantly influence this charge separation process, which we will discuss in detail in this dissertation. We refer to the entire process of solid-liquid contact electrification in sliding drops as slide electrification.

The first account of static charging of objects was reported by the Greek philoso-

pher Thales of Miletus¹ around 600 B.C. He rubbed amber (also known as "elektron" in Greek) and observed that it could attract light objects like feathers [3]. Due to his findings with amber (elektron), we continue to use the terms "electricity" and "electric charge." At that time, the exact understanding of charge and electricity was lacking. However, through his observations, Thales of Miletus laid the foundation for the understanding of electricity and charge separation.

Continuing the exploration of electric charge, English physicist Stephan Gray² worked with static charging in the 1700s and demonstrated that not only can charges be created, but they can also be transferred [4]. He showcased this through his famous 'flying boy' experiment, where he suspended a boy using silk cords. By charging the suspended boy with static electricity, Stephan Gray demonstrated that another person in close proximity could also feel the electric charge and that electricity could be conducted. He divided objects into conductors, which transfer electricity, and insulators, which do not transfer electricity.

Approximately 150 years after Stephan Gray's contributions, a significant observation of solid-liquid and liquid-liquid charge separation was reported by P. Lenard³ in 1892. In his work, Lenard documented the negative charging of the air around a waterfall and the positive charging of the falling water [6]. Specifically, he noticed that the air had a higher concentration of negative charges around the base of the waterfall, where the splashing water droplets made contact with the rocks. Another example of water charging up is the thunderstorm and lightning, which was studied by J. Nolan et al. [7] in early 1900s. One of the first observations of surface charging due to the moving aqueous solution was made by Eliot F. Porter and Jeffries Wyman, Jr. in 1938 [8, 9]. In the same year, Irving Langmuir⁴ discussed three possible mechanisms for their observation, including the internal dipole of the film, surface charge due to dewetting of the contact line, and volume charge [10]. Since then, charging of liquid drops has captivated scholars for two main reasons, firstly the wish to understand the basic interaction of liquid and solid, and secondly because of the possibility of using such electrification in energy harvesting. Nevertheless, the physical process behind such solid-liquid contact charge separation is not fully understood.

The mechanisms proposed to describe solid-solid contact charge separation are electrification via contact-friction [11, 12] and/or via the ion separation at contact interfaces [13] as there is high shear stress at few asperities. But, the same mechanism

¹Thales of Miletus, 624–546 BCE, Greek philosopher.

²Stephan Gray, 1666 – 1736, English physicist.

³Philipp Lenard. 1862–1947. German physicist.

⁴Irving Langmuir, 1881–1957, American chemist and physicist.



Figure 1.1: Experimental illustration of the flying boy experiment conducted by Stephan Gray [5]

can not be used to describe solid-liquid contact electrification because there is no high enough shear stress at the solid-liquid contact interface due to deformability of liquid [14]. Arranging a series of materials from the most positively charged to the most negatively charged as they become triboelectrically charged by contacting each other is called the triboelectric series. The position of water in the triboelectric series between air and glass, as shown by Burno et al. [15], inspires the investigation of solid-liquid charge separation.

In 1993 and 1996, motivated by the electrification of semiconductors during the process of washing and rinsing with water, K. Yatsuzuka et al. [16, 17], Matsui et al. [18], and Yaminsky et al. [19] studied the charge separation of ultrapure water

drops sliding on a polymer surface. They observed spontaneous positive charging of moving drops and the accumulation of negative charge on the polymer surface. They also demonstrated that the separation of charges between the solid and liquid phases depended on several parameters, such as polymer surface, slide length, liquid conductivity, falling height, and environmental conditions. While their qualitative observations were influenced by various parameters, a quantitative understanding of the ions absorbed by the polymer surface was lacking.

Similar solid-liquid charge separation phenomena were subsequently reported by Stetten et al. [14] and Lin et al. [20] in more recent times. These authors improved the experimental setups and attempted to introduce physical models to describe the charge separation process. Here, it is assumed that the charge is separated during the motion of the three-phase contact line, and some charge remains on the solid surface, resulting in the charging of the sliding drop.

Solid-liquid charge separation is not limited to sliding drops; it is relevant in numerous scenarios. For example, charging in micropipetting could play an important role in chemical and biological labs [21, 22]. In the case of aerosols, the charging in nano and micro droplets could play a crucial role in virus and bacterial transfer [23]. Additionally, in agricultural spraying, where the charging can influence the effectiveness of insecticides and pesticides because of its influence on the spreading of the liquid [24]. This emphasizes the significance of solid-liquid charge separation in the realm of chemical and biological studies.

Furthermore, solid-liquid charge separation has also been observed in bouncing or splashing of drops [25, 6, 26, 27, 28, 29]. Díaz et al. [30] reported that the receding contact line and the contact area play an important role in charge separation. Moreover, it can even influence the bounce of a drop due to the electrostatic forces between the charged drop and the solid surface [31].

Experimental evidence suggests that in most cases, glass coated with hydrophobic hydrocarbon and silane surfaces obtains a negative charge, while sliding drops acquire a positive charge. In 2008, N. Kudin et al. [32] conducted molecular dynamic simulations of such hydrophobic surfaces with hydroxide and hydronium ions. They proposed that due to the asymmetry in molecular charge distribution in hydroxide and hydronium ions, one side of the molecule becomes hydrophilic while the other side becomes hydrophobic. They suggest that this effect is more pronounced for hydroxide ions, potentially explaining the negative charging of the surface due to the presence of hydroxide ions on its surface. Similarly, Artemov et al. [33] conducted molecular dynamic simulations and suggested that the quantity and polarity of ions near the

surface depend on the type of surface. Their simulation shows that ion absorption minima are deeper near Teflon, and the hydroxide ions are closer to the surface compared to the hydronium ions. In contrast, they observed weak absorption on Kapton surfaces.

Experimentally, Zimmermann et al. [34], and Sosa et al. [35, 36] also suggested that the ion transfer dominates the solid-liquid contact electrification. Sosa et al. presented a model that uses ion exchange and acid-base equilibrium to describe the charge separation. Through this model, they aim to explain the pH-dependent nature of charge separation. Notably, they managed to successfully fit surface charge density, zeta potential, and acid-base titration with changes in pH with the same set of parameters. Moreover, the model even predicted the existence of a point of zero charge, matching well with experimental findings. Another reason to believe the ions are dominating the charge separation is the observation of concentration dependence, which shows a decrease in charge separation with increasing concentration [22, 37, 38].

Studies addressing the question which specimen is responsible for charge separation also do not consent to one particular process. Wang et al. suggest that electron transfer is the dominating factor in contact charge separation [20, 39, 40]. While the majority of the community believes ions play a significant role, the ongoing debate regarding whether it involves ions, electrons, or a combination of both remains to be addressed.

1.2 Motivation

Energy harvesting

Solid-liquid charge separation get increased attention in recent years due to its potential application in energy harvesting. Such devices are called Solid-Liquid Triboelectric nanogenerators (SL-TENGs). SL-TENGs typically involve two types of setups. First one involves a metal electrode is positioned underneath the surface. As drops slide down this surface, some charges are left behind, causing the drops to acquire opposite charges. This, in turn, induces a capacitive current in the metal electrode, which is then utilized for electric energy harvesting (Fig. 1.2a) [41, 42, 43, 44, 45]. One advantage of such a device is that it does not disturb the sliding drop and can be implemented in various locations, such as rooftops and solar panels. However, a drawback is that the induced current is bipolar, and the maximum potential for power generation is not achieved. The second type of devices involves directly probing the drop potential by

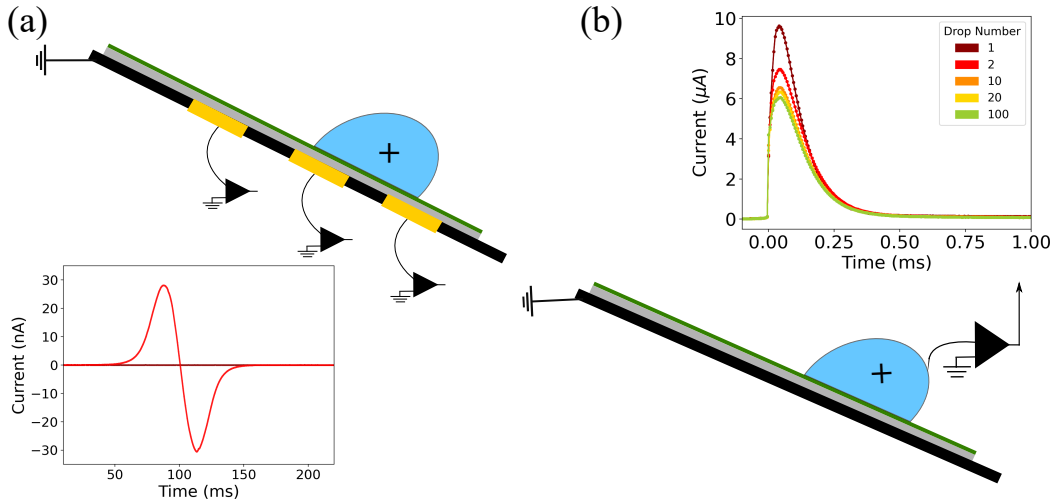


Figure 1.2: Two different types of energy harvesting methods using slide electrification. (a) The figure illustrates a way to harvest electric energy in the form of induced current. (b) The figure demonstrates a method to harvest electric current by directly discharging the drop.

either touching the drop or collecting them in a Faraday cup [46, 47, 48, 49, 50, 51] (Fig. 1.2b). While this method may not be applicable everywhere, it offers the potential for much higher current generation than the capacitive current method. Simple comparison shows that the capacitive current is in the range of nA , whereas the direct method produces the direct current in the range of μA . Nevertheless, both of these techniques can be used for different scenarios or combined to create an energy harvesting device.

Although SL-TENGs produce a very small amount of energy, this could be extremely useful for applications in nanofluidics [52, 53, 54], electrochemical power systems [55, 56], and emerging low-power devices like the Internet of Things (IoT). These devices need to run continuously, but only require a small amount of energy. Feng et al. have even proposed a temperature monitoring device powered by solid-liquid contact electrification [57]. Similarly, Shen et al. have shown that contact electrification can also be used for monitoring human health by tracking sweat [58]. Therefore, a good understanding of the physical mechanism of solid-liquid charge separation is needed to advance its applicability.

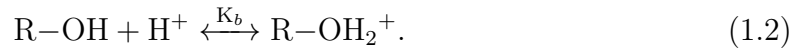
Gap of knowledge

Although the solid-liquid charge separation phenomenon is observed almost everywhere and are being optimized for energy harvesting, there are not many studies being done to understand the fundamental physics behind the process.

Due to the simultaneous influence of multiple variables—such as the type of liquid, drop size, solid surface characteristics, drop velocity, contact angle, contact area, and environmental conditions—on charge separation, conducting a quantitative study becomes challenging. For instance, when the drop velocity is increased, it concurrently reduces the receding contact angle while increasing drop friction [59]. As a result, an experimental setup and methods are required to disentangle these distinct effects and individually examine the relevant factors.

One simple way to study slide electrification is to measure the discharge current of a drop sliding down a tilted hydrophobic plate [14, 40, 20, 60]. Using this method, Stetten et al. [14] observed that the drop charge saturates after a few cm, and it depends on drop-number and drop interval. Wong et al. [61] also discovered the influence of surface chemistry on charge separation.

In water or high dielectric liquids, most solid surfaces are charged. This surface charge forms spontaneously, e.g. by the adsorption of ions from solution, by protonation or deprotonation of surface groups or the preferential dissolution of ions, leading to the formation of EDL [62, 63]. An example of protonation/deprotonation on the active sites (R) on the surface can be written as follows [36, 64]:



As water comes into contact with the surface, deprotonation and protonation occur, as shown in equations (1.1) and (1.2). These processes reach an equilibrium state within a few microseconds [65], and the equilibrium constants K_a and K_b determine the surface charge density and the point of zero charge (PZC), where the surface charge density is zero. The charged interface gives rise to the electrostatic potential difference between the interface and the bulk, also known as the surface potential Φ . Meanwhile, the potential in the presence of a shear flow of the liquid is defined as the ζ -potential [66, 67].

In the charge separation model discussed in this dissertation, we assume that some of the charge from the EDL is pinned to the solid surface as the receding contact line

moves. Thermodynamically, the probability of ions staying in a liquid is much higher than on a dry-solid surface [14]. Nevertheless, both drop and surface charging have been observed in different experiments [40, 20, 60, 11, 35, 36, 61, 68, 49, 57, 51]. Therefore, we assume that the pinned charges might be surrounded by a hydration cell. The magnitude of pinning depends on the charge already accumulated by the drop and the pre-existing surface charge, e.g. left behind from previous drops. Recently, our study of charge transfer mechanism at receding contact lines and its parametric dependencies were described theoretically [64]. This analysis reveals that charge exchange depends on drop velocity and the receding contact angle during the dewetting.

Although much progress has been made in recent years in understanding slide electrification, there are still some open questions. Here, we will address three of these research questions listed below and illustrated in figure 1.3.

- **Question 1:** What is the connection between the EDL and the slide electrification?
- **Question 2:** What amount of charge is left on the solid surface?
- **Question 3:** What factors influence the charge retention on the surface and surface neutralization?

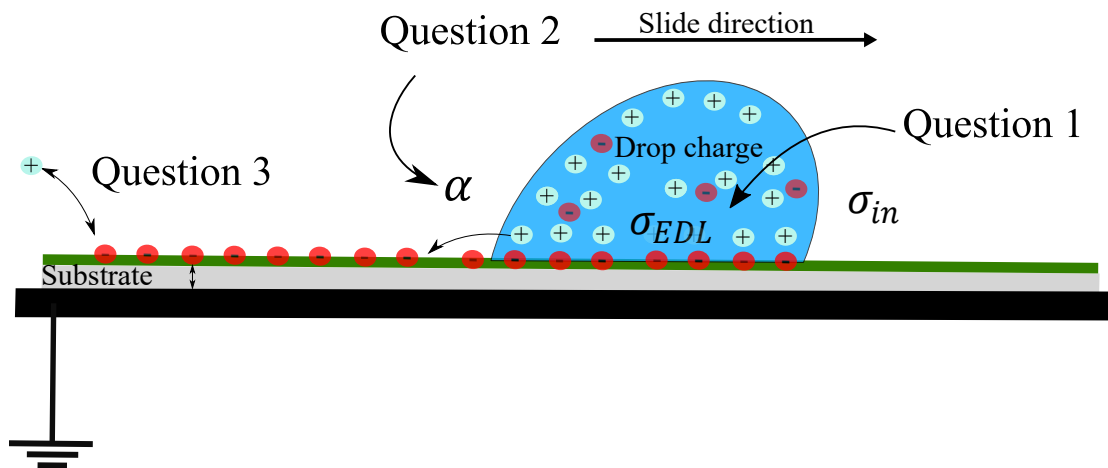


Figure 1.3: Illustration showing the gap in knowledge

Within this study, we explore the relationship between charge/voltage accumulation in sliding drops and physicochemical surface properties, specifically focusing on the surface potential Φ , in EDL. We will discuss methods for quantifying the drop's

voltage/charge on hydrophobized substrates. These measurements reveal drop voltages exceeding kilovolts in a drop-substrate capacitor with a capacitance of pF . The high potential can be explained by examining electrostatic fields at the solid-liquid interface, establishing the connection between drop voltage/charge and surface potential. Consequently, the measurement of the saturated drop charge/voltage enables the determination of the surface potential at the solid-water interface.

Furthermore, we investigate the assumption that a certain percentage α , of the surface charges from the EDL remains on the surface as the receding contact line moves. To accomplish this, we will present a method for quantifying α . Additionally, we will utilize the mirror or capacitive charge method to locally measure the solid-liquid charge separation as the contact line moves over the surface. We will study the surface charge, its neutralization process, and the neutralization timescale by employing a grounded drop sliding down the surface.

1.3 Outline

In chapter 2, we delve into the fundamentals of physics at interfaces. This chapter covers the interactions between liquids and solids, exploring surface and interface, three-phase contact lines, contact angles, and electrostatic interactions. Additionally, we examine the existing model used to describe slide electrification.

In chapter 3, we introduce different methods to measure charge separation, namely drop (*super probe*) and surface (*subsurface probe*) charge. For measuring drop charge, we use the direct discharge method, where we measure the drop charge and/or voltage by touching the sliding drop after a certain slide length. To measure surface charge, we use the mirror charge detection method based on capacitive current. Here, a mirror charge is induced in the probe electrode beneath the substrate as the drop slides above the probe electrode. Integrating the capacitive current during this process, we estimate the local charge density atop the electrode.

In chapter 4, we will discuss the experimental observations to establish the relevant parameters. The experiments show that the drop charge depends on slide length, drop number, drop interval, and surface chemistry. These relevant parameters will be the backbone of the theoretical model introduced in this dissertation to describe slide electrification.

In chapter 5, we will present an electronic model to describe the slide electrification,

and discuss the parameters involved in slide electrification. we will further explore the connection between the high voltage generated in slide electrification and surface potential. The results presented here were published in *High voltages in sliding drops* [38].

In chapter 6, we will present a method to quantify the transfer coefficient α , which is the ratio between the surface charge density σ_{out} , left by the sliding drop and the total surface charge density σ_{EDL} , in the EDL. Here, we will first derive an equation to estimate σ_{EDL} using the drop potential. Then, we will introduce a way to quantify σ_{out} using the tail current and the drop velocity. Finally, we will study the transfer coefficient's dependence on different parameters such as velocity and salt concentration. Parts of this chapter are published in *How charges separate when surfaces are dewetted* [64].

In chapter 7, we discuss the surface charge density as a drop dewets the surface. we use the mirror charge method to measure the point of charge separation, the amount of charge left on the surface, and the charge retained by the surface. The results presented here were published in *Surface Charge Density and Induced Currents by Self-Charging Sliding Drops* [69].

In chapter 8, I present the summary of the dissertation, important scientific findings, its shortcomings, and the outlook of the project.

1.4 Publications associated with this dissertation

- **P. Bista**, A. D. Ratschow, Amy. Z. Stetten, H.-J. Butt, and S. A. Weber, "Surface Charge Density and Induced Currents by Self-Charging Drops," *Soft Matter*, 2024.
- **P. Bista**, A. D. Ratschow, H.-J. Butt, and S. A. Weber, "High voltages in sliding water drops," *The Journal of Physical Chemistry Letters*, vol. 14, pp. 11110–11116, 2023.
- A. D. Ratschow, L. S. Bauer, **P. Bista**, S. A. Weber, H.-J. Butt, and S. Hardt, "How charges separate when surfaces are dewetted," *Physical Review Letters* 132.22 (2024): 224002.
- W. S. Wong, **P. Bista**, X. Li, L. Veith, A. Sharifi-Aghili, S. A. Weber, and H.-J. Butt, "Tuning the charge of sliding water drops," *Langmuir*, 2022.

Chapter 2

Physical Concepts in Surface Science

To understand slide electrification, we need to consider various physical and chemical concepts, such as interface, surface tension, and the Young-Laplace theory describing the shape of liquids. Additionally, it is crucial to understand Young's equation, the three-phase contact line, and the surface charge density at the solid-liquid interface. Here, we briefly explore the concepts of the solid-liquid interface based on the theory presented in the book *Physics and Chemistry of Interfaces* by Hans-Jürgen Butt, Karlheinz Graf, and Michael Kappl [63].

2.1 Interface & Wetting

The three fundamental states of matter are gas, liquid, and solid phases [70]. In the gas phase, molecules experience minimal attraction to one another, allowing them to move freely and mix. Hence, there is no interface. In the solid phase, molecules are tightly bound through covalent and metallic bonds. Initially, one might think there is no interface within the solid, but the boundaries between different crystal orientations can create interfaces within the solid. The liquid phase, situated between the solid and gas phases, is characterized by molecular interactions driven by forces such as Van der Waals forces (dipole-dipole interactions between molecules) [71] and hydrogen bonds (interactions between partially negatively charged molecules and protons) [72]. These relatively weak intermolecular attractions allow liquids the unique ability for molecules to move within the liquid. Because of its unique position between solid and liquid, liquids can form interfaces between both solid and gas. The interface between liquid-gas or solid-gas is known as the surface.

2.1.1 Surface Tension

Liquid bodies at equilibrium seek to attain a state of minimum energy [73]. At equilibrium, drops tend to adopt shapes with the lowest surface area-to-volume ratio, typically spherical geometry in the absence of gravity [74]. A liquid body can be divided into two regions: the bulk, where molecules are surrounded by similar molecules and experience balanced intermolecular forces, and the interface/surface. At the interface, molecules experience an attractive force from the bulk, but there's no opposing force (see Fig. 2.1a). This results in an unfavourable state for the molecules at the interface. To minimize this energy penalty, the liquid reduces its surface area. The energy required to create the surface is known as surface tension.

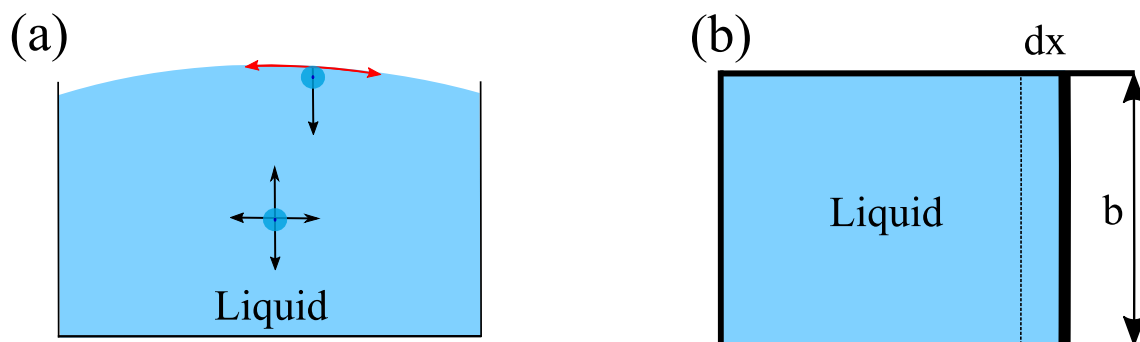


Figure 2.1: (a) Graphical illustration of surface tension (b) Empirical law to obtain surface tension

Mathematically, surface tension can be described as the work dW , required to change the surface area dA .

$$dW = \gamma dA. \quad (2.1)$$

The surface tension, denoted by γ , is the proportionality constant between applied work and change in area. Surface tension is independent of the area but still varies with temperature, pressure, and composition of liquid and vapour [73].

Another way to estimate surface tension is by using the force F , that holds a liquid body together. This interpretation allows for a simple calculation of surface tension. Here, one needs to apply a force to maintain the surface area and can calculate surface tension using the applied force with the equation $\gamma = -\frac{F}{2b}$. A typical example of the surface tension of water at room temperature is 72 mN/m. This value decreases with increasing temperature due to the increase in thermal energy, which makes it easier for molecules to move. The surface tension of water at 100 °C is 58.8 mN/m [75].

2.1.2 Young-Laplace Equation

As mentioned above, a liquid body, in the absence of gravity, attempts to decrease its surface area to overcome the energy penalty and achieve a spherical shape. In the presence of gravity, we observe the liquid body forming a flat surface. But how can we physically describe the shape of a liquid body? Young¹ and Laplace² came up with an elegant way to relate the pressure difference between the bulk and the exterior of the liquid to its shape and curvature.

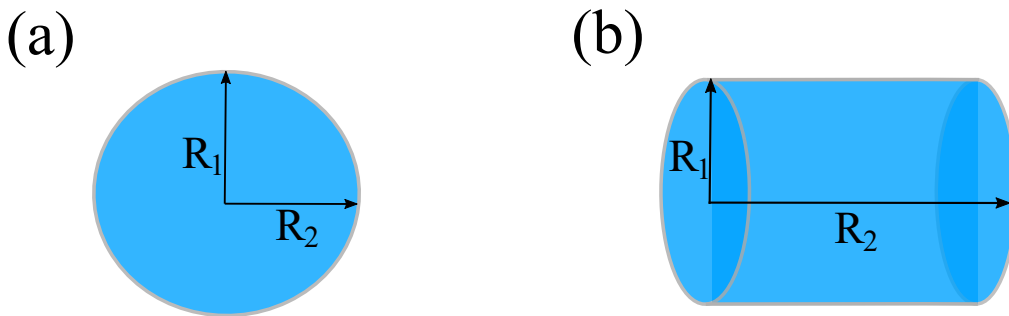


Figure 2.2: (a) Illustration of principal radii in the case of a spherical object (b) a cylindrical object

The Young-Laplace equation relates the pressure difference ΔP and the principal radii (R_1 and R_2) of curvature:

$$\Delta P = \gamma \left(\frac{1}{R_1} + \frac{1}{R_2} \right). \quad (2.2)$$

Here, the proportionality constant γ is the surface tension of the liquid. The principle radii are perpendicular to each other and intersect the normal drawn at the surface of the object/liquid. In the case of a spherical shape, the principal radii are equal to the radius, denoted as R ($R_1 = R_2 = R$), which results in a curvature of $2/R$. However, in the case of a cylinder, one of the principal radii $R_1 = R$, represents the radius of the circle making up the cylinder, while R_2 is infinity, yielding a curvature of $1/R$.

In the presence of gravity, the Young-Laplace equation must be extended using the hydrostatic pressure ρgh . Here, ρ is the liquid density g is the gravitational acceleration, and h is the height of the liquid body.

But when should we include or neglect gravity? This can be estimated using the Bond number [76], which is the ratio of hydrostatic force to capillary force and is given

¹Thomas Young, 1773–1829, English physicist.

²Pierre Simon Marquis de Laplace, 1749–1827, French physicist.

by:

$$B_n = \frac{\Delta\rho g l^2}{\gamma}. \quad (2.3)$$

Here $\Delta\rho$ represents the difference in density between two phases, and l is the characteristic length scale. In the case of a drop, l would represent the radii of curvature.

When $B_n \ll 1$, we can neglect the effect of gravity, and interfacial forces dominate. Whereas when $B_n \gg 1$, gravitational forces dominate, and the liquid body takes on an elliptical shape. In the case of the water droplet of radius 2.5 mm as in our experiments, a simple calculation gives the pressure difference of 57.6 Pa for the droplet at room temperature.

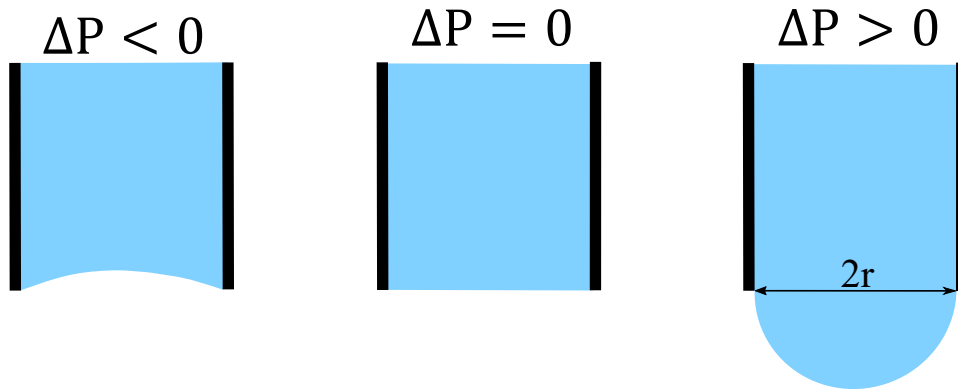


Figure 2.3: Three different configuration of water drop in the nozzle according to the pressure difference

A simple way to visualize the relation between the pressure difference ΔP , and the curvature is to use water in the nozzle. As shown in figure 2.3, we can expect three different configurations. If $\Delta P < 0$, the water is sucked inside the nozzle. If $\Delta P = 0$, the water flattens on the nozzle. Whereas $\Delta P > 1$ means, the water is pushed out of the nozzle. Due to surface tension, a drop forms in the nozzle, and unless the gravitational force exceeds the surface tension force, the water drop hangs on the nozzle. When the drop falls, the gravitational force mg , is not compensated by the surface tension force $2\pi r\gamma$, where r is the radius of the nozzle. This provides a simple way to estimate the mass or volume of a falling drop from a nozzle or to determine the surface tension by measuring the mass of the drop:

$$mg = 2\pi r\gamma. \quad (2.4)$$

Using this equation to estimate the volume of a drop falling from a nozzle with a radius of 1 mm, we obtain a drop volume of 46 μL , which closely aligns with the value observed in our experiments.

2.1.3 Wetting

Wetting is a well-observed but hardly understood phenomenon. We have all experienced rain completely wetting trees, windows, or clothes. However, sometimes we also observe that some leaves, such as those of the lotus plant, do not get wet. In some cases, we may desire a surface to be completely wet, as in the spreading of ink on paper during printing, coatings and paints, or the distribution of herbicides or insecticides in plants. In other cases, we do not want a liquid to wet the surface, such as in liquid-repellent coatings for outdoor jackets, car wind shields, roads, etc. Here, we will discuss the fundamental understanding necessary to describe wetting.

2.1.4 Young's Equation

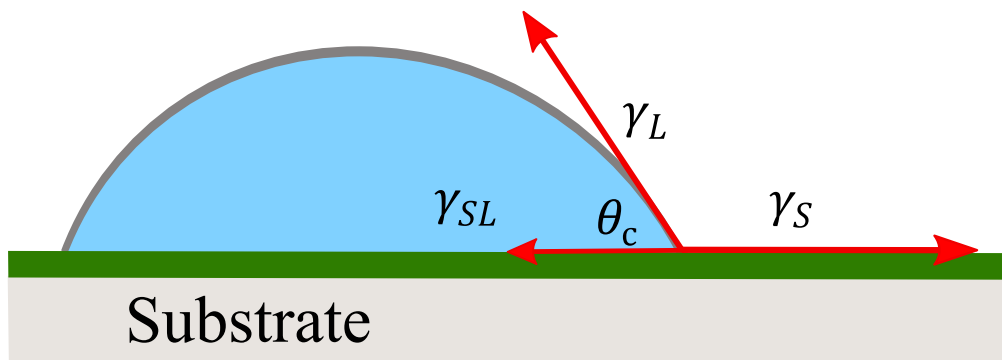


Figure 2.4: Ideal equilibrium contact angle of a sessile drop on a planar surface

A quantitative way to describe the wetting of the solid surface is by using Young's equation. Young's equation describes the equilibrium state, which is the most favourable state, and the change in Gibbs free energy is zero $dG = 0$. Gibbs free energy represents the thermodynamic potential used to calculate the maximum amount of work done by a closed system at constant pressure and temperature. It is defined by the equation

$G = U + pV - TS$, where U represents the internal energy p is the pressure V is the volume T is the temperature, and S is the entropy of the system [77]. The change in Gibbs free energy dG , indicates the spontaneity of a physical or chemical process in the system. If $dG < 0$, the process is spontaneous, i.e., the system releases energy to reach an equilibrium state, where $dG = 0$. Conversely, if $dG > 0$, the process is non-spontaneous, i.e., it requires energy input to change the system.

At equilibrium, the sum of the forces per unit length parallel to the surface is zero (see, Fig 2.4), and a liquid body atop a solid surface forms a contact angle θ_c . Young's equation relates the contact angle formed by the liquid on the surface to the interfacial tensions [78]:

$$\begin{aligned}\gamma_S - \gamma_{SL} - \gamma_L \cos \theta &= 0 \\ \cos \theta &= \frac{\gamma_S - \gamma_{SL}}{\gamma_L}.\end{aligned}\quad (2.5)$$

Here γ_L is the liquid surface tension γ_S is the solid surface tension, and γ_{SL} is the solid-liquid interfacial tension. If $\theta_c = 0$, the liquid completely wets the surface, and if $\theta_c \neq 0$, the liquid partially wets the surface.

In an ideal case, if the surface tension of the solid surface is higher than the solid-liquid surface tension ($\gamma_S > \gamma_{SL}$) $\cos(\theta_c)$ is positive, and $\theta_c < 90^\circ$. In this situation, the liquid body partially wets the surface. If the interfacial surface tension is higher than the solid surface tension ($\gamma_S < \gamma_{SL}$), then the contact angle becomes higher than 90° , and the contact line contracts, as shown in figure 2.5 (a) and (b), respectively. Generally, a surface with contact angle less than 90° is referred to as hydrophilic surface, and a surface with contact angle larger than 90° is called hydrophobic. For example, a typical contact angle on a hydrophobic surface, such as cross-linked polydimethylsiloxane (PDMS), is around 110° [79].

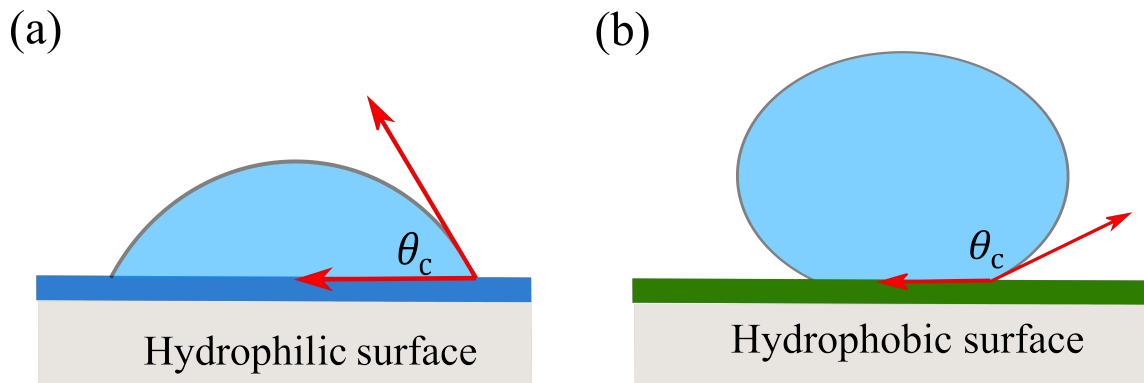


Figure 2.5: (a) Contact angle of hydrophilic surface $\theta_c < 90^\circ$ (b) Contact angle of hydrophobic surface $\theta_c > 90^\circ$

Young's equation is only valid for thermodynamic equilibrium in the presence of saturated vapour of liquid in the system, and might not be applicable in many practical cases. Similarly, the equation assumes an ideal case with a single contact angle. However, in reality, the exact contact angle cannot be measured accurately and might vary slightly within measurements. Therefore, in practice, the concept of an absolute contact angle, as stated in Young's equation, does not hold much significance. Instead, one typically calculates an average of multiple measurements, which may vary by a few degrees.

One method to measure a contact angle is to use a Goniometer. The Goniometer typically consists of a pump to shape a drop of liquid onto the solid surface and a video camera to capture the drop and the surface. Then, the volume of liquid is increased using a pump, and at the moment when the advancing contact line starts moving, the advancing contact angle (θ_a) is measured. Similarly, to measure the receding contact angle (θ_r), the volume of liquid is decreased, and the contact line is observed. As the contact line starts to recede, the contact angle is measured. To obtain the contact angles, the contour is fitted using the Laplace equation. The difference between the advancing and receding contact angles is known as contact angle hysteresis ($\Delta\theta = \theta_a - \theta_r$). Possible reasons for this contact angle hysteresis include surface heterogeneities, surface chemistry, surface roughness, and soft surfaces, among others [80, 81, 82].

Young's contact angle considers the macroscopic contact angle, which is on the length scale of a few $\mu\text{m} - \text{mm}$. However, the contact angle at much smaller scales (nanometers), where van der Waals forces and the electric double layer are important, might be completely different and could influence the results in some particular cases. Nevertheless, the macroscopic picture of Young's model in combination with contact angle hysteresis can describe most observations.

2.1.5 Dynamic wetting

Any external perturbations at the solid-liquid interface can induce a dynamic wetting state. A typical example of such a dynamic wetting state is the motion of a sessile drop due to gravitational potential. Figure 2.6 shows the effect of gravity as we tilt the system with the tilt angle β . This provides the drop with an external gravitational force of $mg \sin \beta$, where m is the drop mass and g is the gravitational acceleration, which is 9.8 m/s^2 . Here, the drop velocity is proportional to the tilt angle, and we use this principle to force the drops to slide down the surface in our slide electrification

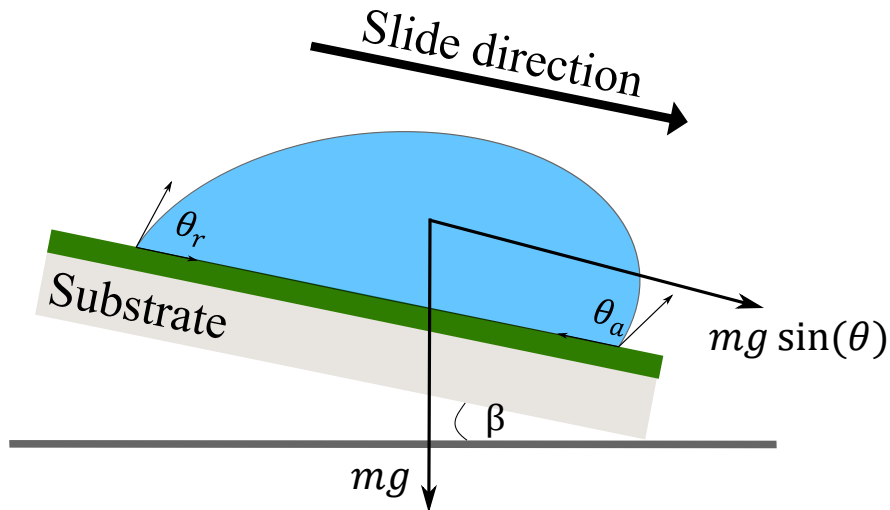


Figure 2.6: Dynamic contact angle hysteresis of sliding drop with advancing contact angle θ_a is different from receding contact angle θ_r .

experiments.

As the drop slides, it forms the advancing contact angle in the wetting direction and a receding contact angle on the dewetting side. One must distinguish between these contact angles in the static and dynamic cases. In the dynamic case, the advancing contact angle increases with the increasing velocity, and the receding contact angle reduces with the increasing drop velocity. One can use the sliding velocity to calculate the kinetic drop friction on different solid surfaces [59].

2.2 Interface & Electric double layer (EDL)

A liquid bulk consists of molecules surrounded by other molecules, and they interact with each other via van der Waals interactions or chemical bonds. Since the interactions are equal in all directions, the bulk has no net electric charge or free energy [83].

When a liquid comes into contact with another phase of materials (solid, air, or another liquid), the symmetry is broken, and the interactions at the interface can change. An example of such a process is the contact between liquid water and a solid surface. In water or high dielectric liquids, most solid surfaces obtain a net charge. This surface charge can form spontaneously through processes such as the adsorption of ions from the solution, protonation, or deprotonation of surface groups, or the

preferential dissolution of ions. This leads to the formation of surface charge and the EDL [62, 63].

Basic groups like amine groups can get protonated in contact with water and attain positive charge. In acidic groups like carboxylic or sulfonic acid can deprotonate in contact with water and attain negative charge. Nevertheless, this is not the prerequisite for the formation of surface charge. Inert surfaces like hydrophobized glass surfaces can also get charged due to the preferential absorption of hydroxide ions [32].

The surface charge at the interface gives rise to the surface potential Φ , which is the electrostatic potential difference between the solid-liquid interface and the liquid bulk [84, 67, 63]. This surface potential is one of the fundamental properties in colloid and interface science. It determines the stability of dispersions and emulsions, causes electrokinetic phenomena, corrosion, influences catalytic activity, contact angles, and the thickness of thin liquid films [85]. Moreover, the surface potential is a fundamental property of biological membranes. Several models have been developed to describe the formation of such a charge at the interface, but each one comes with its own assumptions and limitations, which we will discuss in this chapter.

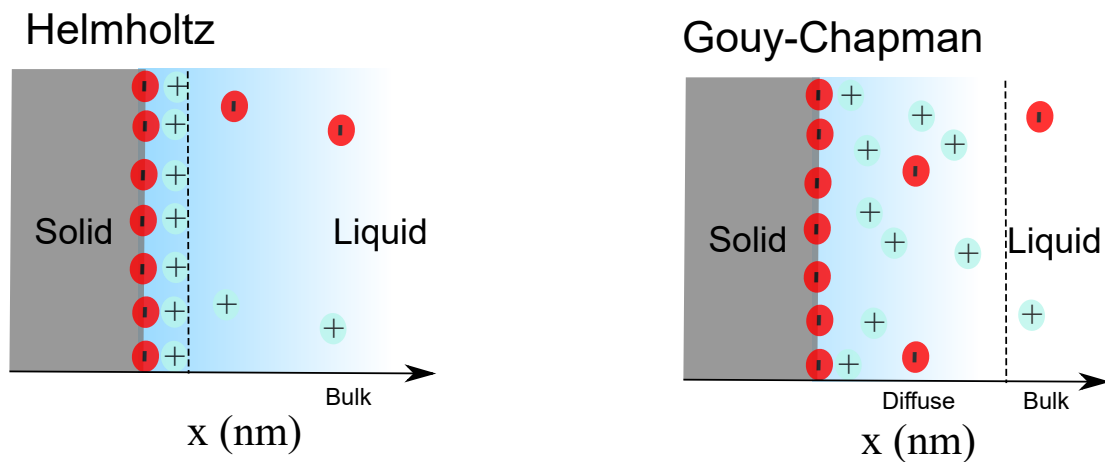


Figure 2.7: Electric double layer (EDL) as described by Helmholtz and Gouy-Chapman model

2.2.1 Helmholtz model

The simplest way to describe the influence of surface charge at the solid-liquid interface is through the Helmholtz picture, named after the German physicist Ludwig Helmholtz¹. This model assumes that the surface potential resulting from surface

¹Hermann Ludwig Ferdinand von Helmholtz, 1821 – 1894

charge attracts counter ions from the liquid, forming a double layer. In this model, the double layer consists of a charge layer and a single layer of counter ions. Beyond this layer, the liquid behaves as if there is no surface potential ($\Phi = 0$) [86].

In Figure 2.7 (left), you can see a visual representation of this simple structure, which resemble a basic parallel plate capacitor with capacitance (C_{Hz}). This model was an early attempt to describe the charged surface and demonstrated that the interface behaves like a capacitor with molecular dielectrics. However, it did not take into account the thermal diffusion of ions and ion-ion interactions. Moreover, the experimentally measured double layer capacitance (C_{DL}) often deviated from the predictions.

2.2.2 Gouy-Chapman model

In the early 1900s, Gouy¹ and Chapman² expanded upon the Helmholtz model of the double layer by incorporating the thermal energy of ions [87, 88]. The introduction of this perspective, as depicted in Figure 2.7 (right), revealed that the double layer must include a diffuse layer. This is because the potential generated by the surface charge attracts counter ions, but the thermal energy tends to push these ions away from the surface. As a result, the potential does not drop to zero immediately, but gradually decays towards the bulk.

The Gouy-Chapman model simplifies the description of the solid-liquid interface by ignoring the molecular nature of the liquid and the discrete nature of ions. It also does not account for the finite size of ions and the non-coulombic interactions between them. This model assumes a continuous potential field, which is an oversimplification of reality. However, despite these simplifications, the Gouy-Chapman model is surprisingly effective at describing the diffuse layer. One reason for this success is that some of the model's assumptions and errors partially offset each other. For example, while the neglect of finite ion size tends to increase the surface potential, ignoring non-coulombic interactions tend to decrease the surface potential [63].

2.2.2.1 Poisson–Boltzmann statistics of diffuse layer

In this section, we will derive an equation to describe the potential landscape of the diffuse layer for an infinitely long planar surface, where the potential remains constant

¹Louis Georges Gouy, 1854 – 1926, French physicist

²David Leonard Chapman, 1869 – 1958, an English physical chemist

in the y - and z -directions. One way to relate the charge density to the potential is by using the Poisson equation:

$$\nabla^2\Phi = -\frac{\sigma_{EDL}}{\epsilon_o\epsilon_r}. \quad (2.6)$$

Here σ_{EDL} is the local solid-liquid surface charge density ϵ_o is the vacuum permeability, and ϵ_r is the permeability of the medium.

Once we have information about the charge distribution, we can calculate the potential at a specific position. However, the presence of ions in the liquid determines the charge distribution. The local ion distribution is described by Boltzmann statistics:

$$c_i = c_o \cdot e^{\frac{-e\Phi(x)}{k_B T}}. \quad (2.7)$$

Now, we consider both cation and anion that are present in the liquid and modify eq.(2.7) and get

$$\sigma_{EDL} = e \cdot (c^+ - c^-) = e \cdot c_o \cdot \left(e^{\frac{-e\Phi(x)}{k_B T}} - e^{\frac{e\Phi(x)}{k_B T}} \right). \quad (2.8)$$

Here $-e\Phi$ represents the position-dependent electric work required to bring an ion closer to the surface, where e is the charge of the ion k_B is the Boltzmann constant, and T is the temperature.

Combining eq.(2.6) and eq.(2.8), we get the Poisson–Boltzmann eq.

$$\nabla^2\Phi = -\frac{e \cdot c_o}{\epsilon_o\epsilon_r} \left(e^{\frac{-e\Phi(x)}{k_B T}} - e^{\frac{e\Phi(x)}{k_B T}} \right). \quad (2.9)$$

We can solve this partial differential equation for the simple planar case by making some basic assumptions and applying the necessary boundary conditions. Furthermore, we linearize Eq. (2.9) for potentials where $\Phi \ll k_B T$ ($k_B T$ being approximately 25 mV at room temperature). This results in the linearized Poisson–Boltzmann equation:

$$\frac{d^2}{dx^2}\Phi \approx \frac{2c_o e^2}{\epsilon_o\epsilon_r k_B T} \Phi. \quad (2.10)$$

The general solution to this one-dimensional differential equation is as follows:

$$\Phi = C_1 e^{-\frac{x}{\lambda_D}} + C_2 e^{\frac{x}{\lambda_D}}, \quad (2.11)$$

where

$$\lambda_D = \sqrt{\frac{\epsilon_o\epsilon_r k_B T}{2c_o e^2}} \quad (2.12)$$

and C_1 and C_2 are constants. The decay length λ_D is also known as the Debye length. This Debye length depends on concentration (c_o) and decreases with increasing salt

concentration (see Fig. 2.8). A typical Debye length for a 1 mM aqueous NaCl solution is 9.7 nm. The Debye length increases by hundreds of nanometers in distilled water due to its very low ion concentration.

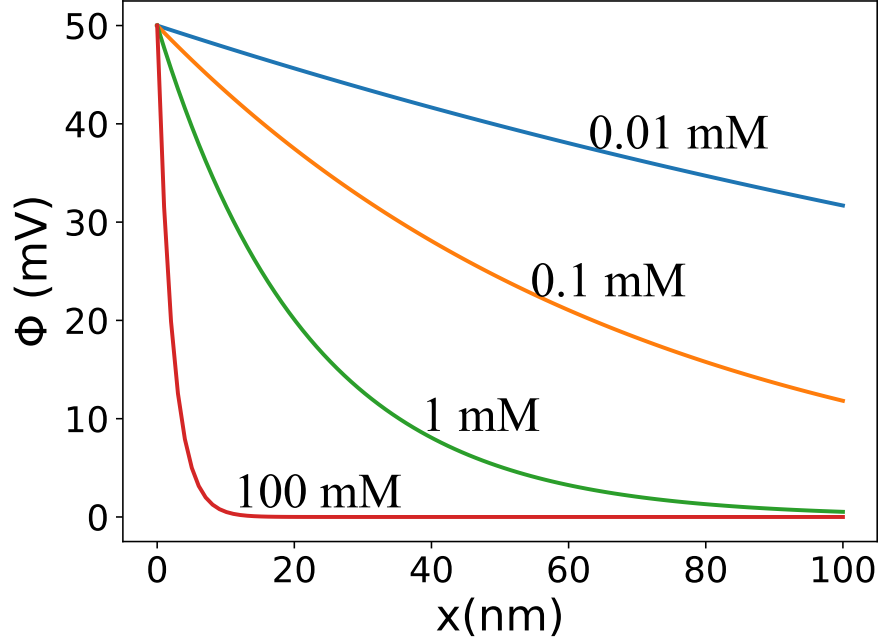


Figure 2.8: Potential landscape for different salt concentrations assuming the surface potential of 50 mV

We can further simplify eq. (2.10) by using boundary conditions. These boundary conditions provide the surface potential at two different extremes. At $x = 0$, the surface potential Φ should equal the total surface potential Φ_0 , and as x approaches infinity ($x \rightarrow \infty$), the surface potential should approach zero. Therefore, the solution to the linearized Poisson–Boltzmann equation becomes:

$$\Phi = \Phi_0 e^{-\frac{x}{\lambda_D}}, \quad (2.13)$$

The solution of the linearized Poisson–Boltzmann equation for low potentials is simple yet very powerful, and it can even be applied to higher potentials, up to 80 mV [63]. This solution provides a clear depiction of the diffuse layer and demonstrates how it decreases exponentially with the decay length λ_D from the surface, as shown in figure 2.8.

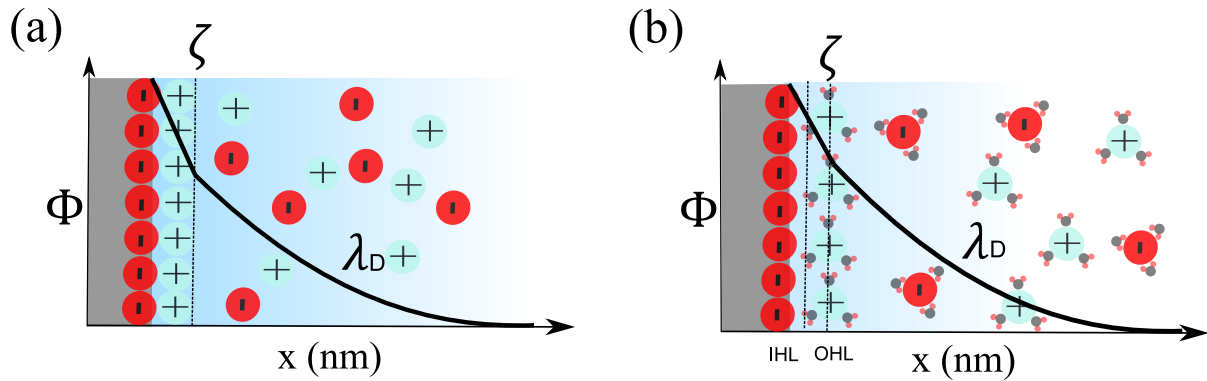


Figure 2.9: (a) Potential landscape in Stern model (b) potential landscape in Grahame model with Inner Helmholtz Layer (IHL) and Outer Helmholtz Layer(OHL)

2.2.3 Stern model

Stern¹ essentially combined Helmholtz and Gouy-Chapman concepts to describe the Electric Double Layer (EDL) [89]. In the first layer, there are immobile counter ions attached to the charged surface, which can be described as a plate capacitor with capacitance C_{St} . Here, the potential drops rapidly due to the absorbed counter ions. This potential after the first immobile layer is also known as the ζ -potential (see Fig. 2.2). Additionally, on top of the immobile ions, there is a diffuse layer, as described by Gouy-Chapman, where the potential falls within the Debye length.

The Stern layer picture becomes more complex when considering the hydration of cations and anions. Due to the hydration shell, the immobile ions are not directly in contact with the surface but can have a layer of polarized H_2O molecules between the ions and the surface charge. This can be described using the concept of inner and outer Helmholtz layers, as shown in Figure 2.2b. We will not further discuss the more complicated models because it is still an ongoing field of research, and in most cases, the Stern model captures most of the measurable physical effects.

2.2.4 The Grahame's Equation

Grahame² introduced an equation to estimate the surface potential Φ , from the surface charge density σ_{EDL} , using the Gouy-Chapman model and the electroneutrality of the

¹Otto Stern, 1888 – 1969, German-American physicist and Nobel laureate in physics

²David C. Grahame, 1912-1958, American physical chemist

EDL [90]. This yields the surface charge density

$$\sigma_{EDL} = \sqrt{8c_0\epsilon_0\epsilon_r k_B T} \sinh\left(\frac{e\Phi_0}{2k_B T}\right) = \frac{2\epsilon_r\epsilon_0 k_B T}{e\lambda_D} \sinh\left(\frac{e\Phi_0}{2k_B T}\right). \quad (2.14)$$

Solving this equation for a low potential system and expanding \sinh and taking only the first term, one obtains a straightforward equation to estimate the surface charge density.

$$\sigma_{EDL} = \frac{\epsilon_0\epsilon_r\Phi_0}{\lambda_D}. \quad (2.15)$$

These discussions of various models have provided us with a comprehensive understanding of the EDL. It is evident that a model does not need to be overly complex to grasp the underlying physics of the system. The best model is one that offers the clearest insight with the simplest assumptions.

2.3 Slide electrification

Numerous studies have demonstrated that liquid drops sliding atop hydrophobic surfaces become charged, leaving an opposite charge on the surface. One possible mechanism at the origin of charge separation in sliding drops might be the combination of the EDL and moving three-phase contact line.

To describe slide electrification, Stetten et al. [14] assumed that the surface charges from the EDL are left by the receding contact line as the drop slides. The amount of charge left by the receding contact line depends on the charge density within the tail of the sliding drop σ_L , and the charge density σ_s , left on the substrate. Experiments showed that the charge transfer decreases as the drop slides down the surface; therefore α should decrease with the increasing drop potential. The Taylor expansion of this transfer coefficient with respect to charge gives:

$$\alpha(Q) = \alpha_0 + \frac{qQ}{C_D k_B T} \alpha_1. \quad (2.16)$$

Here Q represents the drop charge α_0 stands for the transfer coefficient at $Q = 0$, and α_1 denotes the first term of the Taylor expansion. C_D represents the drop capacitance k_B is the Boltzmann constant, and T is the temperature. In this model, the charge transfer process is linearized by considering only the first term of the Taylor expansion. The energy required for charge separation is scaled using thermal energy $k_B T$, which introduces the factor $\frac{qQ}{C_D k_B T}$ in front of the term α_1 . As a drop slides over the substrate

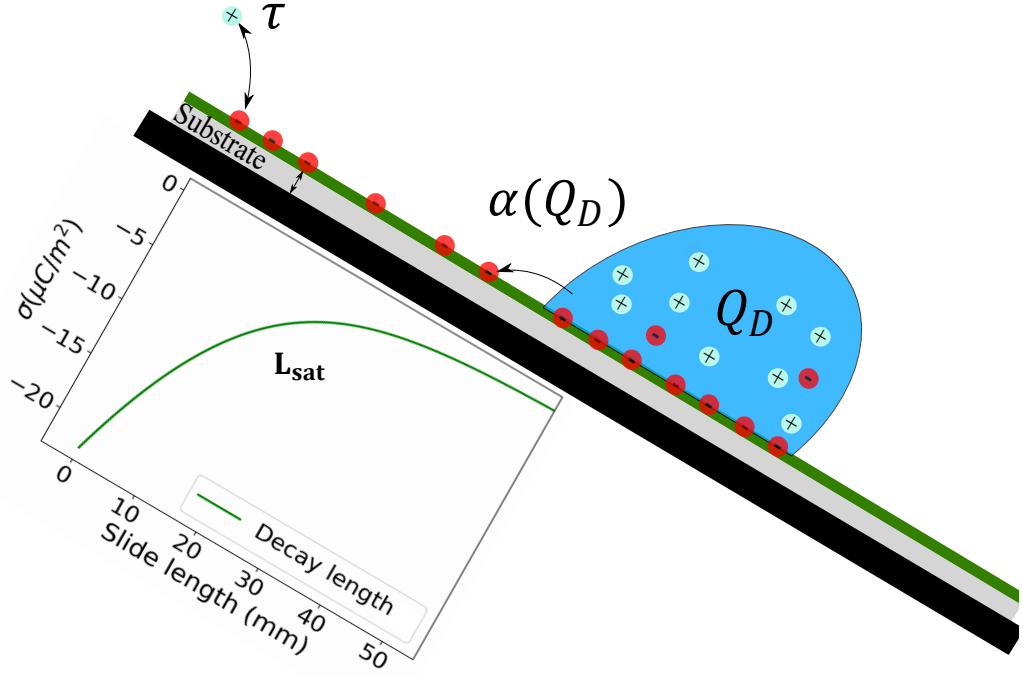


Figure 2.10: The charge separation process representation, where L_{sat} represents the decay length $\alpha(Q_D)$ denotes the drop charge-dependent transfer coefficient, and τ signifies the surface discharge time.

by dx , the accumulated charge is given by:

$$dQ_1(x) = -\alpha(Q)\sigma_L w dx \quad (2.17)$$

$$\Rightarrow dQ_1 = -\left(\alpha_0 + \alpha_1 \frac{qQ_1}{C_D K_B T}\right) w \sigma_L dx \quad (2.18)$$

$$\frac{dQ_1}{dx} + \frac{Q_1}{L_{\text{sat}}} = -\alpha_0 w \sigma_L. \quad (2.19)$$

Here $L_{\text{sat}} = \frac{C_D k_B T}{\alpha_1 q w \sigma_L}$, which represents the length at which the change in charge dQ , becomes zero. Here $\alpha(Q)$ is the charge transfer coefficient w is the width of the drop, and x gives a coordinate along the sliding path. By solving the differential eq. (2.19), one can determine the total charge of the first drop.

For a single drop sliding over the surface, then the surface charge density as a function of x is given by

$$\sigma_{S1}(x) = -\frac{1}{w} \frac{dQ_1}{dx} = \sigma_L \alpha_0 \cdot e^{\frac{-x}{L_{\text{sat}}}}. \quad (2.20)$$

As multiple drops slide down the surface, one can observe dynamics in drop charge over the course of successive drops. This phenomenon arises from the charging and

discharging of the surface. A simple model to describe this discharging process is an exponential decay, which can be expressed as follows:

$$\sigma_s(t) = \sigma_s(0) \cdot e^{-\frac{\Delta t}{\tau}}, \quad (2.21)$$

where $\sigma_s(0)$ is the initial surface charge $\sigma_s(t)$ is the surface charge after time Δt , and τ is the surface discharge time. If the time between drops is Δt , then the differential equations describing the drop charge and the surface charge density after n^{th} drop are as follows

$$\frac{dQ_n}{dx} + \frac{Q_n}{L_{\text{sat}}} = w\sigma_{s_{n-1}}e^{-\Delta t/\tau} - w\sigma_0. \quad (2.22)$$

$$\sigma_{s_n}(x) = \sigma_{s_{n-1}}e^{-\Delta t/\tau} - \frac{1}{w} \frac{dQ}{dx}. \quad (2.23)$$

The analytical solutions of these equations at steady state are given as

$$Q_\infty(L) = -w\sigma_0 L_{\text{sat}} \left[1 - \exp \left[-\frac{L}{L_{\text{sat}}} \left(1 - e^{-\Delta t/\tau} \right) \right] \right] \quad (2.24)$$

$$\sigma_{s_\infty}(x) = \sigma_0 L_{\text{sat}} \left[-\frac{x}{L_{\text{sat}}} \left(1 - e^{-\Delta t/\tau} \right) \right]. \quad (2.25)$$

Here L is a slide distance, and x is a coordinate on the slide path.

This model describes the drop and surface charge in sliding drops by using equations (2.24), and (2.25). The model assumes the solid-liquid interfacial charge density σ_L , and a phenomenological drop charge-dependent transfer coefficient $\alpha(Q_n) = \alpha_0 + \alpha_1 Q_n$ to describe the slide electrification. The resulting model provided a qualitative description of the drop charge dependence on drop number and sliding length. Nevertheless, the model does not fully capture the physical mechanism connecting charging drops to the EDL, and many assumptions, such as surface discharge and charge separation at the receding contact line, remain unverified.

Chapter 3

Methodology

3.1 Electrical concepts

Before delving into the discussion on measurement methods, let us establish a foundation by exploring some fundamental electrical concepts. The concepts discussed here are drawn from "Introduction to Electrodynamics" by D. J. Griffiths [91].

3.1.1 Electrostatics

The basis of electrostatics comes from inherent properties of fundamental atomic particles such as electrons and protons. These particles carry a net charge known as the elementary charge (1.6×10^{-19} C [92]), also referred to as unit charge. Electrons are associated with a negative charge, while protons carry a positive charge. Additionally, ions serve as other sources of charge; atoms or molecules with an excess of electrons are called anions, and those with a deficiency are called cations. A question might arise how these particles interact with each other if we bring them together.

Let us consider a charge q in free space, and we want to bring a probe charge q_1 close to it. The electrostatic force \mathbf{F} , between two charged particles, situated at a distance $\mathbf{r} = \mathbf{x} - \mathbf{x}'$ is determined by Coulomb interaction and is quantified using Coulomb's law:

$$\mathbf{F} = \frac{qq_1}{4\pi\epsilon_0 r^2} \hat{r}, \quad (3.1)$$

where $\epsilon_0 = 8.854 \times 10^{-12}$ C²/Nm² is the permittivity of vacuum \hat{r} is the direction from q to q_1 r is the magnitude, and x' and x are the respective positions of q and q_1

in the reference frame. The electrostatic force is proportional to the product of the charges and decreases with the square of the distance. This force is repulsive when two particles carry the same charge (e.g., two cations or anions) and attractive when the charges are opposite (e.g., cations and anions).

We can extend the two-particle system to a continuous charge distribution over a surface of a certain area with the charge density σ , by integrating the total interactions:

$$\mathbf{F} = \frac{q_1}{4\pi\epsilon_0} \int \frac{\sigma}{r^2} \hat{r} dA, \quad (3.2)$$

where

$$\mathbf{E} = \frac{1}{4\pi\epsilon_0} \int \frac{\sigma}{r^2} \hat{r} dA. \quad (3.3)$$

\mathbf{E} is defined as the electric field, E-field, and the electrostatic force can be written as $\mathbf{F} = q_1\mathbf{E}$. Here, dA is a small element area on the surface. We can observe from eq.(3.3) that the E-field is independent of the probe charge q_1 and only depends on σ and the distance.

We can use Gauss' law to find the relationship between the electric field and the charge density. Gauss' law states that the E-field per unit area (electric flux) outside an enclosed surface is proportional to the net charge inside the surface divided by the permittivity, or the divergence of the electric field is given by

$$\nabla \cdot \mathbf{E} = \frac{\sigma}{\epsilon_0}. \quad (3.4)$$

While the divergence of the electric field gives the charge density, the curl of the static electric field is zero $\nabla \times \mathbf{E} = 0$, meaning the line integral of the E-field is path-independent and only depends on the endpoints. This $\nabla \times \mathbf{E} = 0$ also implies the vector field is a gradient of a scalar quantity and can be written as

$$\mathbf{E} = -\nabla V, \quad (3.5)$$

where V is an electric potential, and the negative sign is used as a convention to show the direction of the electric field from positive to negative. We can further use eq. (3.6) to find the relationship between V and σ , which is also known as Poisson's equation

$$\nabla^2 V = -\frac{\sigma}{\epsilon_0}. \quad (3.6)$$

Similar to the flow of water due to pressure difference, the potential difference ΔV , causes the flow of electric current I , between two points. Metals are very good

conductors due to the presence of free electrons in their valence bands. In contrast, insulators, like glass, have high resistivity (low conductivity), obstructing current flow, as they lack mobile electrons. The relationship between the electric current I , the potential difference ΔV , and the resistance R , is given by Ohm's Law, which states that the flow of current is directly proportional to the potential difference, and the proportionality constant is the resistance. Mathematically, this relationship is represented as $\Delta V = IR$.

Another way to comprehend electrical current is to use the analogy of water flowing from a higher to a lower altitude, forming a river. This flow of water, known as river current. In the electrical context, electric current represents the rate of flow of electric charge, expressed as $I = dQ/dt$, measured in amperes A . We can calculate the total amount of charge Q , by integrating the current over time as follows:

$$Q(t) = \int_0^t I(t') dt' \quad (3.7)$$

A capacitor is an electrical device designed to store electric charge. A simplified representation of a capacitor involves parallel plates with a uniform electric field. Such capacitors comprise two conductors separated by a specific distance d . The electric charge stored within a capacitor can be estimated by the product of the potential difference and the capacitance ($Q = C\Delta V$). The capacitance depends upon the physical factors of the system such as the distance between conductors d , the area of the conductors A , and the relative permittivity of the medium (ϵ_r)

$$C = \epsilon_r \epsilon_0 \frac{A}{d}. \quad (3.8)$$

If the E-field lines between these conductors are uniform, then the work needed to move a unit charge q , is $W = \Delta V q$. Comparing this equation with $W = F \cdot d = q \cdot E \cdot d$, we get the potential difference in a capacitor can be expressed as $\Delta V = E \cdot d$.

The flow of current during the charging or discharging of the capacitor is known as capacitive current I_c , given by $I_c = d(CV)/dt$. The time required to charge or discharge the capacitor is given by the product of resistance and capacitance, denoted as $\tau = RC$.

3.1.2 Sensing electrical current

A straightforward approach for measuring electrical current involves using a shunt resistor, which operates based on Ohm's law. This device comprises a shunt resistor

in series, and one measures the voltage drop across the resistor. However, this method can affect the accuracy of the measured current because of the active electrical element in the circuit. It is also noise-sensitive, and the measuring bandwidth could not be controlled, making it unsuitable for accurately measuring low current signals.

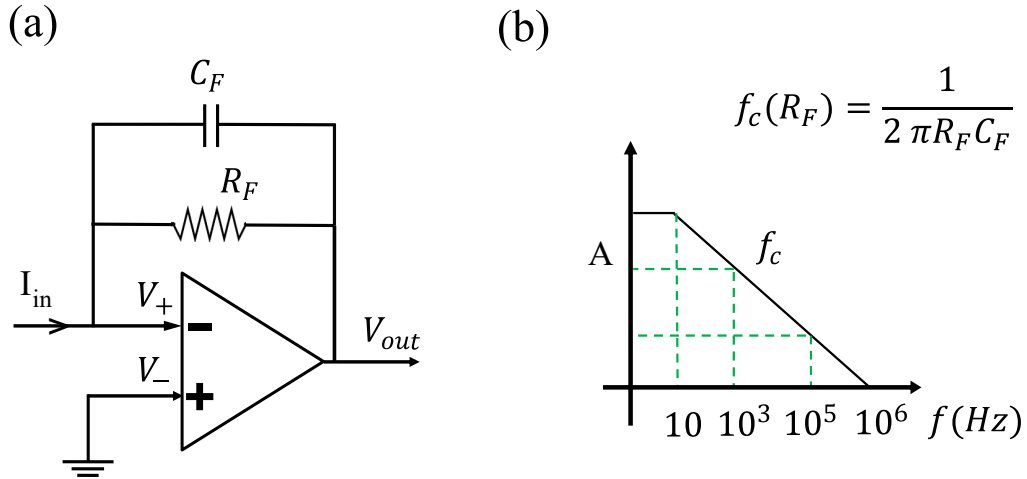


Figure 3.1: (a) shows the illustration of transimpedance amplifier, (b) shows the frequency dependent amplitude response after using compensating capacitor C_F .

An alternative way to measure a low electrical signal is to use a transimpedance amplifier (TIA), which utilizes operational amplifiers (Op-amps). TIA serves as a current-to-voltage converter, where the output voltage is determined by the input current and the gain factor provided by the feedback resistor R_F . The fundamental principle of TIA is that no current flows through the input terminals. As the negative terminal senses an input current I_{in} , the Op-amp adjusts the output voltage V_{out} , so that an equivalent amount of current flows through R_F . TIA is more suitable for measuring low currents since it allows for increasing the measurement voltage by adjusting the gain, without affecting the current source.

Two crucial factors that one needs to consider when using such a measurement device are the bandwidth and the signal-to-noise ratio. Ideally, one aims to achieve maximum signal across the entire frequency spectrum. However, due to the presence of input and internal capacitance, the TIA introduces a low-pass filter in the feedback path. This means the TIA does not measure the complete signal beyond a certain frequency. To overcome this, one can introduce a compensating capacitor C_F , as shown in Fig. 3.1a. By controlling this external capacitor, one can control the low-pass filter and achieve the defined response in different frequency regimes, as shown in Figure 3.1b.

The second factor that one needs to consider is the signal-to-noise ratio. Two typical sources of such high background noise are thermal noise and electrostatic noise from a high-voltage source, or 50 Hz noise from the grid. One can improve the signal-to-noise ratio by using high feedback resistance or low bandwidth, and by placing the whole setup in a Faraday cage.

3.2 Experimental setups

We use three different approaches to study slide electrification. The first is the discharge current measurement method, where we investigate the accumulated drop charge by integrating the discharge current. The second method (*Super probe*) involves studying the drop potential by using an external input capacitor. The third method we employ is the mirror charge detection method (*Subsurface probe*), where we measure the capacitive current to locally determine the surface charge density. We used a National Instruments data acquisition board (NI USB-6366 x-Series) to record the current or voltage signal. In the following, we describe both methods in detail.

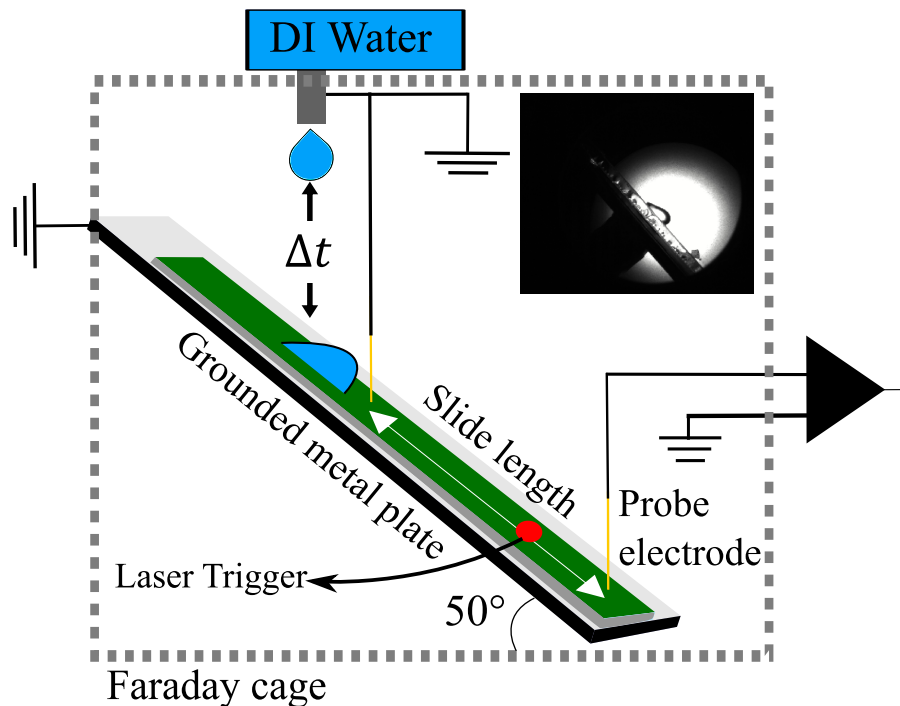


Figure 3.2: Illustration of experimental setup

3.2.1 Discharge current measurement

Figure 3.2a illustrates a schematic of the entire experiment, which comprises water, a grounded syringe that releases a neutral drop of volume $45 \mu\text{L}$, a tilted metal sample holder, a ground electrode, probe electrodes, a laser trigger system, and a sub-femtoampere transimpedance current amplifier (rise time: $0.7\text{--}1.8 \mu\text{s}$, FEMTO DLPCA-200, Berlin, Germany). Everything, except the amplifier (due to its electric connection), is placed inside a Faraday cage to minimize external electrostatic effects.

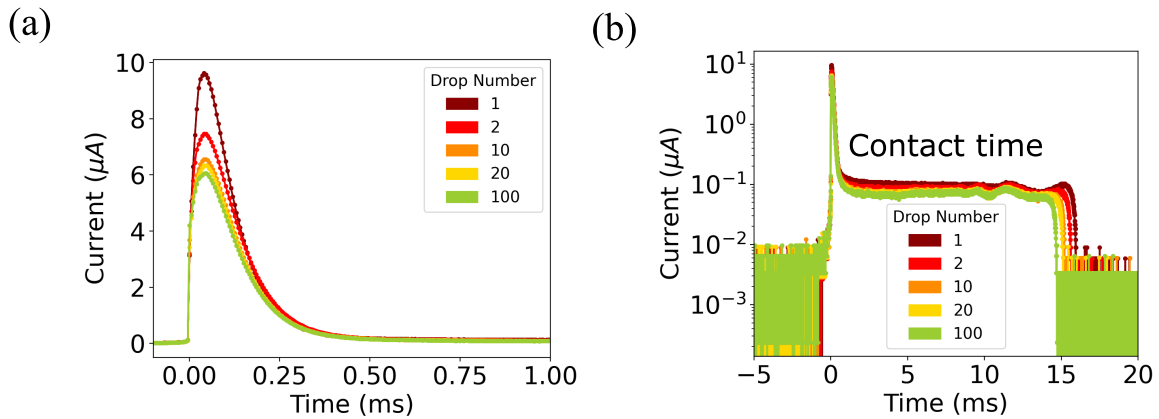


Figure 3.3: (a) Short-circuit current measured as the probe electrode discharges the sliding drop, and (b) drop-surface is the contact time.

A grounding metal electrode is placed at the beginning of the slide length. As drops fall on the substrate, they acquire bouncing charge. To neutralize this initial charge, the grounding electrode is placed around 1.0 cm away from the bouncing point.

A laser trigger system is used to initiate the data acquisition. This system consists of two essential components: a laser pulse and a photodiode. As long as the laser pulse hits the photodiode, there is a positive output voltage. But as soon as the laser pulse is stopped, there is a sudden voltage drop. The edge of this voltage drop is used to start the data acquisition.

The probe electrode is a thin metal (Tungsten or gold) wire which discharges the sliding drops. As the positively charged drop gets in contact with the electrode, we measure a current using TIA. Figure 3.3, shows the discharge current after each drop. In the current signal, we see the initial discharge peak ($10 \mu\text{A}$) of around 0.5 ms Fig 3.3 a and a long tail current (80 nA) of around 15 ms Fig 3.3 b. The initial peak is associated with the discharge of accumulated drop charge after sliding the prede-

terminated slide path. Whereas, the long tail is the current due to the ongoing charge separation as the drop is in contact with the probe and the surface. To obtain the accumulated drop charge, we integrated the initial peak of 0.5 ms. We also estimated the average velocity of the sliding drop by using two time points (laser trigger and probe signal) during the measurement.

3.2.2 Drop voltage measurement

To measure the voltage of sliding drops, we incorporated a 1 nF capacitor in parallel with the NI box. The NI box has a high input resistance of 100 G Ω and an input capacitance of 100 pF. Including the cable, we determined a total system capacitance of 1.35 nF using a capacitance meter. An additional 400 M Ω resistor ensures capacitors discharge between drops while maintaining voltage stability during drop contact. The schematic of the voltage probe is presented in figure 3.4a.

The voltage in the capacitor C_D before contact with the probe C_{in} capacitor is denoted as U_D . The charge in C_D is represented as Q . After contact, the total charge equilibrates between the two parallel capacitors, both achieving the same voltage. The total charge in this situation is given by

$$Q = C_{\text{total}}U_{in} = (C_D + C_{in})U_{in} = C_D U_D. \quad (3.9)$$

We can rewrite this equation as:

$$U_D = \frac{C_{in} + C_D}{C_D} U_{in}. \quad (3.10)$$

From the measured voltage, we calculated the initial drop voltage using the ratio of two known capacitors in eq.(3.10). Figure 3.4c illustrates the measured voltage vs drop number.

In the voltage curves (Fig. 3.4b), we can observe the initial peak is followed by a linear increase in voltage. This linear increase in voltage due to the ongoing charge separation at the moving contact line. The current resulting from ongoing charge separation can be estimated as

$$I = (C_D + C_{in}) \frac{dV}{dt} \approx C_{in} \frac{dV}{dt}, C_{in} \gg C_D \quad (3.11)$$

, which yields a value of 70-80 nA. This value matches the tail current measured in previous method 3.2.1.

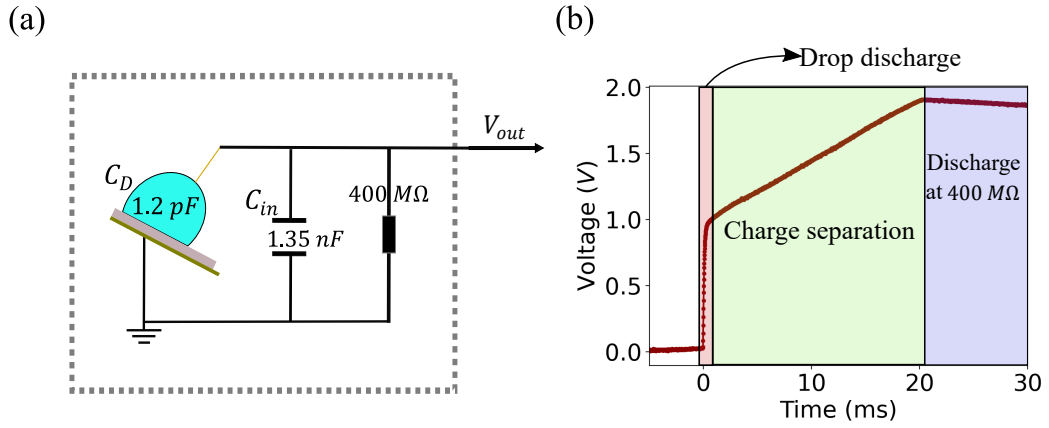


Figure 3.4: (a) Setup to measure the high drop voltage using capacitors in parallel. (b) Voltage measured as drop comes in contact with probe electrode.

3.2.3 Mirror charge method

To investigate the surface charge as a drop dewets the surface, we use a mirror charge detection method. The main idea behind the method is to use a metal electrode beneath the substrate to quantify the surface charge left behind by the sliding drop. Figure 3.5 illustrates the basic concept of the subsurface setup, where a drop moves on top of the substrate and acquires a positive charge. During this process, a negative charge is left on the surface. We utilize the principle of a parallel capacitor, where the probe electrode acts as the bottom plate, and the sliding drop on the substrate acts as the top plate. Given that the plate length is $L = 5$ mm, which is five times larger than the distance between the plates ($d = 1$ mm), we assume a locally homogeneous electric field distribution and a low stray field within the capacitor as a first-degree approximation. By measuring the capacitive current as the drop moves on top of the substrate and integrating this current using the equation $Q = \int_0^t I(t') dt'$, we estimate the surface charge.

To comprehend the current signal induced by the moving charged drop on the subsurface probe electrode, we examined the drop's position using a high-speed camera (Photron FastCam Mini UX100, frame rate 1000), as shown in figure 3.6. In the figure, we can observe the current polarity during two distinct cases. When a positively charged drop moves towards the area above the probe electrode, it increases the negative mirror charge on the electrode, resulting in a *positive current*. As the drop is directly on top of the electrode, the current reaches zero. Conversely, when the positively charged drop moves away from the electrode, the current polarity changes, and there is a *negative current*.

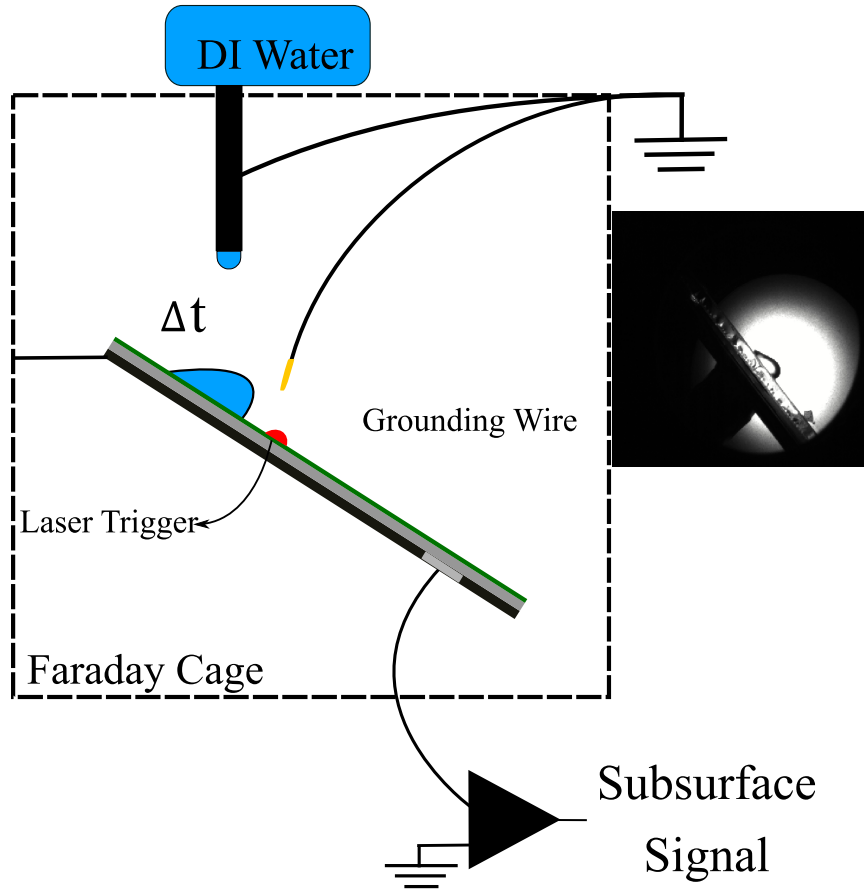


Figure 3.5: Illustration of subsurface (mirror charge) measurement setup

3.2.4 Numerical simulation of capacitive current

We use a sliding plate capacitor model to verify the working principle discussed earlier. The concept involves the bottom electrode acting as a static bottom plate, while the moving top plate mimics a drop to slide down its surface. The change in area due to the sliding drop results in variations in capacitance and induced charge over time, leading to a capacitive current. This phenomenon can be modelled using four simple equations as follows:

$$Q = \sigma A(t) \quad (3.12)$$

$$C = \epsilon_0 \epsilon_r \frac{A(t)}{\sqrt{d^2 + l^2}} \quad (3.13)$$

$$V = \frac{Q}{C} \quad (3.14)$$

$$I = C \frac{dV}{dt}. \quad (3.15)$$

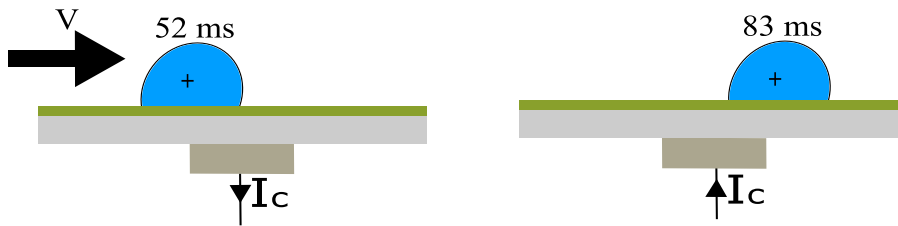
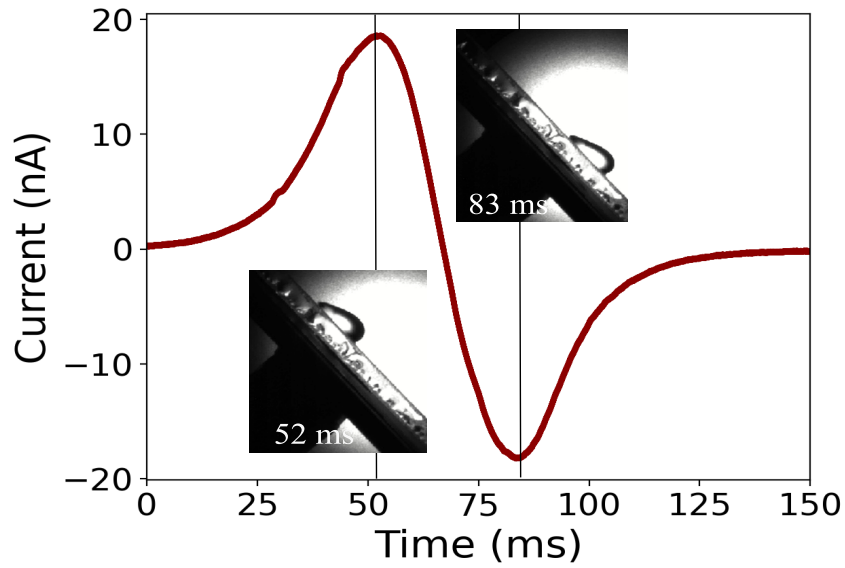


Figure 3.6: Capacitive current and its corresponding drop position identified using high speed video. The capacitive current increases as the drop moves toward the probe electrode, and it changes the polarity as the drop moves away from the probe electrode.

Here, σ is the charge density A is the area (which changes with sliding drop) d is the dielectric thickness l is the horizontal distance between two the drop and the bottom plate V is the voltage, and t is the time (which depends on the velocity v). This implies that by increasing the velocity and the area, one can enhance the capacitive current.

We compared the modelled induced current with the measurements, as illustrated in figure 3.7. For the simulation, we used a charge density of $\sigma = -20\mu C/m^2$ and a velocity of $0.2 m/s$, values close to those observed experimentally. The slight deviation between the model and the measurements could be attributed to the simplified geometrical assumptions, such as the use of a rectangular plate, and constant velocity. Nonetheless, there is a good agreement between the model and the measurement.

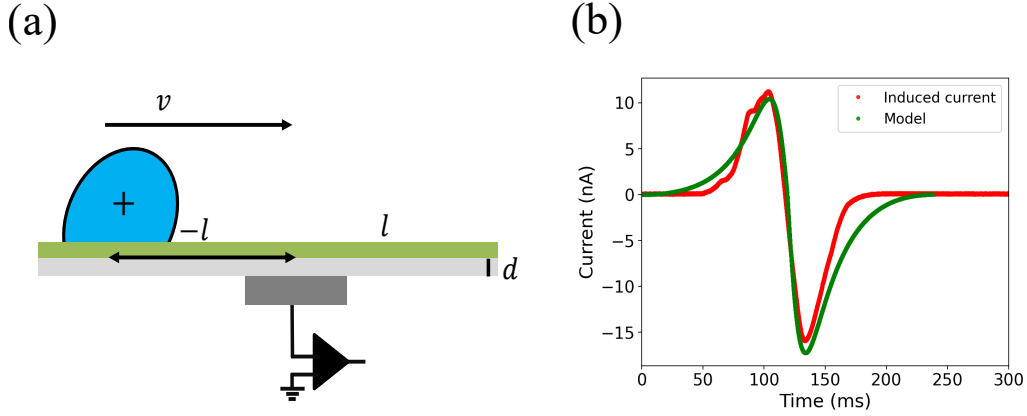


Figure 3.7: (a) Illustration of sliding plate capacitor model (b) Induced capacitive current shows good agreement with the sliding plate capacitor model.

3.2.5 Capacitance measurements

To measure the capacitance of the drop-substrate system, we conducted an experiment where we charged up the capacitor externally using a potential V , and measured the charge Q , in the capacitor system. Using Q and V for $45 \mu\text{L}$ drop, we estimated an average $C_D = 1.22 \pm 0.02 \text{ pF}$ and $C_D = 0.47 \pm 0.09 \text{ pF}$ for 1 and 3 mm glass substrate, respectively. Another way to estimate the capacitance is by using a plate capacitor approximation. We used the substrate dielectric $\epsilon_r \approx 7.0$ for soda lime glass, drop base area ($A = \pi lw/4$), and the glass thickness d in the following equation

$$C = \epsilon_0 \epsilon_r \frac{A}{d}, \quad (3.16)$$

which yields the approximated capacitance of our system $\approx 1.38 \text{ pF}$ and 0.48 pF for 1 and 3 mm substrate, respectively. The slight deviation from the measurement should be caused by the difference between sessile and moving drops. We further want to state that the measurement of such a small capacitance is highly susceptible to error. Thus, the good agreement of measurement and theoretical prediction confirms the parameter value.

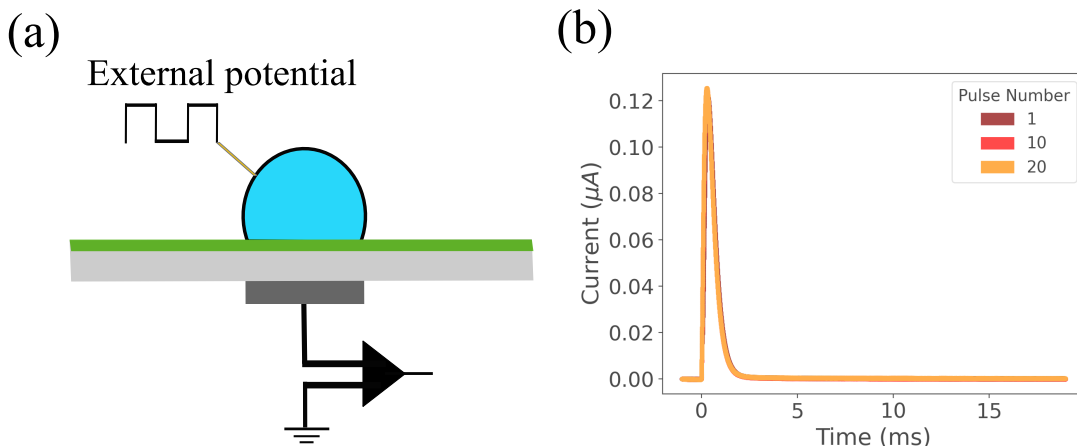


Figure 3.8: (a) Setup to measure the capacitance using the plate capacitor system. (b) Capacitive current caused by the 0-100V square potential.

3.3 Sample preparation

The investigation of slide electrification requires a surface with hydrophobic properties so that the drops slide off the surface. To investigate the charge separation, we used PFOTS (trichloro(1H,1H,2H,2H-perfluorooctyl) silane) coated substrate (Sigma-Aldrich Chemie GmbH, Eschenstrasse 5, Germany). To prepare the substrate, we used different types of glass slides, including microscopic float glass ($70 \times 20 \times 1$) mm^3 (Menzel glass, Thermo Fisher Scientific), long glass slides ($200 \times 20 \times 3$) mm^3 (window glass, prepared by a glass mechanic at Max-Planck-Institute for Polymer Research, unless mentioned otherwise), and quartz glass slides ($70 \times 20 \times 1$) mm^3 (Thermo Fisher Scientific). If the bottom metal plate in the experimental setup was not conductive enough, the glass slides were sputtered with a 35 nm layer of gold on the backside to ensure a good connection between the grounded plate and the glass.

We employed chemical vapour deposition (CVD) to coat the glass substrates with PFOTS. Prior to coating, we cleaned the substrates with acetone and ethanol. Afterward, we treated the cleaned substrates in an oxygen plasma cleaner for 10 minutes at 300 W power (Diener Electronics Plasma surface: Femto BLS, Ebhausen, Germany) to remove all organic compounds from the surface. Subsequently, the substrates, along with a 1 mL vial of PFOTS containing a magnetic stir bar, were placed in a vacuum desiccator. The desiccator was evacuated by a pump to a pressure of 100 mbar, causing the PFOTS to vaporize. The chamber was then left on a stir plate for 30 minutes to complete the silanization process. The PFOTS-coated substrate exhibited advanc-

ing and receding contact angles of $(117 \pm 2)^\circ$ and $(88 \pm 3)^\circ$, respectively. This was measured using a goniometer (Dataphysics, Germany).

To investigate the effect of different chemical groups on sliding electrification, we used a functionalized hydrophobic substrate. To synthesize the functionalized hydrophobic substrate, we first coated the glass substrate with PFOTS or hydrocarbon trichloro(propyl) silane (TCPS). Afterward, the secondary layer was synthesized by co-functionalization with (3-aminopropyl)-triethoxysilane (APTES). We avoided using only APTES due to its hydrophilicity. A fresh desiccator was used to avoid cross-contamination. APTES was deposited (1 mL) at ca. 11 cm from the centre. The pressure was then pumped down to ca. 50 mbar and kept for 6 hours. After functionalization, the glass substrates were kept under 50 mbar for 30 minutes without any silane to vent unreacted silanes. The coated glass substrates were then left to equilibrate with the ambient air environment ($T = 20^\circ\text{C}$, humidity = 30-70 %) for 5 days before testing. TCPS, and TCPS-APTES surfaces obtained after silanization has advancing and receding contact angles of $(93 \pm 3)^\circ$ and $(77 \pm 6)^\circ$, respectively. Similarly, PFOTS-APTES surfaces obtained after silanization had advancing and receding contact angles of $(111 \pm 3)^\circ$ and $(91 \pm 6)^\circ$, respectively. The surfaces were rinsed with ethanol and DI water after the silanization to remove unbounded silane layer before using them for the study.

Chapter 4

Parameter Exploration with Tilted Plate Experiments

To understand a new physical phenomenon, we should start with the observation of all its possible parametric dependencies. The aim of this chapter is to identify the important parameters of slide electrification using the tilted plate setup introduced by Stetten et al. We will explore three different experiments, focusing on parameters such as slide length, drop interval, and surface chemistry. These parameters play a crucial role in understanding the underlying mechanisms when constructing the slide electrification model. The results discussed here are also published in our work [38, 61].

For the experiment, we utilized the drop discharge method discussed in section 3.2.1. Here, grounded drops slid down inclined hydrophobic substrates, and after reaching a certain slide length, a probe electrode was used to discharge the drops. We integrated the discharge current over time to calculate the drop charge.

4.1 Slide length dependent drop charge

The first important observation of slide electrification is the slide length-dependent drop charge, which we call *drop charge traces*. The total charge of the drops sliding over a PFOTS-coated glass slide was measured at different slide lengths. In a typical experiment, we measured a drop charge at a certain slide length with a drop interval of $\Delta t = 2.1 \pm 0.2$ seconds. Then, we plotted the drop charge values as a function of slide length (see Fig.4.1). The figure shows drop charge traces for the 1st 5th 20th and 200th drops, respectively. Generally, the charge increased with slide length. The

first drop reached a saturation charge of around 1.5 nC after a few cm. We call this characteristic drop charge saturation length or surface charge decay length (L_{sat}). The successive drops after the first drop showed a slower saturation, i.e, longer L_{sat} than the first drops, and lower steady-state charge.

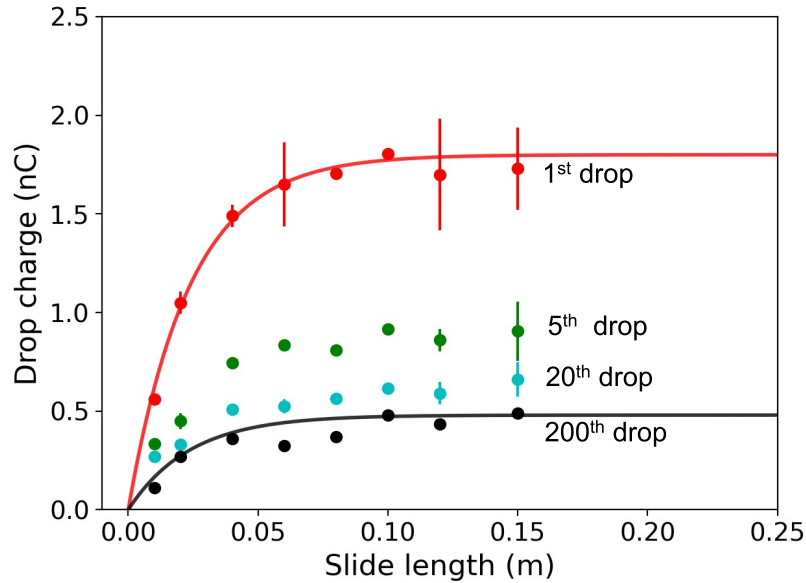


Figure 4.1: Drop charge traces of 1st 5th 20th and 200th drop measured at different slide lengths. The experiments were done at tilt angle of 50°, IAB for 5 minutes before every experiment.

This result is one of the important characteristics of slide electrification experiments, where drops only charge until a certain slide length, and then there is no exchange of charge between the solid surface and the drop.

4.2 Drop interval dependent drop charge

The second important observation of slide electrification is the drop-number and drop-interval dependent drop charge. The measurement for drops sliding at an interval time of $\Delta t = 1$ s showed a rapid decrease in the drop charge from 1.7 nC for the first drop, down through 0.75 nC, and eventually saturating at 0.26 nC for the 500th drop (see Fig. 4.2). Remarkably, changing Δt to 2 seconds led to an increase in drop charge, reaching 0.3 nC. Subsequent adjustments of Δt to 8 seconds and 29 seconds resulted in a further increase in drop charge, stabilizing at 0.65 nC and 1.1 nC, respectively.

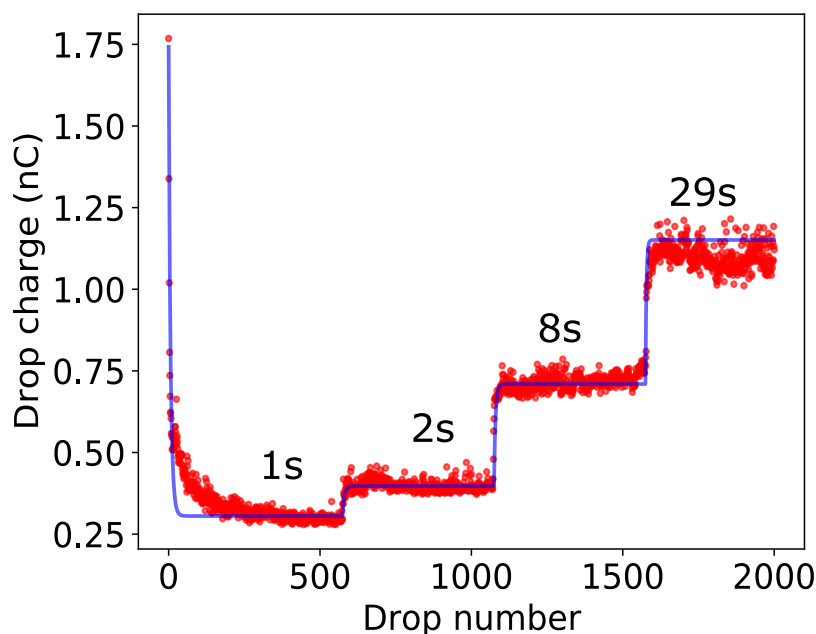


Figure 4.2: Stair experiment with changing Δt to study the drop charge dynamics in time measured at 15 cm slide length. The blue line serves as a guide for the eyes.

This behaviour of drop rate-dependent drop charge demonstrates the time dependence of charge separation.

A model that effectively captures this phenomenon is a capacitor with a specific relaxation time. In this model, the substrate accumulates a certain amount of negative charge through exchange with the drop, while the drop acquires positive charge. When the time between drops is less than the relaxation time of the surface, the subsequent drop has less possibility of charge transfer. With an increase in the time between drops, the surface can relax through various mechanisms, as we will explore later in chapter 7. Consequently, the drop can accumulate a higher charge with enough time between drops, and with a sufficiently extended time interval, each drop charge would closely resemble that of the initial drop.

4.3 Surface chemistry dependent drop charge

The third important observation is the surface chemistry-dependent drop charge. Typically, the protonation or deprotonation of the surface depends on the surface or the pH of the liquid. We conducted measurements on three different surfaces: TCPS, PFOTS modified with secondary layers of APTES, and TCPS modified with APTES

surfaces to understand the effect of the surface under the same pH. The results of the measurements were published in Langmuir [61].

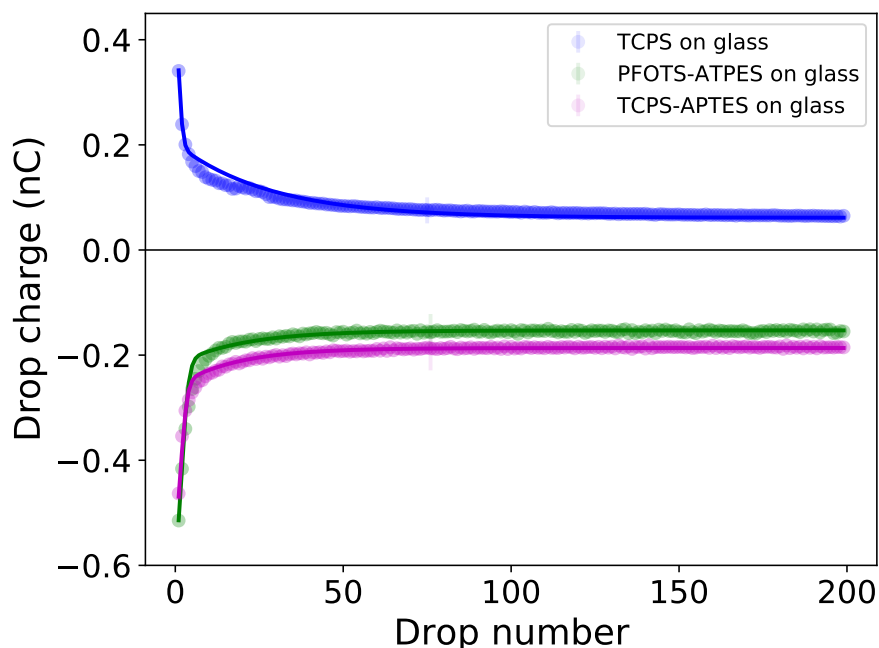


Figure 4.3: The drop charge on various surfaces coated on a glass substrate flips when the surface chemistry is altered. The figure is a modified version of the figure published by Wong et al. [61].

Positive drop charge:- The drop charge measured on TCPS showed a positive charge. Hydrocarbon (TCPS) surfaces exhibited a lower charge than the PFOTS surface. The initial drop charge was around 0.5 nC but decreased with an increasing drop number and got a steady-state of around 0.05 nC (see Fig.4.3). The positive drop charge on TCPS substrate is widely attributed to the autolysis of water on hydrophobic surfaces and the adsorption of the hydroxide ion, OH^- . It is assumed that a part of these adsorbed OH^- ions does not recombine at the receding side of the drop but remains on the surface. Therefore, a net surplus of protons, H^+ or H_3O^+ , is found in the departing drop.

Negative drop charge:- Drops sliding on hydrophobic surfaces, such as PFOTS/TCPS functionalized with APTES, which is an amino-containing silane, had a negative drop charge. Regardless of the underlying hydrophobic layer, in both APTES-functionalized surfaces, the drop charges were negative. The initial drop charge was around -0.6 nC, and with an increasing drop number, the charge decreased and reached a steady-state of around -0.16 nC (see Figure 4.3). The polarity flip induced by the functionalization of the amine (APTES) can be attributed to the active hydrolytic

protonation during contact with water. This reaction takes H^+ ions from the sliding drop and could be represented as $R-NH_2 + H^+ \rightarrow R-NH_3^+$. Therefore, resulting in negative drop charge.

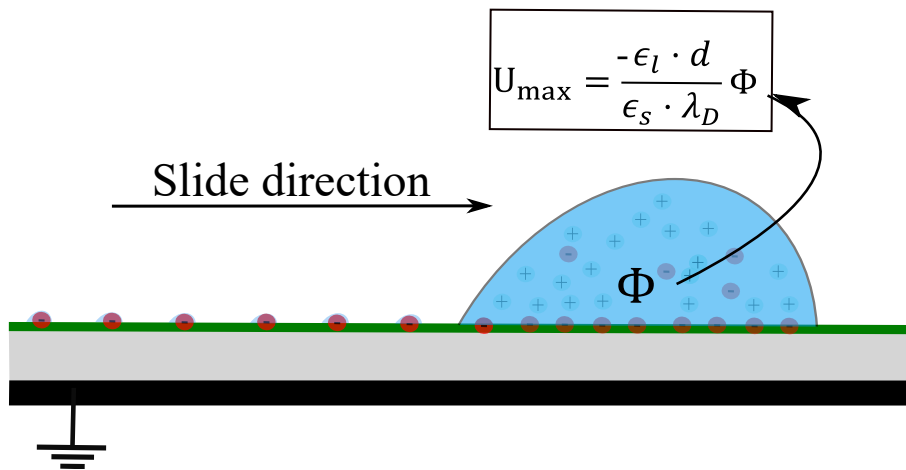
These experiments show that sliding drops with the same pH can charge differently with respect to the surface chemistry. This clearly suggests that the surface chemistry plays an important role in charging, and depending on the formation of this EDL, the drop charge polarity can flip.

4.4 Summary

Summarizing the experimental observations, we see that the EDL plays an important role in slide electrification. Similarly, parameters like drop slide length and the time between drops play crucial roles. We will use this knowledge in the following chapter to build a model describing slide electrification.

Chapter 5

Physical Model for Slide Electrification



The primary aim of the physical model is to understand the origin of charge separation. Here, we introduce a model to describe the origin of slide electrification and find the connection between the drop charge/potential to the EDL charge density and surface potential.

5.1 Two capacitor model

To understand the origin of drop charge/voltage, we develop a model for slide electrification based on a circuit-diagram, which allows identification of the microscopic

physical processes leading to drop charging.

Conceptually, slide electrification can be understood in terms of a voltage U_d , generated by the moving three-phase contact line (circuit diagram in Fig. 5.1). The charges at the solid-liquid interface within the EDL partially remain on the surface, and the mobile counter charges are pulled by the moving drop. Therefore, U_d can be understood as the electrostatic work that the moving contact line performs on the charges inside the drop. In our model, we assume that the contact line voltage moves charges between surface and drop. This is purely physical concept and does not tell about the chemical origin of such voltage. We will discuss its origin in detail in the later section 5.2. We furthermore assume that the charging is limited by the effective capacitance of the drop sitting on the hydrophobic substrate C_D , and the specific capacitance of the substrate $c_s = C_D/A_D$, with A_D as the drop contact area, respectively.

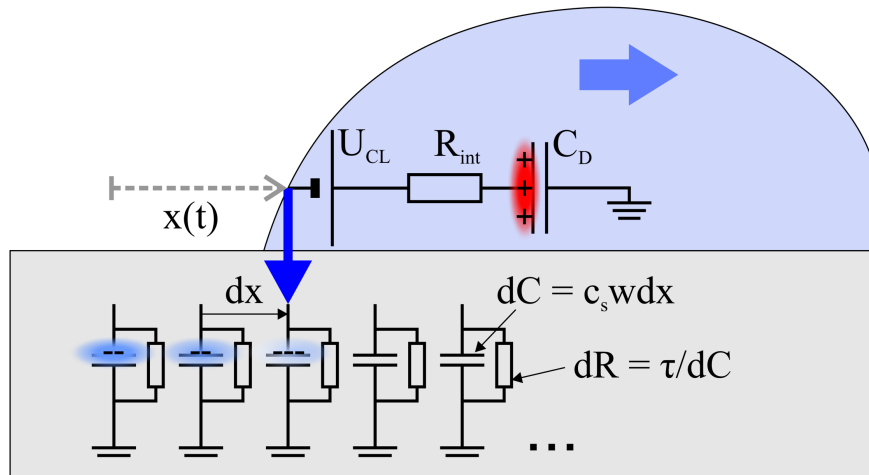


Figure 5.1: The circuit diagram describes the slide electrification model. The moving three-phase-contact line acts as a voltage source with a characteristic voltage U_{CL} , and internal resistance R_{int} , driving charges from the surface to the drop.

Charging of the first drop

At time zero for the first drop, both the drop and the surface are charge-neutral. The charging is then limited by available surface charges under the three-phase contact line and the transfer coefficient α . The maximum charging rate I_{max} occurs just as the

drop begins to slide and is coupled to the velocity v_D , and the width w , of the droplet:

$$I_{max} = \frac{dQ_D}{dt} = U_{cl}\alpha c_s w v_D = \frac{U_{cl}}{R_{int}}, \quad (5.1)$$

where $R_{int} = (\alpha c_s w v_D)^{-1}$ is the internal resistance of the voltage source.

As the drop continues to slide, it accumulates a charge Q_D , which generates a drop voltage $U_D = Q_D/C_D$. Thus, still assuming the neutral surface seen by the first drop, we can write:

$$U_{cl} = U_D + R_{int}I = \frac{Q_D}{C_D} + R_{int}\frac{dQ_D}{dt} \quad (5.2)$$

$$dQ_D = -\alpha(-U_{cl} + U_D)c_s w dx \quad (5.3)$$

In the last step, we used the definition for R_{int} and $v_D = dx/dt$. Equation (5.3) can be rearranged into a familiar form using L_{sat} :

$$\frac{dQ_D}{dx} + \frac{Q_D}{L_{sat}} = \alpha U_{cl} c_s w, \quad (5.4)$$

where L_{sat} is the drop charge saturation or surface charge decay length and is given as $L_{sat} = C_D/\alpha c_s w = A_D/\alpha w$. For circular geometry, it simplifies to $L_{sat} = \frac{\pi w}{4\alpha}$ [38].

Solving equation (5.4) yields a first-drop charge that exponentially saturates with distance, corresponding to the charge on a capacitor saturating with time following a voltage step:

$$Q_D^1(x) = -c_s U_{cl} w L_{sat} \left[1 - e^{-\frac{x}{L_{sat}}} \right] \quad (5.5)$$

Charging of successive drops

So far, we have ignored the effect of the surface charge density $\sigma(x)$, which also generates a voltage $U_s(x) = \sigma(x)/c_s$. For the first drop on a neutral surface ($\sigma_s^0 = 0$) U_s is zero. For the following drops with drop number n , we must include the surface charge that was left behind by the previous drops:

$$\sigma^n(x) = c_s U_s^n(x) = \sigma^{n-1}(x) \cdot e^{-\frac{\Delta t}{\tau}} \quad (5.6)$$

In the time between two drops Δt , the surface charge will gradually dissipate, e.g. through non-zero substrate or surface conductivity [93, 94, 95, 96] or by neutralization through ionic species in the air [97]. As a first-order approximation, we assume that these processes introduce an effective surface resistance dR on each surface element

dA , leading to an exponentially decaying surface charge with characteristic decay time $\tau = dRc_s dA$.

Including $U_s^n(x)$ in equation (5.2) yields the following differential equations for the n^{th} drop:

$$dQ^n = (U_{cl} - U_D^n(x) - U_s^n(x)) c_s w dx \quad (5.7)$$

$$\Delta\sigma^n(x) = -\frac{dQ}{w dx} = -(U_{cl} - U_D^n(x) - U_s^n(x)) c_s \quad (5.8)$$

Here $\Delta\sigma^n(x)$ denotes the change in surface charge caused by the n^{th} drop. We call equations (5.7) and (5.8) the *two capacitor model* for slide electrification. By substituting the contact line voltage with $U_{cl} = -\alpha_0/\alpha_1 C_D$, the drop voltage with $U_D^n(x) = Q_D^n/C_D$ and the surface voltage with $U_s^n(x) = \sigma^n(x)/c_s$, we can obtain the differential equations from Stetten et al. [14](equations (2.22) and (2.23)). The advantage of the two capacitor model over our previous model is that it uses easily accessible parameters physical parameters like drop/surface voltage and capacitance.

5.2 Origin of Three-phase contact line voltage

In the previous section, we derived a model to describe slide electrification and changes in drop and surface charge with successive drops. However, the physicochemical description of contact line voltage is incomplete. In this section, we elaborate on the origin of contact line voltage and demonstrate that the drop charge/voltage is related to the surface potential at the solid-liquid interface. This part of the discussion is published in "*High Voltages in Sliding Water Drops*", and some figures used in this section are from the publication [38].

5.2.1 Deriving the relation between drop charge/voltage potential and surface potential

The charge separation process seems to happen spontaneously against a strong electrostatic potential. To understand the process, we consider a single drop sliding on a neutral substrate. Because of charge conservation and the insulating nature of both the substrate and the surrounding air, any change in total drop charge dQ , is the result of surface charges σ_{out} , leaving the drop at the receding contact line. Thus, the

change in drop charge of a drop with diameter w , sliding a distance of dx , at location x can be expressed as

$$dQ(x) = -\sigma_{\text{out}}(x)w dx, \quad (5.9)$$

From our discussion in section 2.2, we know that solid surfaces in contact with liquid water acquire a net surface charge σ_{EDL} . This surface charge attracts counter ions and forms a diffuse layer. The characteristic decay of this diffuse layer is called the Debye length λ_D . It is thus reasonable to assume that a fraction $0 \leq \alpha \leq 1$ of the surface charge is deposited by the drop as it slides down the substrate [14, 64]. Assuming α to be constant during this process, we can write

$$\sigma_{\text{out}} = \alpha \sigma_{EDL} \quad (5.10)$$

To quantify σ_{EDL} , we consider Gauss' law at the solid-liquid interface,

$$\sigma_{EDL} = \mathbf{n} \cdot (\varepsilon_l \mathbf{E}_l - \varepsilon_s \mathbf{E}_s), \quad (5.11)$$

with the normal vector of the interface \mathbf{n} , and permittivity ε and electric field \mathbf{E} in the liquid (l) and solid (s), respectively. The electric field in the liquid \mathbf{E}_l , is governed by EDL. For moderate surface potentials $\Phi < k_B T$, we can use the linear approximation. Then, the electric field in the liquid scales like $\mathbf{n} \cdot \mathbf{E}_l = \Phi / \lambda_D$. Here k_B is the Boltzmann constant T is the temperature, and λ_D is the Debye length. For water with a monovalent salt at concentration c_0 , it is given by $\lambda_D = \sqrt{\varepsilon_l k_B T / (2c_0 e^2)}$. The electric field in the substrate \mathbf{E}_s , is determined by the potential difference between the drop with charge Q_D and the grounded plate under the substrate with thickness d (Fig.5.2), via $\mathbf{n} \cdot \mathbf{E}_s = -U_D / d$. Overall, the interfacial Gauss' law yields

$$\sigma_{EDL} = \varepsilon_l \frac{\Phi}{\lambda_D} + \varepsilon_s \frac{U_D}{d} \quad (5.12)$$

This relationship is general, as it only contains the assumption of a moderate surface potential. However, equation (5.12) has two free variables: the solid-liquid surface charge σ_{EDL} and surface potential Φ .

Generally, a change in the drop potential could also shift the chemical equilibrium at the solid-liquid interface, thus generating a non-linear response of both σ_{EDL} and Φ to the drop voltage U_D [98, 99]. This potentially complex process can be linearized for an approximately constant potential drop across the diffuse layer and thus approximately constant surface potential. In this case, the drop charge would saturate as a function of distance.

We assume that the voltage across the EDL is always identical to the surface potential Φ of a neutral drop. Using the surface charge within the drop (eq. 5.12), we

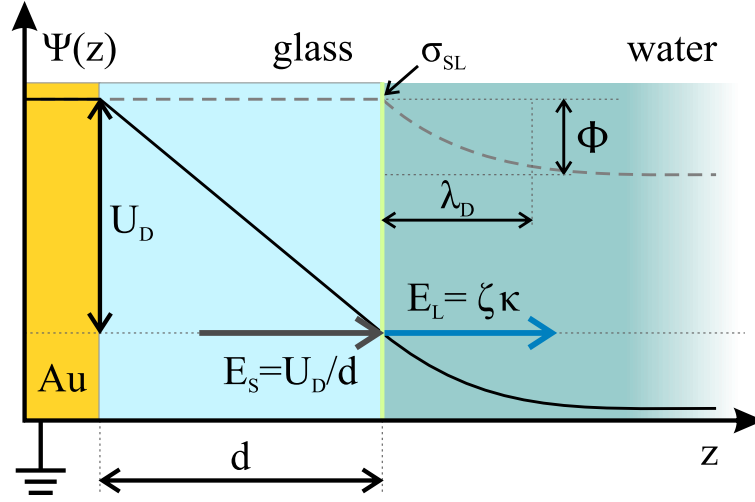


Figure 5.2: The illustration shows the electrostatic potential $\Psi(z)$ landscape in the proposed system. For an uncharged drop, the potential is flat throughout the substrate (dashed line). For a charged drop (solid line), there is an electric field present in the substrate, reducing the jump in the dielectric displacement and thereby amplifying the potential at the solid-liquid interface.

get

$$\sigma_{\text{out}} = \alpha \sigma_{\text{EDL}} = \alpha \left(\varepsilon_l \frac{\Phi}{\lambda_D} + \varepsilon_s \frac{U_D}{d} \right). \quad (5.13)$$

Inserting this into eq. (5.9), we arrive at the model equation for the drop charge:

$$dQ = -\alpha \left[\frac{\varepsilon_l}{\varepsilon_s} \frac{d}{\lambda_D} \Phi + U_D(x) \right] c_s w dx, \quad (5.14)$$

Here, $c_s = \varepsilon_s/d$ is the specific substrate capacitance. By comparing (5.14) and (5.3), we can observe that the contact line voltage U_{cl} discussed in section 5.1 is directly related to the surface potential Φ .

From equation (5.14), we can immediately see that the drop charge will be stationary ($dQ = 0$) at a maximum drop voltage of

$$U_{\text{max}} = -\chi \Phi, \quad (5.15)$$

$$\chi = \frac{\varepsilon_l}{\varepsilon_s} \frac{d}{\lambda_D}. \quad (5.16)$$

Here, we defined the amplification factor χ that is proportional to the ratio of the dielectric permittivities of liquid and substrate and the ratio of substrate thickness d and Debye length λ_D . By re-arranging equation (5.15) and using the drop-substrate capacitance $C_D = \varepsilon_s A/d$, we can find a similar relationship for the drop charge

$$Q_D = -\frac{\varepsilon_l A}{\lambda_D} \Phi = -C_{\text{EDL}} \Phi, \quad (5.17)$$

where C_{EDL} is the EDL capacitance within the drop.

Thus, by measuring the saturated drop charge or voltage after sufficiently long slide distance where $dQ = 0$ is valid, the surface potential of the solid-liquid interface can be determined. The proposed method is independent on the specific transfer coefficient α because once the drop has reached its steady state potential, no charge is transferred. The transfer coefficient only determines the characteristic slide length required to reach saturation state.

5.2.2 Surface Potential beyond the linear approximation

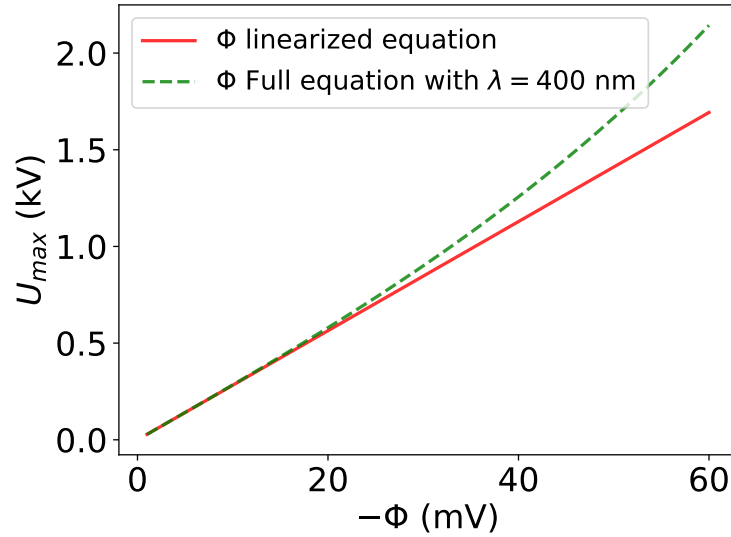


Figure 5.3: Comparison between the linear approximation and the full version of the equation shows that the approximation is valid within the uncertainty for low potentials, but deviates with increasing potential.

The relationship between surface potential and U_{\max} can be expanded beyond the linear approximation by considering Grahame's complete equation

$$\sigma_{\text{out}} = \alpha \left[\frac{2\varepsilon_l \varepsilon_0 k_B T}{e \lambda_D} \sinh \left(\frac{e\Phi}{2k_B T} \right) + \frac{\varepsilon_s}{d} U_{\max} \right]. \quad (5.18)$$

We can solve this equation for U_{\max} and get

$$U_{\max} = -\frac{\varepsilon_l d}{\varepsilon_s \lambda_D} \frac{2k_B T}{e} \sinh \left(\frac{e\Phi}{2k_B T} \right). \quad (5.19)$$

Linearizing this equation for low Φ ($\sinh(x) \approx x$) gives the equation that we saw in the previous section $U_{\max} = -\varepsilon_l d \Phi / \varepsilon_s \lambda_D$.

Comparing the maximum drop potentials for increasing Φ at $\lambda_D = 400$ nm and $pH \approx 6$, we observe that U_{\max} deviates from the linear equation with increasing surface potential. Nevertheless U_{\max} and Φ are linear for low potentials. For example, for $U_{\max} = 1$ kV, the linearized Φ is approximately -35 mV, while for the full model Φ is -33 mV, which falls within the uncertainty. Therefore, we use the linearized version of the equation for further analysis.

5.3 Measuring surface potential

The experimental setup is depicted in figure 3.2 (page 31) and discussed in detail in chapter 3. The experiments were conducted under ambient conditions, maintaining a temperature of $21 \pm 1^\circ\text{C}$ and humidity between 30-50%, where previous studies have reported minimal influence of humidity and temperature [35]. The PFOTS-coated glass substrate was positioned on an inclined grounded plate with a tilt angle of 50° . Surface charge neutralization was achieved by using an ionizing air blower (IAB, Simco-Ion Aerostat PC Ionizing air blower) for 2 minutes, ensuring an air ion concentration of $300,000$ ions/cm³ (measured with an Ionometer, IM806v3, 66687 Wadern, Germany). Afterward, we waited for a few minutes to allow ion dissipation in the air until an equilibrium air ion concentration (200-400 ions/cm³) was reached.

Subsequently, a peristaltic pump (Gilson Minipuls 3, Wisconsin, USA) was used to deliver deionized water (Sartorius Arium Pro VF, 18.2 M Ω resistivity, Germany $pH = 6.4 \pm 0.3$) into a grounded metallic syringe (diameter 2 mm). The needle produced water drops with a volume of 45 μL . As demonstrated in our previous work [30], the falling drops were electrically neutral. Notably, DI water rapidly absorbed CO₂ from the atmosphere [100, 101], leading to a pH of approximately 6, a value close to the measurements for the DI water used in our experiments.

The drops fell from a height of (0.5 ± 0.2) cm and slid for (1.0 ± 0.2) cm towards a grounding metal electrode, where they were neutralized. This allowed us to study only the charge of sliding drops and not from the rebound of falling drops. To minimize interference with drop motion, a thin metal grounding wire was selected. The grounding electrode served as the starting point of the slide length ($L = 0$). Drop dimensions, including width (w) and length (l), were measured using a calibrated telecentric high-speed camera. Previous studies from our group determined that for 45 μL drops, $w = 5$ mm, and $l = 6.7$ mm [14].

Following neutralization at the grounding electrode, the drops then slid a known

slide length ($L \pm 0.2$ cm) towards a gold-plated metal probe electrode. A laser trigger system was positioned 1 cm before the probe electrode and served as a trigger for data acquisition. Subsequently, the drop's charge and voltage were measured using the direct discharge method.

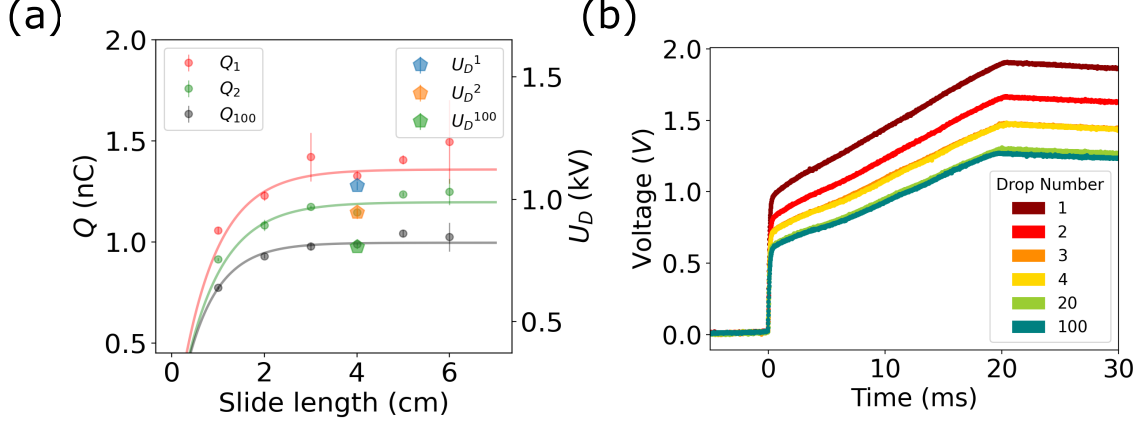


Figure 5.4: (a) Drop charge versus slide distance of the 1st, 2nd, and 100th drop, plotted with an exponential fit to obtain characteristic saturation length $L_{\text{sat}} = 7.0 \pm 0.3$ mm. (b) Voltage measured at C_{in} for multiple drops. The first jump to 1 V is due to the drop discharge; the following linear increase comes from the ongoing charge separation during drop sliding. We can calculate the initial drop voltage using the scaling factor ($\frac{C_{in}}{C_D} = 1125$) to be 1.1 kV.

The drop charge and voltage values as a function of slide length for different drops are shown in Figure 5.4a. The first drop sliding on a neutralized surface accumulated a maximum charge of 1.35 ± 0.03 nC over a distance of $L_{\text{sat}} = 7.0 \pm 0.3$ mm.

In contrast to measuring the drop charge, obtaining a reliable direct measurement of the drop voltage at such low charge values poses a greater challenge. It requires the use of a voltmeter with high input impedance and low stray capacitance. We tackle this challenge from two perspectives:

In the first approach, we measure the capacitance C_D , using a static drop with a bottom electrode positioned beneath the substrate (Fig. 3.8). In this setup, we apply an external voltage V , to the drop and measure the resulting image charge on the bottom electrode Q . This method allow us to determine a drop capacitance of $C_D = Q/V = 1.22 \pm 0.02$ pF, which aligns well with the theoretically estimated value using $C_D = \varepsilon_0 \varepsilon_r A_D/d = 1.17$ pF. using the measured capacitance and drop charge, we calculate the drop voltage as $U_D^1 = Q_D^1/C_D = 1.1$ kV.

In a second approach, we use a capacitive voltage divider to measure the drop

voltage. In this setup, a gold-plated metal electrode with an input capacitance of $C_{in} = 1.35 \text{ nF}$ is utilized to sense the drop potential (see Fig. 3.4 a). When the charged drop comes into contact with the metal electrode, it discharges into C_{in} until the voltages are equalized. The voltage-versus-time profile for the first drop (brown curve in Fig. 5.4b) exhibits a voltage jump within the first millisecond. This initial jump is because of the redistribution of the drop charge across the total capacitance. This is succeeded by a linear voltage increase, this linear increase is due to the ongoing charge separation at the moving contact line. As the drop passes beyond the electrode, the voltage signal exhibits a gradual decrease.

By utilizing the capacitance ratio $(C_{in} + C_D)/C_D \approx C_{in}/C_D$ for $C_{in} \gg C_D$, we estimate the initial voltage within C_D before its contact with C_{in} . These measurements yielded a drop voltage of $1.10 \pm 0.02 \text{ kV}$.

Both methods indicate that the sliding drops on PFOTS coated glass substrate spontaneously charge up to a significant voltage on the order of kilovolts. Utilizing experimentally obtained values ($\varepsilon_S = 7\varepsilon_0$ $\varepsilon_l = 80\varepsilon_0$ $d = 1 \text{ mm}$ $\lambda_D = 400 \pm 50 \text{ nm}$), we calculate a value of $\chi = \varepsilon_l d / \varepsilon_s \lambda_D \approx 28000$. With the measured saturation value of $U_D^{\max} = 1.1 \text{ kV}$, we can compute $\Phi = -38 \pm 5 \text{ mV}$, a value close to the zeta potential reported in the literature [101]. The uncertainty in surface potential was estimated using error propagation from λ_D , which was determined using the standard deviation in pH. Exact measurement of λ_D would help to further quantify the surface potential.

5.3.1 Influence of substrate thickness and salt concentration

The equations used to estimate the surface potential from drop potential (5.15 and 5.16) indicate that the saturation drop voltage is proportional to the substrate thickness d . We conducted a repetition of our measurements on a 3 mm thick glass substrate and observed a roughly threefold increase in the drop voltage to $3.8 \pm 0.1 \text{ kV}$ ($\Phi \approx -44 \text{ mV}$) (Fig. 5.5a). Interestingly, the measured drop charge remained almost constant.

Similarly, the model suggests a dependence of the saturation voltage on the Debye length. To test this relationship, we conducted experiments on the initial 1 mm thick substrate using drops with varying concentrations of KNO_3 . The voltage measurements revealed a decreasing voltage with increasing ion concentration, as shown in Figure 5.5b, aligning with findings in the literature [37]. In Figure 5.5b, the red dots represent the maximum voltage value on the pristine surface with DI water. We measured the voltage generated by the drops while increasing the salt concentration, and washing the surface between each measurement. Contrary to the model prediction, we

observed a decrease in voltage with increasing concentration.

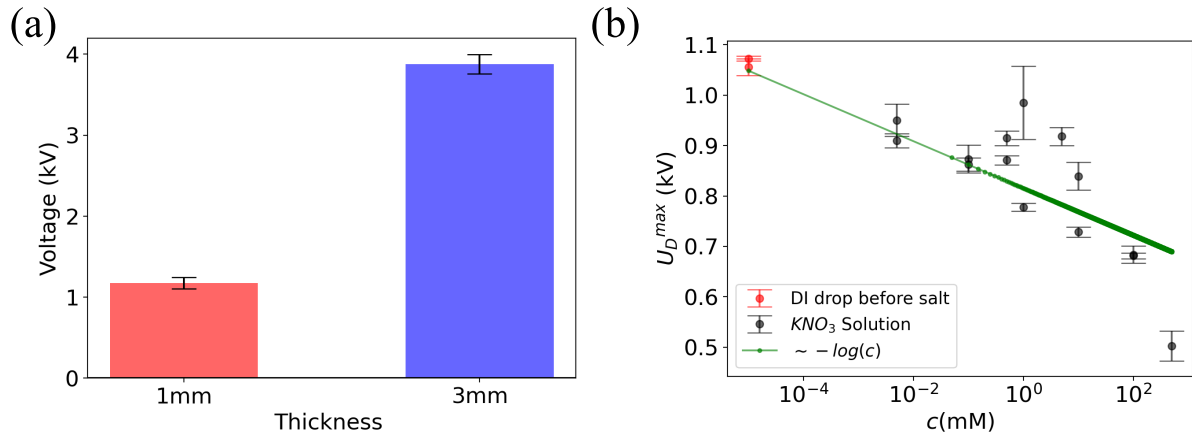


Figure 5.5: (a) Voltage comparison with different substrate thickness (b) Voltage U_D^{max} with increasing KNO_3 concentration

One reason for the deviation from the model prediction might be that our model's assumption of drop potential not shifting the chemical equilibrium at the solid-liquid interface could be violated with increasing concentration. Another reason is that we have assumed the Φ -potential is independent of the salt concentration c . However, it is well-known that changes in pH and ion concentrations affect the Φ -potential. This is because of shifted adsorption equilibrium due to counter-ions, which can also get adsorbed on the surface or in the Stern layer. At lower pH and higher ion concentrations, the empirical relation describing the relationship between surface potential and concentration is given by $\Phi \sim \lambda_D \sim c^{-1/2}$ [102]. For low ion concentration ($c < 10$ mM) solutions with $pH > 3.5$, this relationship is given by $\Phi \sim -\log(c)$ [103]. Our measurements were done in this regime; therefore, the behaviour of the saturation voltage would be proportional to Φ ($U_D^{max} \sim \Phi \sim -\log(c)$). Further study of these boundary conditions is needed to make the model more robust.

Most importantly, our interpretation of the saturation drop voltage offers an economical and straightforward experimental approach to investigate the dependencies of surface potentials on ion concentration. The model relies solely on substrate and solution properties as the only input parameters. Therefore, this method has the potential to be used for studying the intricate processes influencing surface potential.

5.3.2 Surface potential of different surfaces

We used the method discussed above with Debye length of 400 nm ($pH \simeq 6$) to estimate the surface potential of different hydrophobic surfaces in contact with DI

water. The uncertainties were estimated from the uncertainties in drop potential and $\Delta\lambda_D = 50$ nm. Figure 5.6 shows the surface potentials, where polystyrene (PS) and polydimethylsiloxane (PDMS) have negative surface potential. The values obtained for PS and PDMS are close to the values in the literature [103]. At the same time, the hydrophobic surface modified with APTES, which consists of amine groups, shows a positive surface potential. The observation is similar to the values reported in the literature [104, 105, 106]. The comparison shows that the method is valid for different types of hydrophobic surfaces.

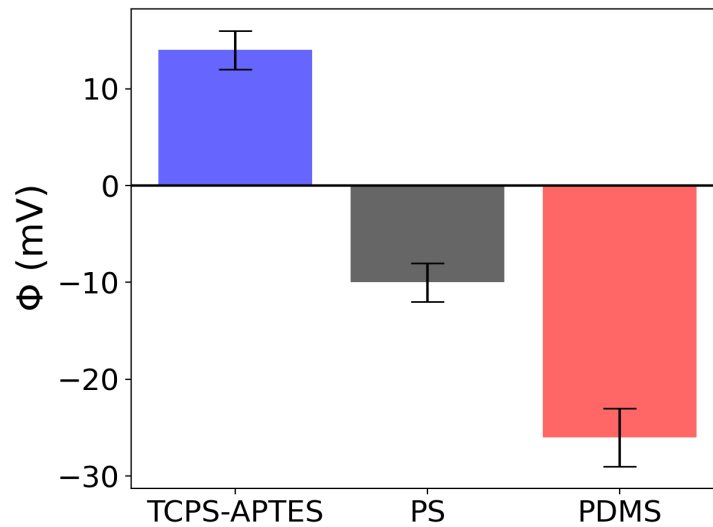


Figure 5.6: Surface potential of different hydrophobic surfaces

5.4 Series of drop sliding down the surface

When we allow multiple drops to slide on the surface at a time interval of $\Delta t = 1.8 \pm 0.2$ s, the drop charge/voltage exhibits a swift decline with the drop number, decreasing from 1.4 nC/1100 V to 1.1 nC/850 V within the initial ten drops (see Fig. 5.7 a, dots). Subsequent drops reach saturation at lower voltage levels, eventually stabilizing around 850 V. This decrease in charge/voltage can be attributed to the partial charge present on the surface from prior drops, thereby reducing the charge transfer.

Our measurements, as well as findings from previous studies, suggest that the surface charge on the dry substrate undergoes decay with a characteristic timescale τ ranging from 1 to 100 s [14]. This decay can be attributed to non-zero substrate or surface conductivity [94, 95, 96] or neutralization through ionic species present in the ambient air [97]. To incorporate these surface charges into the charge balance, we can

modify equation (5.14) for the n -th drop at position x :

$$dQ^n = \left[-\alpha c_s [\chi \Phi + U_D(x)] + \sigma_{\text{out}}^{n-1}(x) e^{-\frac{\Delta t}{\tau}} \right] w dx, \quad (5.20)$$

where Δt is the time in between two drops and $\sigma_{\text{out}}^0 = 0$ for initially uncharged substrates.

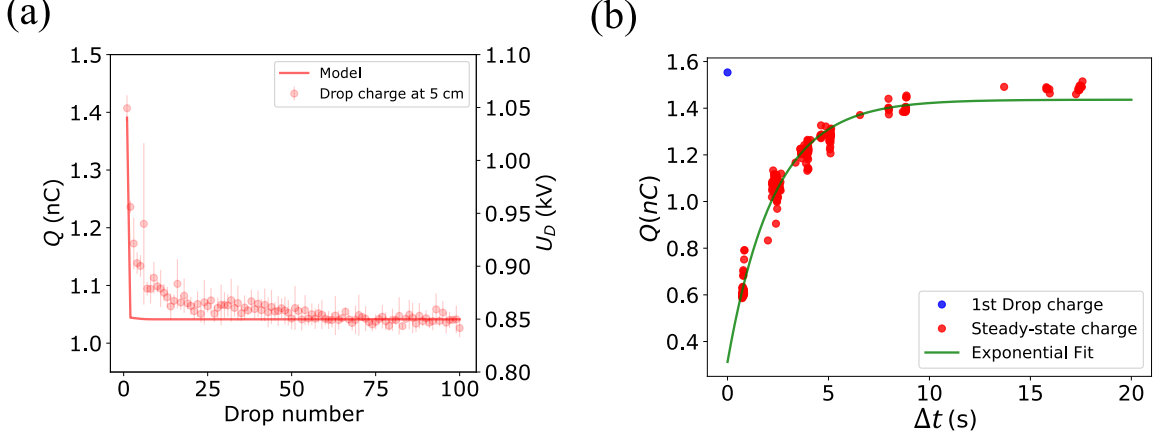


Figure 5.7: (a) Measured drop charge on PFOTS (dots) and numerical simulation (line) using the model. Parameters used for the simulation are $\Delta t = 1.8$ s, $C_D = 1.2$ pF, $\Phi = -40$ mV, and $\tau = 2.3$ s. (b) Steady-state drop charge (Q) vs. drop interval (Δt), and fit an exponential fit to obtain decay time

One approach to determining the discharge time scales involves examining the steady-state charge versus drop rate Δt . As the time between drops increases, the steady-state charge rises until it reaches the charge of the first drop Q_1 . This indicates the complete dissipation of surface charge between drops. This discharge time can be derived using the equation $Q(\Delta t) = Q(1 - e^{-\Delta t/\tau}) + Q_{\text{steady-state}}$, assuming the discharge follows an exponential process. Here, if $\Delta t \gg \tau$, then the drop charge would be at its maximum, and if $\Delta t \ll \tau$, then the drop charge reaches the steady-state value $Q_{\text{steady-state}}$. In this study, we conducted steady-state drop charge measurements versus Δt at a slide length of 4 cm, where saturation is expected to have occurred (see Fig. 5.7b). Through fitting, we determined the timescale to be $\tau = 2.3 \pm 0.2$ s.

After identifying important parameters relevant to slide electrification such as Φ , U_D , L_{sat} , and τ , we can employ eq. (5.20) in a numerical simulation. By considering the additional surface charge deposited during the electrode discharge (see details in later section 5.4.1), we observe notable agreement between simulation and experiment (Fig. 5.7a). Any deviations from the model could potentially be attributed to changes in velocity, possibly induced by electrostatic forces between the drop and surface charges,

as discussed by Li et al. [107]. Additionally, the observed behaviour is influenced by substrate polarization, an aspect we will delve into in detail later.

5.4.1 Numerical simulation

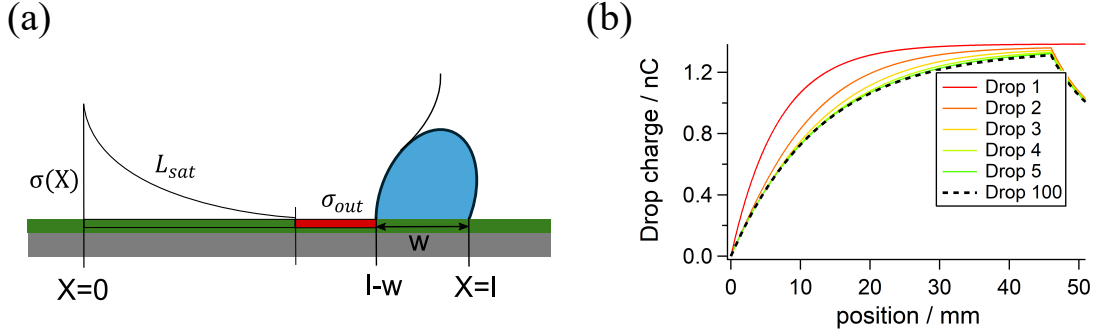


Figure 5.8: (a) Illustration of sliding drop with relevant length scales (b) Simulated drop charge traces of multiple drops

Both previous slide electrification models [14] and our new model fundamentally consist of a set of coupled differential equations for drop and surface charge. Based on these models, a set of analytical solutions for the first and steady-state drops can be derived. Due to the recursive nature of the equations,

$$dQ^n = [-\alpha c_s [\chi \Phi + U_D(x)] + \sigma_{out}^{n-1}(x) \exp(-\Delta t / \tau)] w dx \quad (5.21)$$

$$\sigma^n(x) = \sigma_{out}^n(x), \quad (5.22)$$

analytical solutions for every drop in a series of drops are difficult to calculate and yield complicated expressions. Furthermore, experiments with varying drop rate are impossible to simulate this way. Therefore, we wrote a simulation program in Igor Pro (wavemetrics) that solves equation (5.22) numerically, generating data sets of drop- and surface charge as a function of distance and drop number. Figure 5.8a shows the state and parameters used in the numerical simulation. As the drop with width w slides from $X = 0$, there is a charge exchange that decays exponentially with a decay rate L_{sat} due to the increasing drop potential. When we ground the drop, the drop potential goes to zero; therefore, the maximum possible surface charge $\sigma_{out} = \alpha \sigma_{EDL}$ is left on the surface. This process for multiple drops is also shown in the drop charge traces in Figure 5.8b.

An example of a simulation for a PFOTS surface is shown in figure 5.9. The figure shows the change in drop, and surface charge over the slide length for different times between drops Δt and drop numbers. Within this simulation, we also take into account

that the drop is discharged, as soon as it touches the measurement electrode. At this point in time, the receding contact line is located at a distance w before the electrode and starts to deposit the maximum amount of charges, as the drop is now discharged (red region on the right in Figure 5.9c). The advancing contact line of the following drop will pass this region of maximum surface charge before touching the electrode. This additional σ_{in} contribution reduces the drop charge before the electrode contact, modifying the measured drop charge.

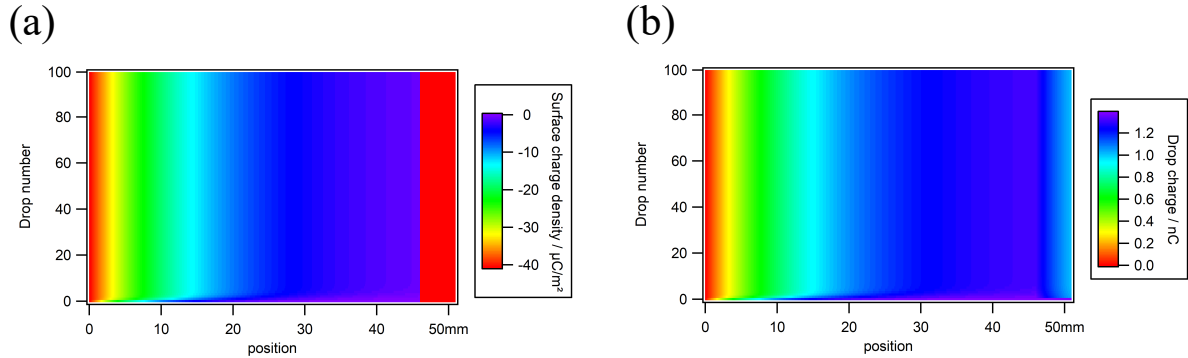


Figure 5.9: (a) Colour plot surface charge density (b) colour plot drop charge generated using numerical simulation

5.5 Energy harvesting

The implications of these findings are immediately relevant to energy harvesting from sliding drops. Previous studies have reported relatively low efficiencies of around 1% by comparing the potential energy of the falling drop with the electrical energy using a load resistor [108, 49]. The theoretical analysis presented here indicates that the saturation voltage increases proportionally to the substrate thickness (eq. 5.15), while the saturation charge Q depends solely on the wetted area and the properties of the EDL (eq. 5.17). Consequently, the total drop energy $W_D = \frac{1}{2}QU_D$ increases linearly with the substrate thickness.

In the current scenario, the drop charge saturates after sliding a height difference of $\Delta z = 3$ cm, resulting in a potential energy loss of $W_G = mg\Delta z = 13 \mu\text{J}$. The electrical energy on a 1 mm thick substrate is $W_D = 0.8 \mu\text{J}$, yielding an energy harvesting efficiency of 6%. By increasing the substrate thickness to 3 mm, the efficiency rises to 18%. It is important to note that an upper limit exists, as drops can become immobilized due to their own electrostatic field. Thus, to optimize this process, a delicate balance between drop motion and energy harvesting must be achieved.

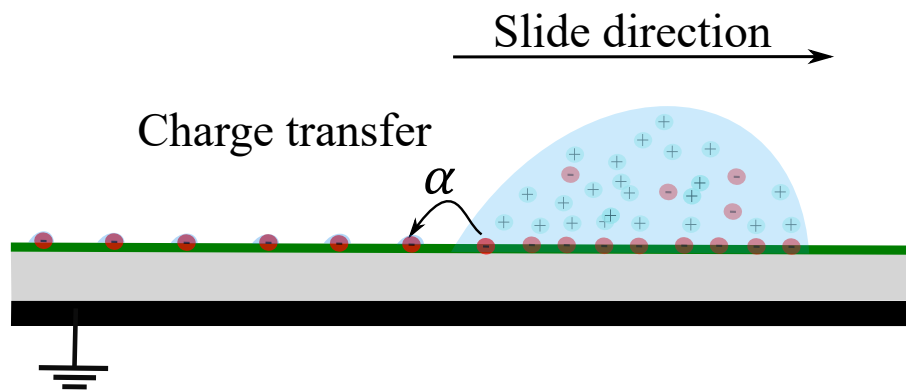
5.6 Summary

In this chapter, we present a slide electrification model based in a simple electrical circuit, capable of describing the experimentally observed drop charges/voltage of a series of water drops on hydrophobic surfaces. The charging dynamics of consecutive drops are influenced by residual surface charges that dissipate from the surface over a characteristic timescale of τ . Furthermore, we demonstrate that drops sliding over hydrophobic insulating surfaces attain voltages exceeding 1 kV across a distance of a few centimetres. The measured saturation drop voltage is an amplified surface potential at the solid-liquid interface. This amplification arises from the electrostatic potential landscape at the interface.

The straightforward electrostatic model developed in this study accurately captures the experimentally observed physics. The identification of kilovolt potentials in sliding drops, coupled with the presented model description, carries significant implications for energy applications, offering opportunities to optimize energy harvesting efficiency. Additionally, the theoretical description of the relationship between the measured saturation voltage U_D^{\max} and the surface potential have the potential to ignite a new research field by enabling low-cost surface/zeta potential measurements on flat surfaces.

Chapter 6

Charge Transfer Coefficient (α)



Another question concerning slide electrification is the rate of charge transfer from the EDL to the dry solid surface. This transfer rate is described by the charge transfer coefficient. The discussion in this chapter involves finding methods to estimate the surface charge density in the EDL and the surface charge density left on the dry surface. The transfer coefficient is given by the ratio between these two surface charge densities. Finally, we will explore different parameters such as sliding velocity and salt concentration that affect the transfer coefficient.

6.1 Quantifying surface charge densities

6.1.1 Surface charge density on EDL (σ_{EDL})

In the previous chapter, we derived the relationship between the drop charge/voltage to the surface potential. We can further explore the theory by using the linearized Grahame's equation, which we also discussed in theory section 2.2.4, for low potentials. This equation gives us the relation between the surface potential and the charge density

$$\sigma_{EDL} = \frac{\epsilon_0 \epsilon_L \Phi}{\lambda_D}. \quad (6.1)$$

Here, ϵ_L and ϵ_0 are the dielectric of liquid and vacuum, respectively. Combining this equation with eq.(5.16) ($U_{max} = -\epsilon_L d\Phi/\epsilon_s \lambda_d$), we obtain an equation to estimate the surface charge density in the EDL σ_{EDL} . We can express the relationship between the measured U_D^{max} and σ_{EDL} for the low potential case as follows:

$$\sigma_{EDL} = -U_D^{max} \cdot \frac{\epsilon_s \epsilon_0}{d} = -\frac{Q_{max}}{C_D} \cdot \frac{\epsilon_s \epsilon_0}{d} = -\frac{Q_{max} d}{\epsilon_s \epsilon_0 A} \cdot \frac{\epsilon_s \epsilon_0}{d} = -\frac{Q}{A}. \quad (6.2)$$

This equation offers a straightforward yet novel method to estimate the σ_{EDL} without knowing solid-liquid parameters such as the Debye length.

This is a powerful insight into slide electrification, demonstrating that the E-field in the substrate due to the drop charge compensates for σ_{EDL} . When the maximum drop charge/potential $Q_{max} \sim U_{max}$, is reached, the drop charge fully compensates the surface charge. Therefore, the net change in drop charge dQ after saturation, is zero.

6.1.2 Surface charge density left on dry surface (σ_{out})

As the grounded drop slides while touching the electrode, we measure a mean tail current I_{mean} , which is caused by the ongoing charge separation as the drop slides down the surface [64]. Then, the surface charge density σ_{out} , left on the dry surface by the receding contact line can be estimated using the following equation:

$$\sigma_{out} = \frac{I_{mean}}{w \cdot v}. \quad (6.3)$$

Here, w is the drop width, and v is the drop velocity. The drop velocity is measured using the laser trigger system placed a known distance of around 1 cm before the probe electrode. The two time points (laser trigger and probe signal) allow for a measurement of the average drop velocity as it traverses the 1 cm between them. The average drop

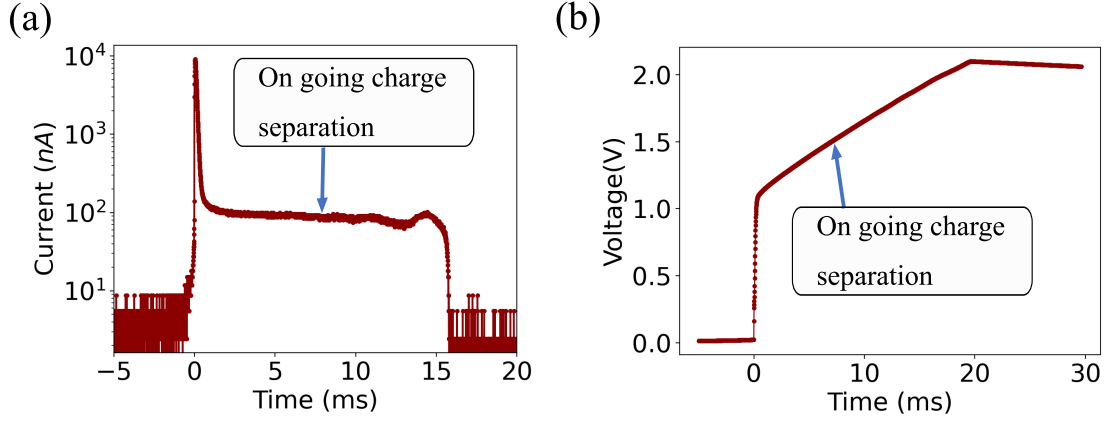


Figure 6.1: (a) Discharge current is measured by the direct drop discharge method, where the peak current represents the total accumulated drop charge, and the tail current represents the ongoing charge separation. (b) Voltage is measured in the external capacitor while touching the drop. The initial voltage jump represents the initial drop voltage, and the linear increase represents the ongoing charge separation.

velocities range from 0.1 m/s to 0.6 m/s, depending on the tilt angle. Due to mass conservation, we assume that the drop velocity is close to the dewetting velocity.

There are two different methods to measure mean current I_{mean} . The first one is by measuring the tail current of the grounded drop, as shown in figure 6.1a. This method was also used in one of our publications, where we studied the parametric dependencies of slide electrification [64].

The second method to measure I_{mean} is to measure the voltage over time using a capacitor voltage divider, as shown in figure 6.1b. Here, we measure the voltage V , in input capacitor C_{in} . The linear increase in voltage after the initial contact with the sliding drop is the ongoing charge separation, which increases the voltage in the input capacitor. The current due to this charge separation can be estimated as $I_{mean} = C_{in}dV/dt$.

Both the direct mean current measurement and the change in voltage measurement methods result in the same current value, which we can use to estimate the surface charge density left on the surface. One advantage of the voltage measurement method is that we can directly measure both σ_{EDL} and σ_{out} with a single measurement. First, C_{in} is measured externally or by using the known resistor R , as shown in figure 6.2a. Then, U_D^{max} and I_{mean} are estimated by fitting the signal shown in figure 6.2b with an equation.

$$V(t) = y * (1 - e^{-t/\tau_{in}}) + m * t. \quad (6.4)$$

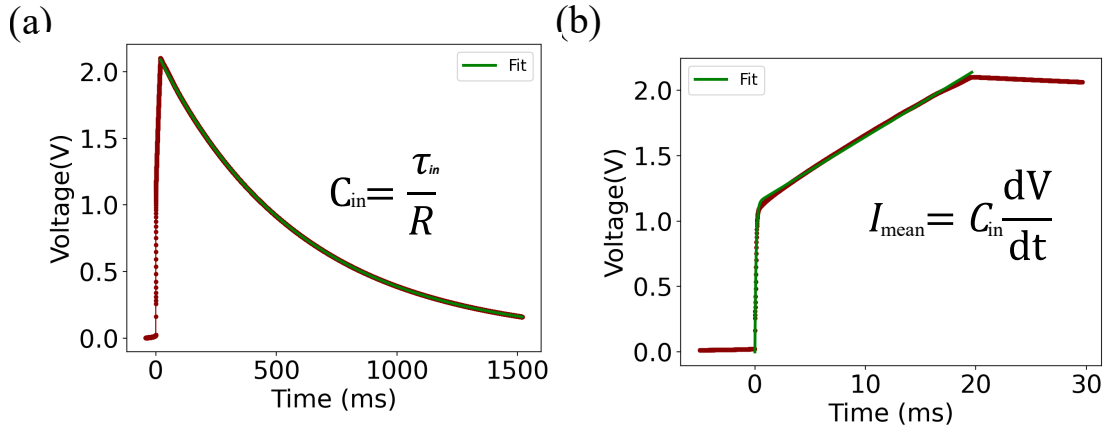


Figure 6.2: (a) Fitting the discharge time to estimate input capacitor C_{in} . (b) Fitting the voltage signal to obtain U_D^{\max} and I_{mean} .

Here, $\tau_{in} = C_{in}R$ is the capacitor charging time, the initial amplitude y , is proportional to U_D^{\max} , and the slope $m = I_{mean}/C_{in}$, is proportional to I_{mean} .

6.2 Quantifying charge transfer coefficient (α)

To understand the role of the charge transfer coefficient α , we can re-arrange eq.(5.14) from section 5.2, by using the drop capacitance $C_D = \varepsilon_s \pi w^2 / (4d) = \varepsilon_s A / d$ and the maximum drop charge $Q_D^{\max} = -\chi \Phi C_D$:

$$\frac{dQ}{dx} + \frac{Q_D(x)}{L_{sat}} = \frac{Q_D^{\max}}{L_{sat}} \quad (6.5)$$

Here, $L_{sat} = \frac{\pi w}{4\alpha}$ is the characteristic saturation length of the drop charge. By measuring the saturation length by fitting the drop charge vs slide length (Fig.5.4a) $L_{sat} = 7.0 \pm 0.3$ mm, and a drop width of $w = 5$ mm, we can estimate the charge transfer coefficient to be $\alpha \approx 0.5$. We compare this value with the measured value for DI water at a sliding velocity of 0.3 ± 0.02 m/s. We estimated $\alpha = 0.5 \pm 0.1$, which consistent with the value estimated using L_{sat} . The comparison between the theoretical predictions and the experimental values further confirms the methodology introduced in this chapter.

6.2.1 Charge transfer coefficient (α) behaviour with drop velocity

In our recently published work [64], we demonstrate that among different parameters such as contact angle and surface potential, drop velocity plays a crucial role in slide electrification. The drop velocity introduces the influence of advection and diffusion in the system, described in terms of the Péclet number $Pe = v\lambda_D/D$, where v is velocity λ_D is the Debye length, and D is ion diffusivity.

The interaction between advection and diffusion effectively influences the Debye length, as expressed by the following equation:

$$\lambda_{\text{eff}} = \lambda_D \frac{\sqrt{Pe^2 + 4} + Pe}{2}. \quad (6.6)$$

This equation predicts that the flow expands the diffuse layer near the contact line, exhibiting two different regimes based on velocity: $\lambda_{\text{eff}} \simeq \lambda_D$ for $Pe < 1$ and $\lambda_{\text{eff}} \simeq Pe\lambda_D$ for $Pe > 1$. This implies that the advective effect decreases charge separation beyond a certain velocity or Péclet number due to changing charge density and electrostatic potential. This effect was further validated in the publication using numerical simulation methods.

We further quantify α as a function of Pe by expanding the model presented in [64]. The charge density on the dry surface is a fraction ω ($\omega \in [0, 1]$), of the surface charge density at the contact line (σ_{CL}), given by:

$$\sigma_{\text{out}}(\theta, Pe) = \omega\sigma_{CL} = \omega \frac{\epsilon\epsilon_l\Phi}{\lambda_{\text{eff}}g(\theta)}. \quad (6.7)$$

Here, $g(\theta \approx 88^\circ) = \frac{\pi}{2\theta} \approx 1$ is the ratio of wall potential to surface charge density [109], and Φ is the potential in EDL. We solve equations (6.1), (6.6), and (6.7) to find an equation for α as a function of Pe :

$$\alpha = \frac{\sigma_{\text{out}}}{\sigma_{EDL}} = \omega \frac{2}{\sqrt{Pe^2 + 4} + Pe}. \quad (6.8)$$

Here, we assume that the total charge density in the fully charged drop is σ_{EDL} , as estimated using equation (6.1).

6.2.1.1 Experimental results

We conducted experiments with different tilt angles to change the sliding velocity. The transfer coefficient was then estimated using the mean tail current (Fig. 8.1) in equation (6.3). We used a 1mM NaCl aqueous solution for the experiment. Figure 6.3a illustrates the behaviour of the transfer coefficient with increasing drop velocity, where we observe a constant α within a certain velocity range. Beyond this range α decreases with increasing velocity.

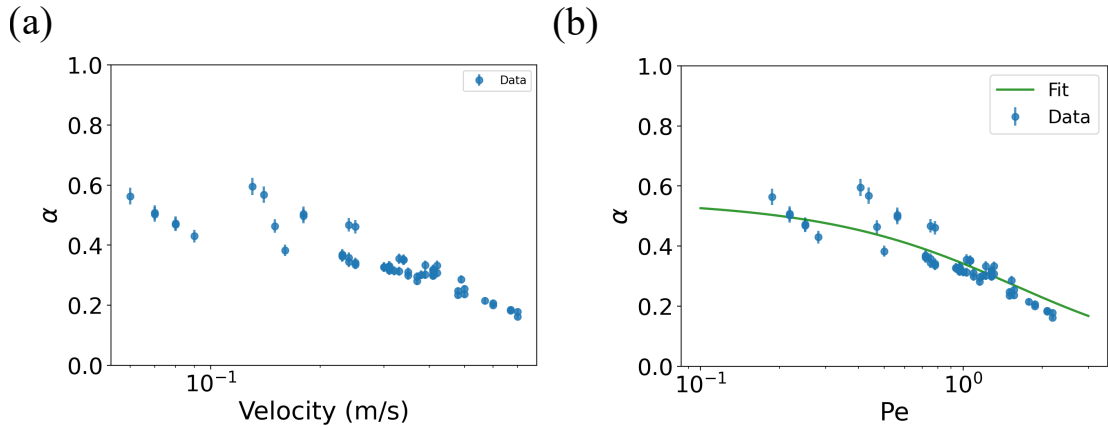


Figure 6.3: (a) Transfer coefficient with increasing drop velocity for the grounded drop (1mM NaCl) aqueous solution. (b) Transfer coefficient with increasing Pe and the fit with Equation (6.8), where $\lambda_{sol} = 9.7$ nm [64], and $D = 1.6 \cdot 10^{-9}$ m^2/s [110].

We use eq.(6.8) to fit the α vs Pe data with a fitting parameter ω in figure 6.3b. The model describes the experimental observations with $\omega \approx 0.7$. This experimentally observed relationship between α and Pe is well described by the theoretical description presented above.

This theoretical and experimental discussion shows that the charge separation process is not constant and changes with the sliding velocity. The reason for this change is the advection process, which increases the effective Debye length in the EDL. The advection process decreases the charge density at the contact line with increasing velocity/ Pe , hence also decreasing the charge density going out of the liquid. The discrepancy between σ_{CL} and σ_{out} is given by the factor ω . This factor might depend on effects at the atomic scale, the type of ion, the chemical composition of the surface, and the hydration cell around the ion on the surface. Further study with molecular dynamics simulations might be needed to quantify ω , and to compare with the values obtained in this work.

6.2.2 Charge transfer coefficient (α) behaviour with salt concentration

To investigate the impact of increasing salt concentration on slide electrification, we employed varying concentrations of KNO_3 aqueous solutions and compared surface charge density left on the surface σ_{out} , with the surface charge density left by DI water $\sigma_{out_{DI}}$. Following each concentration change, the surface was rinsed with DI water to mitigate the potential effects of surface degradation caused by the presence of salt.

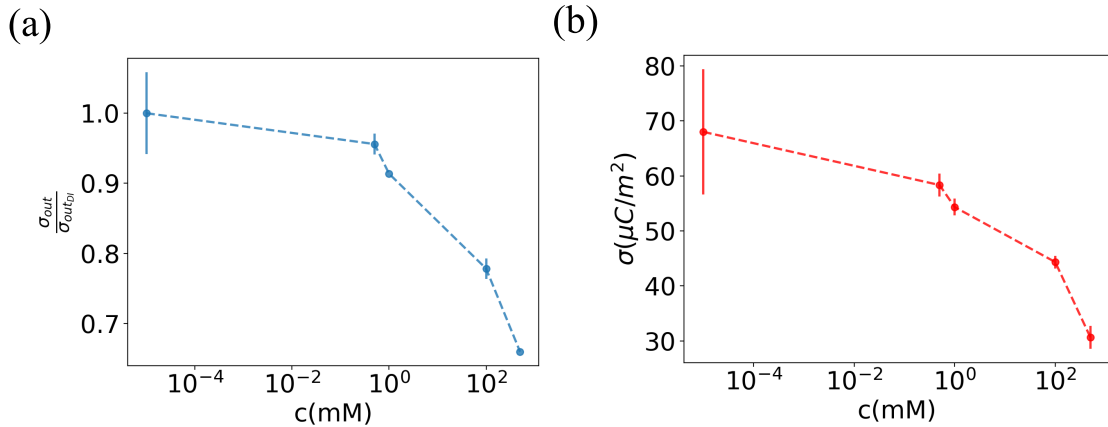


Figure 6.4: (a) Transfer coefficient with increasing KNO_3 concentration as compared to DI water. (b) Surface charge density in EDL with increasing salt concentration.

Normalizing σ_{out} with the increasing salt concentration by $\sigma_{out_{DI}}$ of the DI water, we observe that the ratio decreases with increasing concentration, as shown in figure 6.4a. This implies that the contact charge separation decreases with increasing concentration, as reported in the literature [36, 37, 39]. This decrease in charge separation might result from the decrease in σ_{EDL} with increasing salt concentration, as shown in figure 6.4b. The decrease in net σ_{EDL} can be attributed to two processes that might take place simultaneously: (i) as the concentration increases, the counter ions screen the surface charge in the diffuse layer, and (ii) the increase in ion concentration could also change the Stern layer, thereby modifying the net surface charge density [102].

6.3 Summary

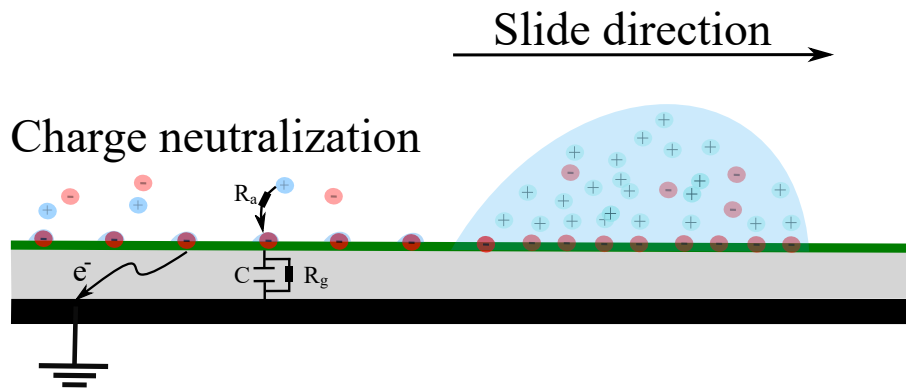
In this chapter, we discussed the charge transfer coefficient α , and a method to analyse the net surface charge density in the EDL. We demonstrate that by measuring the maximum drop voltage after a certain slide length, we can access the σ_{EDL} . We show

that the maximum drop charge/potential is reached when σ_{EDL} is compensated by the drop charge Q_{max} . Additionally, we show that the charge left on the dry surface can be measured using the tail current or the increase in voltage in the measuring capacitor as the drop slides down the surface. By comparing σ_{out} with σ_{EDL} , we can estimate α .

We further discussed the parameters affecting α , where we observe that it decreases with increasing drop velocity. We provide a model of diffusion and advection at the contact line to describe this behaviour. Similarly, we show that the charge separation decreases with increasing ion concentration, which might be attributed to the decreasing net surface charge density in the EDL.

Chapter 7

Surface Charge on Dewetted Surface & Charge Retention



An important aspect of slide electrification is the surface charge left on the solid surface as a drop dewets the surface. Here, we address one of the crucial questions: Where is the point of charge separation located? Furthermore, we explore the surface charge neutralization processes. We find that atmospheric ions, as well as substrate conductivity, play an important role in surface charge neutralization. Some parts and figures discussed in this chapter are published in "*Surface charge density and induced currents by self-charging sliding drops*" [69].

7.1 Surface charge density (σ_{out})

We use the capacitive current due to sliding droplet to measure the surface charge density σ_{out} , of different hydrophobic surface. Figure 7.1a illustrate the method, where a grounded and thus neutral drop slides over the dielectric coated glass substrate with a certain velocity. The velocity of the drop depends on the tilt angle and the hydrophobicity of the surface. A grounded drop sliding over the hydrophobic surface induces a capacitive current I_c , in the probe electrode, as shows in figure 7.1b. We integrate this current signal over time to estimate the charge and normalizing this charge using the area of the probe electrode with diameter ($d = 5$ mm), we estimate σ_{out} .

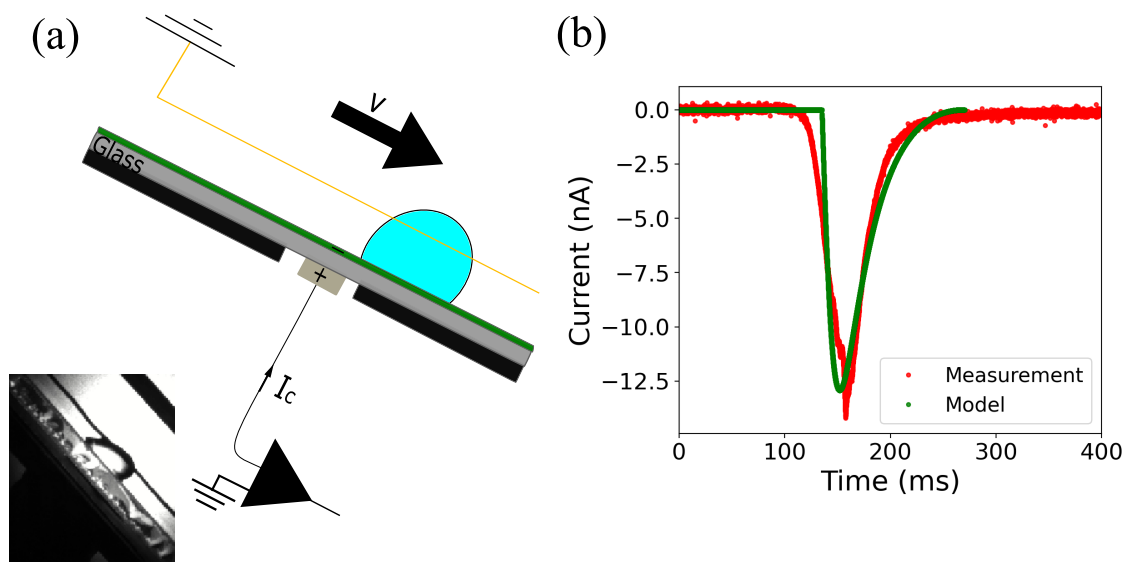


Figure 7.1: (a) Experimental setup to measure a capacitive current of sliding grounded drop. (b) Capacitive current of grounded drop sliding on top of the hydrophobic surface, and the modelled induced current using the model from section 3.2.4.

A grounded drop moving across the surface towards the metal electrode does not induce a positive current (figure 7.1b). This lack of a positive peak can be explained because there is no change in the electric field caused by the incoming neutral drop. However, as the drop moves over and away from the electrode, we can observe a negative peak. Here, the capacitive current that we measure is induced by the negative charge left by the drop at the receding contact line. This observation confirms that the charge separation only occurs as the sliding drop dewets the solid surface.

By continuously discharging the drop and keeping its potential at zero, the maximum charge separation is possible because there is no potential opposing the charge

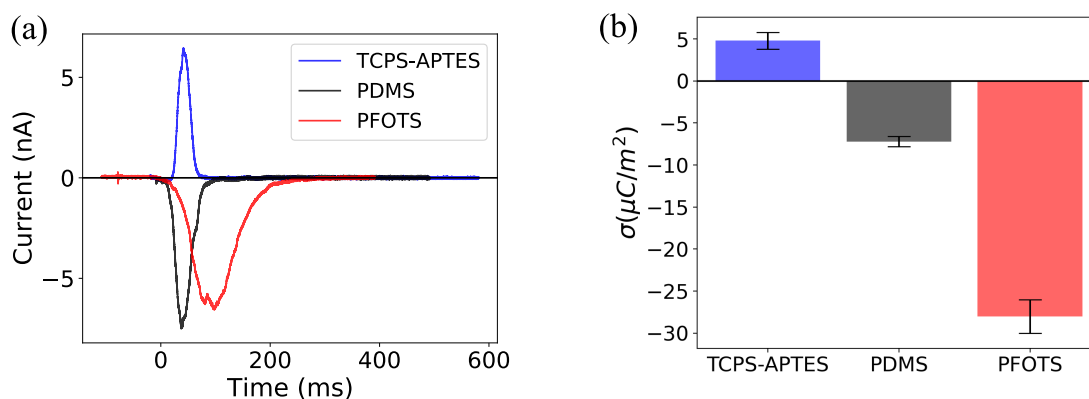


Figure 7.2: (a) Capacitive current induced by a grounded sliding drop on glass coated with various hydrophobic surfaces. (b) surface charge density σ , estimate integrating the current curves in (a). We observe that APTES has a positive surface charge density (positive current peak) whereas glass coated with PFOTS and PDMS has negative surface charge densities (negative peak).

separation [14, 38, 64]. We measured σ_{out} of various hydrophobic surfaces using this method. The surface charge density of PFOTS coated glass substrate is $-28 \pm 2 \mu\text{C}/\text{m}^2$. We further compared the measured surface charge density with the equilibrium charge density in solid-liquid contact line, which we estimated using the Grahame equation. The Grahame equation gives us the relation between the surface potential and the charge density

$$\sigma_{EDL} = \frac{2\epsilon_L\epsilon_0k_B T}{e\lambda_D} \sinh\left(\frac{e\zeta}{2k_B T}\right). \quad (7.1)$$

Here, ϵ_L and ϵ_0 are the dielectric of liquid and vacuum, respectively. For this comparison, we used the zeta potential $\zeta = -36 \text{ mV}$ at $\text{pH} \approx 5.5$ as reported by Vogel et al. [101]. Using this ζ -potential and a typical Debye length of $\lambda_D = 200 - 500 \text{ nm}$ of DI water in eq. (7.1), we estimated the surface charge density to be around -130 to $-55 \mu\text{C}/\text{m}^2$. The comparison shows that all such measurements yielded 20-50 % of the total charge density from EDL is left behind on the PFOTS coated substrate. Hence, understanding this fraction α , and increasing it could help to increase the solid-liquid charge separation.

We also determined the surface charge density of several other hydrophobized glass surfaces. In Figure 7.7b, the surface charge densities of trichloro(propyl)silane (TCPS), (3-aminopropyl)triethoxysilane (APTES), Polydimethylsiloxane (PDMS), and fluorocarbon (trichloro(1H,1H,2H,2H-perfluorooctyl)silane (PFOTS)) are illustrated. A positive surface charge density $\sigma_{out} = 5 \pm 1 : \mu\text{C}/\text{m}^2$, was measured for TCPS-APTES,

possibly due to the presence of amino groups on the surface. Previous studies have reported that the introduction of APTES can increase the surface charge density to a positive value, such as in PDMS coated with APTES [106, 104]. Conversely, the measured negative surface charge density for PDMS $\sigma_{out} = -7 \pm 1 : \mu C/m^2$, can be attributed to the presence of hydrocarbon groups on the surface. These measurements highlight the correlation between surface chemistry and slide electrification, consistent with our discussion in previous chapters. Here, we provide an alternative method to study the slide electrification.

7.2 Surface neutralization/discharge time

Let us consider drops sliding on a hydrophobic substrate. Because of charge conservation and the insulating nature of both the substrate and the surrounding air, any change in total drop charge, is the result of surface charges leaving and entering the drop. The charge density left on the surface is a fraction α , of the charge density in the EDL, and can be expressed as

$$\sigma_{out} = \alpha\sigma_{EDL}. \quad (7.2)$$

Then, the change in surface charge density as n^{th} drop slides at location x can be written as

$$\Delta\sigma_n = [\sigma_{in_n}(x) - \sigma_{out_n}(x)] \quad (7.3)$$

where σ_{in_n} and σ_{out_n} are the surface charges entering the drop via the advancing contact line and leaving the drop at the receding contact line, respectively. They are equal to the surface charge densities of the solid-air interface directly before and behind the drop. For the first drop, there is no surface charge entering the drop $\sigma_{in_1} = 0$.

As multiple drops slide down the surface, we must consider the surface charge caused by previous drops, denoted by σ_{in_n} , which we also discussed in the previous chapter (see section 5.4). During the time interval between successive drops, denoted by Δt , the surface loses some of the surface charges through discharge processes such as finite conduction through the substrate [93, 94, 95, 96] or atmospheric ions induced by cosmic rays [97]. Assuming such discharge processes follow an exponential decay with a surface discharge time τ , we can estimate the surface charge density for the next drop as follows:

$$\sigma_{in_n} = \sigma_{out_{n-1}} \cdot e^{\left(\frac{-\Delta t}{\tau}\right)}. \quad (7.4)$$

Combining eq.(7.3) and eq.(7.4) and the same amount of charge left by the grounded drop, we obtain the change in surface charge density

$$\Delta\sigma_n = \sigma_{in_n} - \sigma_{out_n} = \sigma_{out} \cdot \left(e^{-\frac{\Delta t}{\tau}} - 1 \right). \quad (7.5)$$

A way to measure the surface discharge time τ is to measure $\Delta\sigma$ with increasing time between drops Δt , as shown in figure 7.3a. When the time between drops is less than the discharge time ($\Delta t \ll \tau$), the steady-state $\Delta\sigma$ is around $-11 \mu\text{C}/\text{m}^2$ (Fig. 7.3b). For $\Delta t \ll \tau$, $\Delta\sigma$ tends to zero. This is also observed in steady-state $\Delta\sigma$ in figure 7.4 a/b. As the time between drops increases, the surface has more time to be neutralized. Hence, for the next drop, $\Delta\sigma$ increases. Given enough time between drops ($\Delta t \gg \tau$), then $\Delta\sigma = -\sigma_{out}$ (Fig. 7.3a). Here, we estimated the surface discharge time $\tau = 2.4 \pm 0.2$ s for PFOTS coated glass substrate at 46% relative humidity by fitting the data in figure 7.3a (black dots).

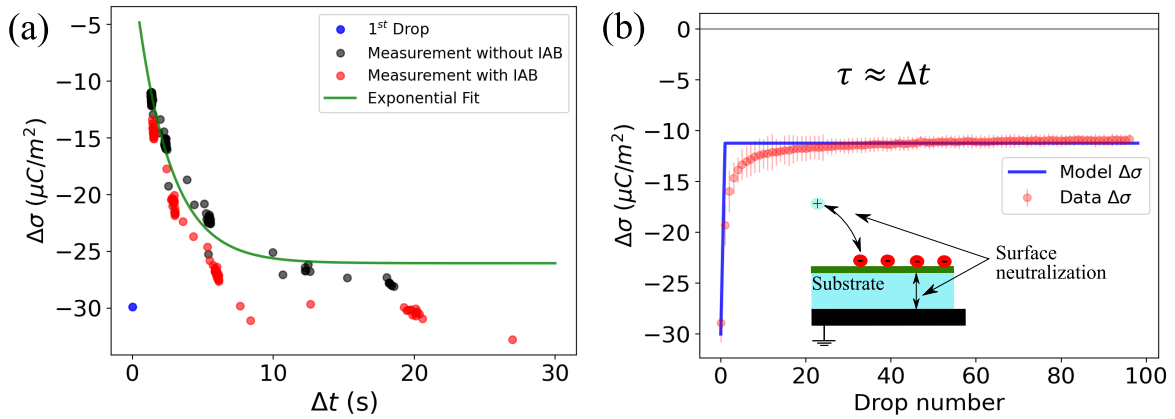


Figure 7.3: (a) Measurement in float glass substrate. Steady-state $\Delta\sigma$ with increasing time between subsequent drops Δt . The first drop, with $\sigma_{in} = 0$, is represented by a blue point. Measured data is fitted using eq.(7.5) (b) Change in surface charge density, $\Delta\sigma$ (red dots) of PFOTS on float glass with increasing drop number and model (blue line). Parameters used for the modelling are $\sigma_{out} = -28 \frac{\mu\text{C}}{\text{m}^2}$, $\tau = 2.5$ s.

Measuring $\Delta\sigma$ on PFOTS-coated 1 mm thick quartz slides (ThermoScientific) reveals different behaviour, as depicted by the black dots in figure 7.4a and 7.4b. In this case, the surface charge density for the first drop is similar to that of the float glass. However, with increasing Δt , saturated $\Delta\sigma$ does not increase, as seen with float glass. This indicates that the surface becomes fully charged, and between drops, it is unable to discharge. Hence, quartz exhibits a longer τ compared to float glass. This can also be observed in figure 7.4b, where $\Delta\sigma$ saturates within two drops to zero for $\Delta t \approx 2$ s.

This observation clearly suggests that the substrate used for coating influences the surface discharge time. Here, the surface discharge time could be understood as a

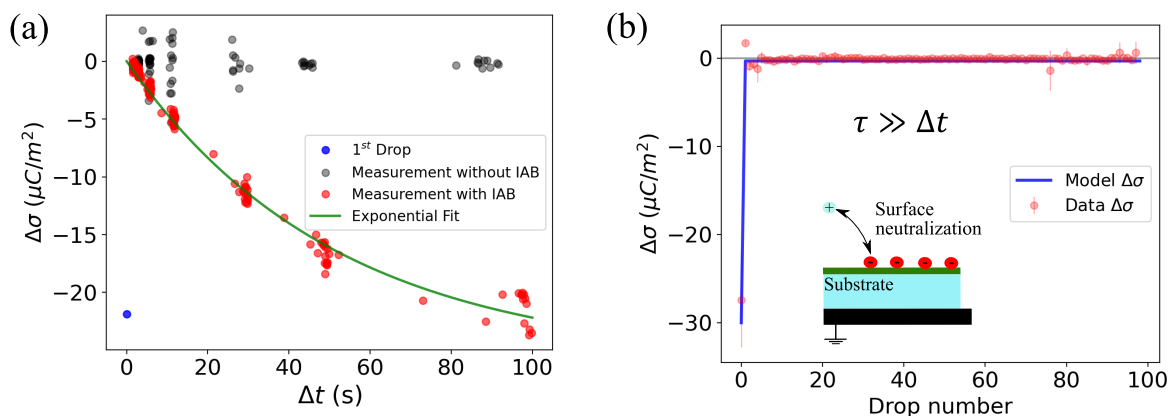


Figure 7.4: (a) Measurement in quartz glass substrate: Steady-state $\Delta\sigma$ with increasing time between drop Δt . The first drop (blue point) shows the $\Delta\sigma$ after the first drop as red dots shows the $\Delta\sigma$ at different Δt with ionizing air blower (IAB) running in the background. Black dots show $\Delta\sigma$ with increasing Δt but without IAB running in the background. (b) Measured $\Delta\sigma$ (red dots) and model (blue line) on PFOTS on quartz with $\sigma_{out} = -28 \frac{\mu\text{C}}{\text{m}^2}$, and discharge time of $\tau \approx 100$ s.

capacitor discharge time, determined by the substrate's capacitance C and resistance R . To verify this argument, we measured the resistivity and capacitance of both float glass and quartz substrates. We applied an external voltage of 200 V to a stationary drop for 10 s and measured the capacitive current from beneath the substrate (figure 7.5). The measurements on float glass revealed a resistance of $R \approx 2.5 \cdot 10^{12}$ Ohms. Using a capacitance $C \approx 1.2$ pF (calculated as $C = \epsilon_0 \epsilon_r A/d$), we estimated the discharge time to be 3 s, which closely aligns with the value obtained from the fit in figure 7.3a.

Interestingly, performing the same estimation in quartz using $R \approx 10^{14}$ Ohms and $C \approx 0.7$ pF reveals a discharge time of hundreds of seconds. The difference in resistance can explain the variations observed in $\Delta\sigma$ vs. drop number between float and quartz in figure 7.3b and 7.4b. This observation also emphasizes the significant role of the substrate in the surface discharging process. Using a low-resistive substrate could be a promising approach to optimize the charge separation process in series of drops and could thus increase energy harvesting efficiency.

To further understand the influence of atmospheric ions in the discharge process, we conducted an experiment with increasing Δt in two different configurations: one with an ionizing air blower (IAB) turned on during the experiment and another without the IAB. The IAB was positioned at a 45° angle relative to the inclined plate to minimize the effect of moving air on sliding drops. More than $300000 \text{ ions}/\text{cm}^3$ atmospheric

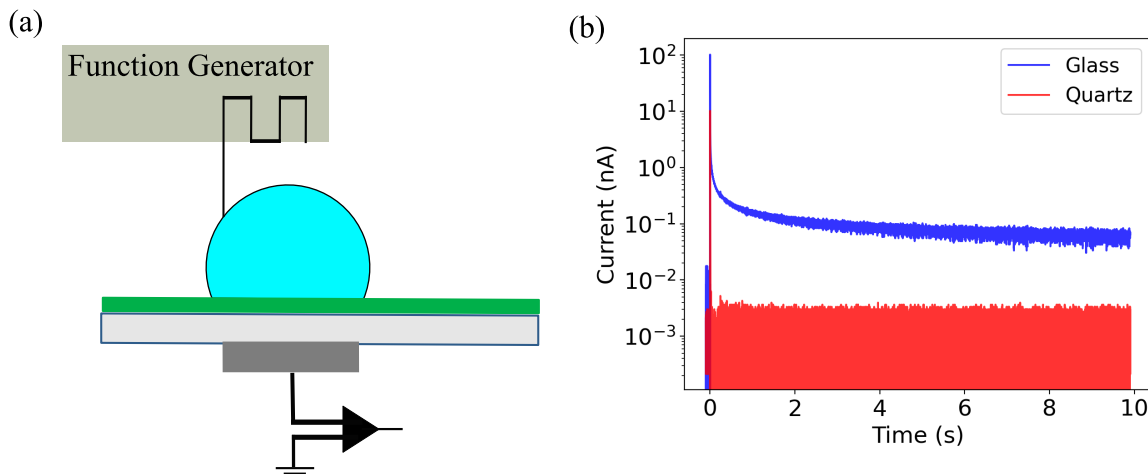


Figure 7.5: (a) Setup to measure capacitive current due to applied voltage (b) Current for 10 s while applying external potential of 200 V

ions were measured using an Ionometer (IM806v3, 66687 Wadern, Germany) while ruining the IAB.

In Figure 7.3a and 7.4a, the black dots represent the measurements without the IAB, and the red dots show the measurements with the IAB. In the case of glass, using the IAB has little effect on the discharge process because the discharge through glass is dominant. However, in the case of quartz, where the discharge through the substrate is considerably slower, the discharge through atmospheric ions seems to play an important role. To determine the discharge time on quartz substrate in the presence of the IAB, we fitted the data (red dots) with an exponential curve (Fig. 7.4a) and estimated the discharge time to be approximately 50 s.

These experiments clearly demonstrate that both atmospheric ions and the substrate play roles in the surface discharging process. However, under normal atmospheric conditions, the influence of the substrate is much greater than that of the air ions. It also highlights that quartz can effectively hold the charge for an extended period. Interestingly, this does not seem to be the case in float glass. The discharge time in float glass is only a few seconds, and atmospheric ions play a minimal role in this scenario. This also shows us that there is a way to tune the drop charge using the substrate with different properties.

substrate polarization effect- Generally, float glass consists of many ionic components mixed with silicon dioxide. Due to these impurities in float glass, it is possible for the ionic components to become polarized under the electric field and potential within the glass, as surface charge is left by the sliding drop. If we assume that the

polarization depends on the surface charge and its decay time, we can modify the equation for the change in surface charge as follows:

$$\Delta\sigma_n = \left[\sigma_{\text{out}} \left(e^{\left(\frac{-dt}{\tau}\right)} - 1 \right) - \sigma_{\text{sub}_{n-1}} \right]. \quad (7.6)$$

Here, σ_{sub} is the substrate polarization due to surface charge after each drop and given by:

$$\sigma_{\text{sub}_{n-1}} = \left(\sigma_{\text{in}_n} - \sigma_{\text{out}} \right) \cdot e^{-n\Delta t/\tau}. \quad (7.7)$$

Here, we assume that surface polarization depends on the drop number because each drop polarizes the substrate while sliding, and the substrate depolarizes over time with the same discharge time as the surface.

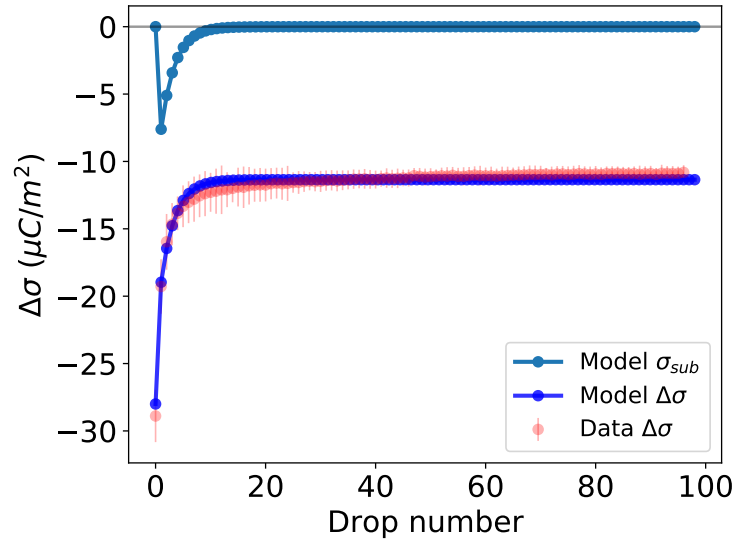


Figure 7.6: Comparison of modified model with experimental observations

Figure 7.6 shows the numerical simulation using the modified model along with the corresponding experimental data, represented by red dots. It is evident that the modified model offers a reliable description of the data. But, this modified theory depends on the substrate and its impurities. Further exploration of substrate polarization would help to better understated the discharge process.

7.3 Surface charge decay length(L_{sat})

To understand how surface charge density σ_{S1} , of the first drop changes as the drop slides down the surface, we locally measured the σ_{S1} left by the self-charging drop at different slide lengths. 'Self-charging' means that we initially ground the drop and

then allow the charged drop to slide down the surface. To estimate σ_{S1} at a particular slide length, we first measured the capacitive current due to incoming and outgoing drop, as shown in figure 7.7a. At the start of every measurement, we measured a background signal to determine the amplifier offset. In figure 7.7a, "Background" represents the offset, and "Drop 1" represents the first drop sliding down the surface. The background signal does not show capacitive current flow, whereas the sliding drop produces a considerable current flow. We subtracted that from the background noise and integrated the capacitive current to estimated σ_{S1} .

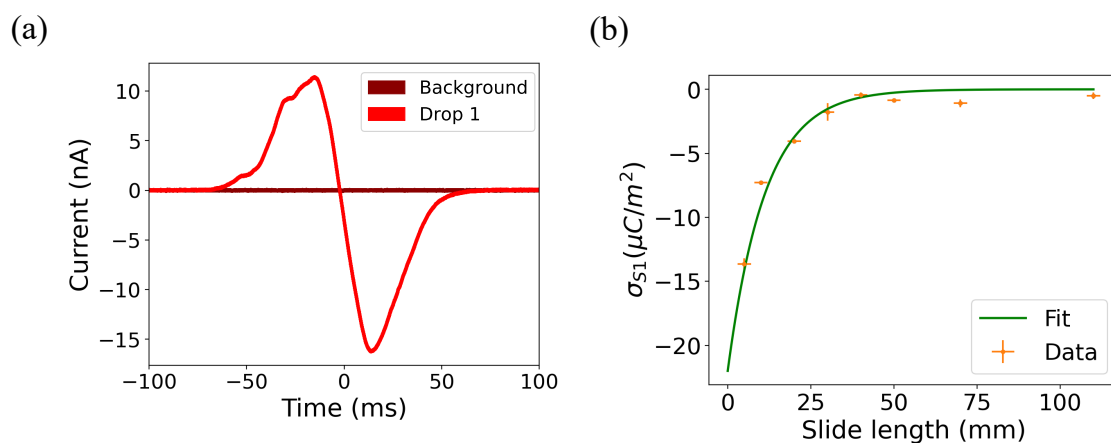


Figure 7.7: (a) The positive peak and negative curve represent the current flowing towards and away from the ground, respectively. (b) The first drop surface charge distribution. The green curve shows the fit. $L_{\text{sat}} = (1.1 \pm 0.1)$ cm is the decay length obtained from the fit.

The quantitative measurement of σ_{S1} shows that the majority of the charge transfer occurs at the beginning of the slide path, consistent with the assumption in a previous study [14]. As the drop slides down the surface, it accumulates more charge until the drop is fully charged. At the same time, the leftover surface charge decreases, as observed in the measurement. This can be described by an exponential decay of surface charge density as given by the equation

$$\sigma_{S1}(x) = \sigma_{out} e^{-\frac{x}{L_{\text{sat}}}}. \quad (7.8)$$

In figure 7.7b, the orange-colored points show the surface charge densities after the first drop at different slide lengths. The measured surface charge densities show an exponential decay, which decreases with increasing slide length. From the fit (green curve), we obtained the decay length $L_{\text{sat}} = 1.1 \pm 0.2$ cm. In order to check the consistency, we estimated the drop charge using the above values in (7.9).

$$Q_1 = -w\sigma_{out} \int_{x=0}^{x=15} e^{-\frac{x}{L_{\text{sat}}}} dx. \quad (7.9)$$

Here, we estimated the total charge of the first drop after sliding 15 cm to be 1.6 nC, which closely aligns with the saturation drop charge measured under the similar conditions as presented in the previous chapter.

7.4 Summary

In this chapter, We saw that by placing a control electrode beneath a hydrophobic substrate, we can measure the charge deposited by drops sliding down the surface. This approach is based on the principle of mirror charge detection, where we measure the capacitive current generated by the moving contact line. By analyzing the capacitive current of the grounded drop and comparing it to drop motion video, we have verified that the charge is deposited at the receding contact line. Furthermore, by comparing the deposited charge density behind a drop with the charge density inside the EDL, we have estimated the fraction of charge left on the surface to be around 20-50%.

Furthermore, we observed that a surface has the ability to retain residual charge, and the neutralization process is influenced by both the substrate and the environment. This neutralization process can be characterized by an exponential discharge time τ . These insights not only deepen our understanding of solid-liquid contact charge separation, but also have the potential to be utilized in improving solid-liquid nanogenerators by leveraging these effects.

Chapter 8

Conclusion & Outlook

Understanding slide electrification has been challenging due to its dependency on multiple parameters. In this dissertation, I approached the problem from two sides. First, the experimental side, where we designed two different setups. We used these experimental setups to quantify the drop charge/potential depending on slide length, drop interval, on the different hydrophobic surfaces, and the surface neutralization time. Second, building upon these experimental results, we addressed three research questions mentioned in the introduction to physically describe slide electrification. These questions included the origin of slide electrification from the EDL, the amount of charge left on the dry surface, and the charge retention and discharge by the surface. In the following, we will summarize the findings, contributions to the field, limitations of the methods and model, and provide an outlook for the project.

Origin of slide electrification from EDL: The question of the origin of charge separation has been widely debated, whether it is caused by electrons [40, 39, 20], ions [35, 34, 13], or a combination of both. However, there is well-established knowledge regarding the formation of surface charge and the EDL when a polar liquid comes into contact with a solid surface, supported by a theoretical background describing these processes [88, 89, 90, 63]. Additionally, there is increasing evidence of the involvement of surface chemistry [61] and the pH of the liquid in slide electrification [36, 39]. Hence, our goal in this work was to explore the correlation between the theory of the EDL and solid electrification.

Here, I developed experimental setups to quantify the charge of drops sliding atop a hydrophobic surface. We observed that the drop charge/potential increases with the slide length, saturating at a maximum drop charge/potential after a certain distance. We described this physical phenomenon as follows: Maximum charge separation occurs

as the neutral drop begins sliding down the substrate. As the drop potential increases, the charge separation decreases. When the drop charge/potential completely compensates for the surface charge/potential, the charge separation halts, and the drop reaches the saturation drop charge/potential, as observed in our experiments. Building on this understanding, I collaborated with Aaron D. Ratschow from TU Darmstadt to develop a model connecting the EDL with the slide electrification. We demonstrated that the charging of a sliding drop directly correlates with the surface charge at the solid-liquid interface. The potential that the drop achieves after reaching the saturation state is an amplified value of the surface potential/zeta potential [38]. The amplification depends on the ratio of the dielectrics and the thickness of the EDL and the substrate.

The relationship was derived under the assumption that the increasing drop potential does not significantly affect the surface, and the drop charge remains constant after a certain slide length. This saturation of drop charge was indeed experimentally observed. By measuring the drop charge/potential, the relationship postulated via theory was validated. The experimentally measured surface potential for a moderate pH of around 6 was found to be close to the zeta potential value measured using other techniques, such as laser Doppler velocimetry measurements [101]. This theoretical model and the experimental results help resolve the debate about what plays a major role in charge transfer. This work shows that the formation of the EDL and the absorption or desorption of ions play a vital role in charge separation.

Amount of surface charge left on the dry surface: After demonstrating that slide electrification originates from the EDL, we tackled the question: What percentage of the charge from the EDL is retained on the dry solid surface? In this chapter of the dissertation, I proposed a method to measure the amount of leftover charge as a grounded drop slides down the surface. The results revealed that the slide electrification occurs as the sliding drop dewets the solid surface and depends on both drop velocity and salt concentration.

The experimental results revealed two distinct velocity-dependent regimes. I collaborated with Aaron D. Ratschow to build a model describing the results, which were published recently [64]. In the low velocity regime, diffusion and advection do not significantly impact charge separation and the charge separation remain constant for a stable receding contact angle. However, with increased velocity, diffusion and advection become more pronounced, leading to a decrease in the deposited surface charge. Additionally, we observed a reduction in charge deposition with increasing salt concentration, likely attributed to the alteration of the EDL due to the presence of salt. This quantification provides easy access to the charge transfer coefficient and

could be utilized to quantify it for different surfaces. Understanding its dependency could help enhance or diminish charge separation in slide electrification.

Furthermore, our parametric study of slide electrification [64] has shown that the flow effect in the drop plays an important role in charge separation. One of these parameters is the receding contact angle. Theoretical models and numerical simulations reveal that the receding contact line play a significant role. Contact angles above 90° seem to leave more surface charge in comparison to hydrophilic surfaces. Numerical simulations even show that for very low contact angles and high velocity, we can expect an inverse charge separation. This means that the drop charge can flip after a certain velocity or slide length. We have observed a similar drop charge flip in another study [61]. In future, more elaborate experiments with different surface, contact angle, and velocity configurations could help verify or modify the presented theoretical model.

Surface charge retention and discharge: The experiments with image charge detection also revealed that the measured slide electrification depends on the drop number and the time between drops. We quantified this process by considering that the surface retains some of the charge left by the sliding drop for a certain time. This retained charge is discharged via an exponential discharge process [38, 69, 14].

We observed that the discharge time depends on the substrate, as well as the surrounding environmental conditions, such as the amount of ions in the atmosphere. Specifically, we quantified the surface discharge time and demonstrated that normal float glass substrate has a faster discharge time than float quartz substrate. This study also revealed that there is a slow relaxation of surface charge, which might be coming from the substrate polarization due to high drop potential. Further study of the involvement of the substrate is needed to fully quantify this process, and this experimental method could play an important role in such studies.

Combining all these findings, we were able to develop a physical model that includes the EDL, surface charge left on the surface, and its discharge time. The model incorporates all these parameters and describes slide electrification using simple equations that can be numerically solved. We observed that the model aligns well with the experimental results. Nevertheless, a possible breakdown of the model could occur in extreme pH conditions, where protonation or deprotonation might affect the equilibrium state. Similarly, conductivity and ionic polarization in the substrate might play a vital role and influence the drop charge and voltage. Future experiments could explore the limitations of the proposed model by conducting measurements with a pH sweep. Different surfaces could be used to understand the saturation drop charge and the factors affecting it.

Outlook & Open questions: The model we derived to describe the slide electrification is comprehensive but not yet complete. One of the effects observed in the experiments but not described by the theoretical model is the drop charge flipping with drop number, as presented in one of our publications [61] (see Fig. 8.2). Here, we used an N-(3-trimethoxysilylpropyl)diethylenetriamine (NTDET)-functionalized PFOTS surface, where we observed drop charge flip from positive to negative within a few drops. This raises several open questions, such as: Is there adaptation of the surface with longer exposure to water? Is the flipping caused by the local point of zero charge achieved due to charge separation? One way to understand such behaviour would be to conduct comprehensive molecular dynamics simulations of different surfaces in contact with water and study the molecular picture of charge separation. Investigation of the underlying physico-chemical processes involved will ultimately lead to a better understanding of the molecular origin of slide electrification.

A deeper understanding of model parameters such as the charge transfer coefficient and surface discharge time, coupled with an understanding of the model's limitations, could pave the way for designing devices that increase energy harvesting from sliding drops. Moreover, the simple relationship between drop charge/voltage and surface charge/potential as shown in this work could provide a straightforward method for measuring surface electrical properties, such as surface potential, of the surface in contact with liquids. This new insight into slide electrification holds the potential to transform the measurement methods in the thin film, coating, and biomembrane industries, offering a simpler and more cost-effective approach.

Bibliography

- [1] S. Pan and Z. Zhang, “Fundamental theories and basic principles of triboelectric effect: A review,” *Friction*, vol. 7, no. 1, pp. 2–17, 2019.
- [2] J. Lowell and A. Rose-Innes, “Contact electrification,” *Advances in Physics*, vol. 29, no. 6, pp. 947–1023, 1980.
- [3] M. Fowler, “Historical beginnings of theories of electricity and magnetism,” *Recuperado el*, vol. 23, no. 5, p. 2012, 1997.
- [4] S. Gray, “V. a letter to cromwell mortimer, md secr. rs containing several experiments concerning electricity by mr. stephen gray,” *Philosophical Transactions of the Royal Society of London*, vol. 37, no. 417, pp. 18–44, 1731.
- [5] C. A. Hausen, *Christiani Avgusti Havsensii Prof. Mathes. Ord. In Academ. Lipsiensis, Novi Profectus In Historia Electricitatis: Post Obitum Avctoris, Praematro Fato Nuper Exstincti, Ex Msto Eivs Editi. Praemissa Est Commemativncula De Vita Et Scriptis Viri, De Solidiori Doctrina Optime Meriti.* Schwan, 1743.
- [6] P. Lenard, “Über die electricität der wasserfälle,” *Ann. Phys*, vol. 46, pp. 584–636, 1892.
- [7] J. Nolan and J. Enright, “Experiments on the electrification produced by breaking up water, with special application to simpson’s theory of the electricity of thunderstorms,” in *Sci. Proc. R. Dublin Soc*, vol. 17, pp. 1–11, 1922.
- [8] E. F. Porter and J. Wyman Jr, “Contact potentials of stearate films on metal surfaces,” *Journal of the American Chemical Society*, vol. 60, no. 5, pp. 1083–1094, 1938.
- [9] E. F. Porter and J. Wyman Jr, “Further studies on the electrical properties of stearate films deposited on metal,” *Journal of the American Chemical Society*, vol. 60, no. 12, pp. 2855–2869, 1938.

- [10] I. Langmuir, “Surface electrification due to the recession of aqueous solutions from hydrophobic surfaces,” *Journal of the American Chemical Society*, vol. 60, no. 5, pp. 1190–1194, 1938.
- [11] W. R. Harper, *Contact and frictional electrification*. Clarendon P., 1967.
- [12] F. Galembeck and T. A. Burgo, *Chemical electrostatics*. Springer, 2017.
- [13] L. S. McCarty and G. M. Whitesides, “Electrostatic charging due to separation of ions at interfaces: contact electrification of ionic electrets,” *Angewandte Chemie International Edition*, vol. 47, no. 12, pp. 2188–2207, 2008.
- [14] A. Z. Stetten, D. S. Golovko, S. A. Weber, and H.-J. Butt, “Slide electrification: charging of surfaces by moving water drops,” *Soft matter*, vol. 15, no. 43, pp. 8667–8679, 2019.
- [15] T. A. Burgo, F. Galembeck, and G. H. Pollack, “Where is water in the triboelectric series?,” *Journal of Electrostatics*, vol. 80, pp. 30–33, 2016.
- [16] K. Yatsuzuka, Y. Mizuno, and K. Asano, “Electrification phenomena of pure water droplets dripping and sliding on a polymer surface,” *Journal of electrostatics*, vol. 32, no. 2, pp. 157–171, 1994.
- [17] K. Yatsuzuka, Y. Higashiyama, and K. Asano, “Electrification of polymer surface caused by sliding ultrapure water,” *IEEE Transactions on Industry Applications*, vol. 32, no. 4, pp. 825–831, 1996.
- [18] M. Matsui, N. Murasaki, K. Fujibayashi, P. Y. Bao, and Y. Kishimoto, “Electrification of pure water flowing down a trough set up with a resin sheet,” *Journal of electrostatics*, vol. 31, no. 1, pp. 1–10, 1993.
- [19] V. Yaminsky and M. Johnston, “Static electrification by nonwetting liquids. contact charging and contact angles,” *Langmuir*, vol. 11, no. 10, pp. 4153–4158, 1995.
- [20] S. Lin, L. Xu, A. C. Wang, and Z. L. Wang, “Quantifying electron-transfer in liquid-solid contact electrification and the formation of electric double-layer,” *Nature communications*, vol. 11, no. 1, pp. 1–8, 2020.
- [21] D. Choi, H. Lee, I. S. Kang, G. Lim, D. S. Kim, K. H. Kang, *et al.*, “Spontaneous electrical charging of droplets by conventional pipetting,” *Scientific reports*, vol. 3, p. 2037, 2013.
- [22] J. Nauruzbayeva, Z. Sun, A. Gallo Jr, M. Ibrahim, J. C. Santamarina, and H. Mishra, “Electrification at water–hydrophobe interfaces,” *Nature communications*, vol. 11, no. 1, p. 5285, 2020.

- [23] P. C. L. Kwok, S. J. Trietsch, M. Kumon, and H.-K. Chan, “Electrostatic charge characteristics of jet nebulized aerosols,” *Journal of aerosol medicine and pulmonary drug delivery*, vol. 23, no. 3, pp. 149–159, 2010.
- [24] W. Hu, Z. Gao, X. Dong, J. Chen, and B. Qiu, “Contact electrification of liquid droplets impacting living plant leaves,” *Agronomy*, vol. 14, no. 3, p. 573, 2024.
- [25] D. Chate and A. Kamra, “Charge separation associated with splashing of water drops on solid surfaces,” *Atmospheric research*, vol. 29, no. 1-2, pp. 115–128, 1993.
- [26] J. Thomson, “Xxxi. on the electricity of drops,” *The London, Edinburgh, and Dublin Philosophical Magazine and Journal of Science*, vol. 37, no. 227, pp. 341–358, 1894.
- [27] Z. Levin and P. V. Hobbs, “Splashing of water drops on solid and wetted surfaces: hydrodynamics and charge separation,” *Philosophical Transactions of the Royal Society of London. Series A, Mathematical and Physical Sciences*, vol. 269, no. 1200, pp. 555–585, 1971.
- [28] N. Miljkovic, D. J. Preston, R. Enright, and E. N. Wang, “Electrostatic charging of jumping droplets,” *Nature Communications*, vol. 4, pp. 1 – 9, 2013.
- [29] H. Wu, N. Mendel, D. van den Ende, G. Zhou, and F. Mugele, “Energy harvesting from drops impacting onto charged surfaces,” *Physical review letters*, vol. 125, no. 7, p. 078301, 2020.
- [30] D. I. Diaz, D. G. González, P. Bista, S. Weber, H.-J. Butt, A. Z. Stetten, and M. Kappl, “Charging of impacting drops onto superhydrophobic surfaces,” *Soft Matter*, 2022.
- [31] D. Díaz, X. Li, P. Bista, X. Zhou, F. Darvish, H.-J. Butt, and M. Kappl, “Self-generated electrostatic forces of drops rebounding from hydrophobic surfaces,” *Physics of Fluids*, vol. 35, no. 1, 2023.
- [32] K. N. Kudin and R. Car, “Why are water- hydrophobic interfaces charged?,” *Journal of the American Chemical Society*, vol. 130, no. 12, pp. 3915–3919, 2008.
- [33] V. Artemov, L. Frank, R. Doronin, P. Stärk, A. Schlaich, A. Andreev, T. Leisner, A. Radenovic, and A. Kiselev, “The three-phase contact potential difference modulates the water surface charge,” *The Journal of Physical Chemistry Letters*, 2023.

- [34] R. Zimmermann, N. Rein, and C. Werner, “Water ion adsorption dominates charging at nonpolar polymer surfaces in multivalent electrolytes,” *Physical Chemistry Chemical Physics*, vol. 11, no. 21, pp. 4360–4364, 2009.
- [35] M. D. Sosa, M. L. M. Ricci, L. L. Missoni, D. H. Murgida, A. Cánneva, N. B. D’Accorso, and R. M. Negri, “Liquid–polymer triboelectricity: chemical mechanisms in the contact electrification process,” *Soft Matter*, vol. 16, no. 30, pp. 7040–7051, 2020.
- [36] M. D. Sosa, N. B. D’Accorso, M. L. Martínez Ricci, and R. M. Negri, “Liquid–polymer contact electrification: Modeling the dependence of surface charges and ξ -potential on pH and added-salt concentration,” *Langmuir*, vol. 38, no. 29, pp. 8817–8828, 2022.
- [37] L. E. Helseth, “Ion concentration influences the charge transfer due to a water–air contact line moving over a hydrophobic surface: Charge measurements and theoretical models,” *Langmuir*, vol. 39, no. 5, pp. 1826–1837, 2023.
- [38] P. Bista, A. D. Ratschow, H.-J. Butt, and S. A. Weber, “High voltages in sliding water drops,” *The Journal of Physical Chemistry Letters*, vol. 14, pp. 11110–11116, 2023.
- [39] J. Nie, Z. Ren, L. Xu, S. Lin, F. Zhan, X. Chen, and Z. L. Wang, “Probing contact-electrification-induced electron and ion transfers at a liquid–solid interface,” *Advanced Materials*, vol. 32, no. 2, p. 1905696, 2020.
- [40] J. Zhang, S. Lin, M. Zheng, and Z. L. Wang, “Triboelectric nanogenerator as a probe for measuring the charge transfer between liquid and solid surfaces,” *ACS nano*, vol. 15, no. 9, pp. 14830–14837, 2021.
- [41] A. Shahzad, K. R. Wijewardhana, and J.-K. Song, “Contact electrification efficiency dependence on surface energy at the water-solid interface,” *Applied Physics Letters*, vol. 113, no. 2, p. 023901, 2018.
- [42] L. E. Helseth, “Electrical energy harvesting from water droplets passing a hydrophobic polymer with a metal film on its back side,” *Journal of Electrostatics*, vol. 81, no. C, pp. 64 – 70, 2016.
- [43] L. Zhao, L. Liu, X. Yang, H. Hong, Q. Yang, J. Wang, and Q. Tang, “Cumulative charging behavior of water droplet driven freestanding triboelectric nanogenerators toward hydrodynamic energy harvesting,” *Journal of Materials Chemistry A*, vol. 8, no. 16, pp. 7880–7888, 2020.
- [44] N. Miljkovic, D. J. Preston, R. Enright, and E. N. Wang, “Jumping-droplet electrostatic energy harvesting,” *Applied Physics Letters*, vol. 105, pp. 013111 – 6, 2014.

- [45] L. Yang, Y. Wang, Y. Guo, W. Zhang, and Z. Zhao, “Robust working mechanism of water droplet-driven triboelectric nanogenerator: Triboelectric output versus dynamic motion of water droplet,” *Advanced Materials Interfaces*, vol. 6, no. 24, p. 1901547, 2019.
- [46] L. E. Helseth and X. D. Guo, “Contact Electrification and Energy Harvesting Using Periodically Contacted and Squeezed Water Droplets,” *Langmuir*, vol. 31, pp. 3269 – 3276, 2015.
- [47] Y. Sun, X. Huang, and S. Soh, “Using the gravitational energy of water to generate power by separation of charge at interfaces,” *Chemical science*, vol. 6, no. 6, pp. 3347–3353, 2015.
- [48] L. E. Helseth, “A water droplet-powered sensor based on charge transfer to a flow-through front surface electrode,” *Nano Energy*, vol. 73, p. 104809, 2020.
- [49] W. Xu, H. Zheng, Y. Liu, X. Zhou, C. Zhang, Y. Song, X. Deng, M. Leung, Z. Yang, R. X. Xu, *et al.*, “A droplet-based electricity generator with high instantaneous power density,” *Nature*, vol. 578, no. 7795, pp. 392–396, 2020.
- [50] J. Niu, W. Xu, K. Tian, G. He, Z. Huang, and Q. Wang, “Triboelectric energy harvesting of the superhydrophobic coating from dropping water,” *Polymers*, vol. 12, no. 9, p. 1936, 2020.
- [51] H. Wu, N. Mendel, S. van Der Ham, L. Shui, G. Zhou, and F. Mugele, “Charge trapping-based electricity generator (cteg): an ultrarobust and high efficiency nanogenerator for energy harvesting from water droplets,” *Advanced materials*, vol. 32, no. 33, p. 2001699, 2020.
- [52] M. Sun, X. Wang, L. R. Winter, Y. Zhao, W. Ma, T. Hedtke, J.-H. Kim, and M. Elimelech, “Electrified membranes for water treatment applications,” *ACS ES&T Engineering*, vol. 1, no. 4, pp. 725–752, 2021.
- [53] J. K. Holt, H. G. Park, Y. Wang, M. Stadermann, A. B. Artyukhin, C. P. Grigoropoulos, A. Noy, and O. Bakajin, “Fast mass transport through sub-2-nanometer carbon nanotubes,” *Science*, vol. 312, no. 5776, pp. 1034–1037, 2006.
- [54] B. Grosjean, M.-L. Bocquet, and R. Vuilleumier, “Versatile electrification of two-dimensional nanomaterials in water,” *Nature communications*, vol. 10, no. 1, p. 1656, 2019.
- [55] V. R. Stamenkovic, D. Strmcnik, P. P. Lopes, and N. M. Markovic, “Energy and fuels from electrochemical interfaces,” *Nature materials*, vol. 16, no. 1, pp. 57–69, 2017.

- [56] J. Dong, S. Huang, J. Luo, J. Zhao, F. R. Fan, and Z.-Q. Tian, “Supercapacitor-inspired triboelectric nanogenerator based on electrostatic double layer,” *Nano Energy*, vol. 95, p. 106971, 2022.
- [57] M. Feng, X. Kong, Y. Feng, X. Li, N. Luo, L. Zhang, C. Du, and D. Wang, “A new reversible thermosensitive liquid–solid teng based on a p (nipam-*mma*) copolymer for triboelectricity regulation and temperature monitoring,” *Small*, vol. 18, no. 21, p. 2201442, 2022.
- [58] H. Shen, H. Lei, M. Gu, S. Miao, Z. Gao, X. Sun, L. Sun, G. Chen, H. Huang, L. Chen, *et al.*, “A wearable electrowetting on dielectrics sensor for real-time human sweat monitor by triboelectric field regulation,” *Advanced Functional Materials*, vol. 32, no. 34, p. 2204525, 2022.
- [59] X. Li, F. Bodziony, M. Yin, H. Marschall, R. Berger, and H.-J. Butt, “Kinetic drop friction,” *Nature communications*, vol. 14, no. 1, p. 4571, 2023.
- [60] L. E. Helseth, “The influence of microscale surface roughness on water-droplet contact electrification,” *Langmuir*, vol. 35, no. 25, pp. 8268–8275, 2019.
- [61] W. S. Wong, P. Bista, X. Li, L. Veith, A. Sharifi-Aghili, S. A. Weber, and H.-J. Butt, “Tuning the charge of sliding water drops,” *Langmuir*, 2022.
- [62] L. R. W. Robert J. Hunter, *Foundations of Colloid Science, Volume 1*. Weinheim: Clarendon, 1987.
- [63] H.-J. Butt, K. Graf, and M. Kappl, *Physics and Chemistry of Interfaces*. Weinheim: Wiley-VCH, 1., auflage, neue ausg ed., 2006.
- [64] A. D. Ratschow, L. S. Bauer, P. Bista, S. A. Weber, H.-J. Butt, and S. Hardt, “How charges separate when surfaces are dewetted,” *Physical Review Letters*, vol. 132, no. 22, p. 224002, 2024.
- [65] R. A. Jacobs and R. F. Probstein, “Two-dimensional modeling of electroremediation,” *AIChE journal*, vol. 42, no. 6, pp. 1685–1696, 1996.
- [66] R. J. Hunter, *Zeta potential in colloid science: principles and applications*, vol. 2. Academic press, 2013.
- [67] G. Gonella, E. H. Backus, Y. Nagata, D. J. Bonthuis, P. Loche, A. Schlaich, R. R. Netz, A. Kühnle, I. T. McCrum, M. T. Koper, *et al.*, “Water at charged interfaces,” *Nature Reviews Chemistry*, vol. 5, no. 7, pp. 466–485, 2021.
- [68] Q. T. Nguyen, C. P. Vo, T. H. Nguyen, and K. K. Ahn, “A direct-current triboelectric nanogenerator energy harvesting system based on water electrification for self-powered electronics,” *Applied Sciences*, vol. 12, no. 5, p. 2724, 2022.

- [69] P. Bista, A. D. Ratschow, A. Z. Stetten, H.-J. Butt, and S. A. Weber, “Surface charge density and induced currents by self-charging drops,” *Soft Matter*, 2024.
- [70] D. Tabor and D. Tabor, *Gases, liquids and solids: and other states of matter*. Cambridge university press, 1991.
- [71] H. Margenau, “Van der waals forces,” *Reviews of Modern Physics*, vol. 11, no. 1, p. 1, 1939.
- [72] G. C. Pimentel, *The hydrogen bond*. Reinhold Pub, 1960.
- [73] P. Chuchvalec, “Hans-jürgen butt, karlheinz graf, michael kappl: Physics and chemistry of interfaces,” *Chemické listy*, vol. 107, no. 7, 2013.
- [74] V. K. Khanna, *Introductory Nanoelectronics: Physical Theory and Device Analysis*. CRC Press, 2020.
- [75] N. Vargaftik, B. Volkov, and L. Voljak, “International tables of the surface tension of water,” *Journal of Physical and Chemical Reference Data*, vol. 12, no. 3, pp. 817–820, 1983.
- [76] G. Løvoll, Y. Méheust, K. J. Måløy, E. Aker, and J. Schmittbuhl, “Competition of gravity, capillary and viscous forces during drainage in a two-dimensional porous medium, a pore scale study,” *Energy*, vol. 30, no. 6, pp. 861–872, 2005.
- [77] J. W. Gibbs, “A method of geometrical representation of the thermodynamic properties by means of surfaces,” *Transactions of Connecticut Academy of Arts and Sciences*, pp. 382–404, 1873.
- [78] T. Young, “Iii. an essay on the cohesion of fluids,” *Philosophical transactions of the royal society of London*, no. 95, pp. 65–87, 1805.
- [79] W. S. Wong, L. Hauer, A. Naga, A. Kaltbeitzel, P. Baumli, R. Berger, M. D ‘Acunzi, D. Vollmer, and H.-J. Butt, “Adaptive wetting of polydimethylsiloxane,” *Langmuir*, vol. 36, no. 26, pp. 7236–7245, 2020.
- [80] R. Shuttleworth and G. Bailey, “The spreading of a liquid over a rough solid,” *Discussions of the Faraday Society*, vol. 3, pp. 16–22, 1948.
- [81] D. Pilat, P. Papadopoulos, D. Schaffel, D. Vollmer, R. Berger, and H.-J. Butt, “Dynamic measurement of the force required to move a liquid drop on a solid surface,” *Langmuir*, vol. 28, no. 49, pp. 16812–16820, 2012.
- [82] C. Huh and S. Mason, “Effects of surface roughness on wetting (theoretical),” *Journal of colloid and interface science*, vol. 60, no. 1, pp. 11–38, 1977.

- [83] A. H. Dourado, “Electric double layer: The good, the bad, and the beauty,” *Electrochem*, vol. 3, no. 4, pp. 789–808, 2022.
- [84] J. Lyklema, *Fundamentals of interface and colloid science: soft colloids*, vol. 5. Elsevier, 2005.
- [85] S. Chen, H. Dong, and J. Yang, “Surface potential/charge sensing techniques and applications,” *Sensors*, vol. 20, no. 6, p. 1690, 2020.
- [86] A. J. Bard, L. R. Faulkner, and H. S. White, *Electrochemical methods: fundamentals and applications*. John Wiley & Sons, 2022.
- [87] G. Gouy, “J. physicuq (4) 9, 457 (1910),” *Ann. d. phys.(9)*, vol. 7, p. 129, 1917.
- [88] D. L. Chapman, “Li. a contribution to the theory of electrocapillarity,” *The London, Edinburgh, and Dublin philosophical magazine and journal of science*, vol. 25, no. 148, pp. 475–481, 1913.
- [89] O. Stern, “The theory of the electrolytic double-layer,” *Z. Elektrochem*, vol. 30, no. 508, pp. 1014–1020, 1924.
- [90] D. C. Grahame, “The electrical double layer and the theory of electrocapillarity,” *Chemical reviews*, vol. 41, no. 3, pp. 441–501, 1947.
- [91] D. J. Griffiths, “Introduction to electrodynamics,” 2005.
- [92] B. N. Taylor, P. J. Mohr, and M. Douma, “The nist reference on constants, units, and uncertainty,” *available online from: physics.nist.gov/cuu/index*, 2007.
- [93] C. Moore and B. Vonnegut, “Measurements of the electrical conductivities of air over hot water,” *Journal of Atmospheric Sciences*, vol. 45, no. 5, pp. 885–890, 1988.
- [94] V. T. Paiva, L. P. Santos, D. S. da Silva, T. A. Burgo, and F. Galembeck, “Conduction and excess charge in silicate glass/air interfaces,” *Langmuir*, vol. 35, no. 24, pp. 7703–7712, 2019.
- [95] A. Soffer and M. Folman, “Surface conductivity and conduction mechanisms on adsorption of vapours on silica,” *Transactions of the Faraday Society*, vol. 62, pp. 3559–3569, 1966.
- [96] R. Umezawa, M. Katsura, and S. Nakashima, “Electrical conductivity at surfaces of silica nanoparticles with adsorbed water at various relative humidities,” *e-Journal of Surface Science and Nanotechnology*, vol. 16, pp. 376–381, 2018.
- [97] G. Bazilevskaya, I. Usoskin, E. Flückiger, R. Harrison, L. Desorgher, R. Bütikofer, M. Krainev, V. Makhmutov, Y. I. Stozhkov, A. Svirzhevskaya,

- et al.*, “Cosmic ray induced ion production in the atmosphere,” *Space Science Reviews*, vol. 137, pp. 149–173, 2008.
- [98] S. H. Behrens and D. G. Grier, “The charge of glass and silica surfaces,” *The Journal of chemical physics*, vol. 115, no. 14, pp. 6716–6721, 2001.
- [99] E. J. van der Wouden, D. C. Hermes, J. G. E. Gardeniers, and A. van den Berg, “Directional flow induced by synchronized longitudinal and zeta-potential controlling ac-electrical fields,” *Lab on a chip*, vol. 6, no. 10, pp. 1300–1305, 2006.
- [100] M. Kowacz and G. H. Pollack, “Moving water droplets: The role of atmospheric CO_2 and incident radiant energy in charge separation at the air–water interface,” *The Journal of Physical Chemistry B*, vol. 123, no. 51, pp. 11003–11013, 2019.
- [101] P. Vogel, N. Möller, P. Bista, H.-J. Butt, B. Liebchen, and T. Palberg, “Charging of dielectric surfaces in contact with aqueous electrolyte: the influence of CO_2 ,” *Journal of the American Chemical Society*, vol. 144, no. 46, pp. 21080–21087, 2022.
- [102] B. J. Kirby and E. F. Hasselbrink Jr, “Zeta potential of microfluidic substrates: 1. theory, experimental techniques, and effects on separations,” *Electrophoresis*, vol. 25, no. 2, pp. 187–202, 2004.
- [103] B. J. Kirby and E. F. Hasselbrink Jr, “Zeta potential of microfluidic substrates: 2. data for polymers,” *Electrophoresis*, vol. 25, no. 2, pp. 203–213, 2004.
- [104] K. Yamada, S. Yoshii, S. Kumagai, I. Fujiwara, K. Nishio, M. Okuda, N. Matsukawa, and I. Yamashita, “High-density and highly surface selective adsorption of protein–nanoparticle complexes by controlling electrostatic interaction,” *Japanese journal of applied physics*, vol. 45, no. 5R, p. 4259, 2006.
- [105] W. A. Talavera-Pech, A. Esparza-Ruiz, P. Quintana-Owen, A. R. Vilchis-Nestor, C. Carrera-Figueiras, and A. Ávila-Ortega, “Effects of different amounts of aptes on physicochemical and structural properties of amino-functionalized mcm-41-msns,” *Journal of Sol-Gel Science and Technology*, vol. 80, pp. 697–708, 2016.
- [106] L. Ģērmane, L. Lapčinskis, M. Iesalnieks, and A. Šutka, “Surface engineering of pdms for improved triboelectrification,” *Materials Advances*, vol. 4, no. 3, pp. 875–880, 2023.
- [107] X. Li, P. Bista, A. Z. Stetten, H. Bonart, M. T. Schür, S. Hardt, F. Bodziony, H. Marschall, A. Saal, X. Deng, *et al.*, “Spontaneous charging affects the motion of sliding drops,” *Nature Physics*, pp. 1–7, 2022.

-
- [108] L. Helseth, “Harvesting energy from light and water droplets by covering photovoltaic cells with transparent polymers,” *Applied Energy*, vol. 300, p. 117394, 2021.
- [109] A. Dörr and S. Hardt, “Electric-double-layer structure close to the three-phase contact line in an electrolyte wetting a solid substrate,” *Physical Review E*, vol. 86, no. 2, p. 022601, 2012.
- [110] V. Vitagliano and P. A. Lyons, “Diffusion coefficients for aqueous solutions of sodium chloride and barium chloride,” *Journal of the American Chemical Society*, vol. 78, no. 8, pp. 1549–1552, 1956.

List of Figures

1.1	Experimental illustration of the flying boy experiment conducted by Stephan Gray [5]	3
1.2	Two different types of energy harvesting methods using slide electrification. (a) The figure illustrates a way to harvest electric energy in the form of induced current. (b) The figure demonstrates a method to harvest electric current by directly discharging the drop.	6
1.3	Illustration showing the gap in knowledge	8
2.1	(a) Graphical illustration of surface tension (b) Empirical law to obtain surface tension	12
2.2	(a) Illustration of principal radii in the case of a spherical object (b) a cylindrical object	13
2.3	Three different configuration of water drop in the nozzle according to the pressure difference	14
2.4	Ideal equilibrium contact angle of a sessile drop on a planar surface	15
2.5	(a) Contact angle of hydrophilic surface $\theta_c < 90^\circ$ (b) Contact angle of hydrophobic surface $\theta_c > 90^\circ$	16
2.6	Dynamic contact angle hysteresis of sliding drop with advancing contact angle θ_a is different from receding contact angle θ_r	18
2.7	Electric double layer (EDL) as described by Helmholtz and Gouy-Chapman model	19

2.8	Potential landscape for different salt concentrations assuming the surface potential of 50 mV	22
2.9	(a) Potential landscape in Stern model (b) potential landscape in Grahame model with Inner Helmholtz Layer (IHL) and Outer Helmholtz Layer(OHL)	23
2.10	The charge separation process representation, where L_{sat} represents the decay length $\alpha(Q_D)$ denotes the drop charge-dependent transfer coefficient, and τ signifies the surface discharge time.	25
3.1	(a) shows the illustration of transimpedance amplifier, (b) shows the frequency dependent amplitude response after using compensating capacitor C_F	30
3.2	Illustration of experimental setup	31
3.3	(a) Short-circuit current measured as the probe electrode discharges the sliding drop, and (b) drop-surface is the contact time.	32
3.4	(a) Setup to measure the high drop voltage using capacitors in parallel. (b) Voltage measured as drop comes in contact with probe electrode.	34
3.5	Illustration of subsurface (mirror charge) measurement setup	35
3.6	Capacitive current and its corresponding drop position identified using high speed video. The capacitive current increases as the drop moves toward the probe electrode, and it changes the polarity as the drop moves away from the probe electrode.	36
3.7	(a) Illustration of sliding plate capacitor model (b) Induced capacitive current shows good agreement with the sliding plate capacitor model.	37
3.8	(a) Setup to measure the capacitance using the plate capacitor system. (b) Capacitive current caused by the 0-100V square potential.	38
4.1	Drop charge traces of 1 st 5 th 20 th and 200 th drop measured at different slide lengths. The experiments were done at tilt angle of 50°, IAB for 5 minutes before every experiment.	41

4.2	Stair experiment with changing Δt to study the drop charge dynamics in time measured at 15 cm slide length. The blue line serves as a guide for the eyes.	42
4.3	The drop charge on various surfaces coated on a glass substrate flips when the surface chemistry is altered. The figure is a modified version of the figure published by Wong et al. [61].	43
5.1	The circuit diagram describes the slide electrification model. The moving three-phase-contact line acts as a voltage source with a characteristic voltage U_{CL} , and internal resistance R_{int} , driving charges from the surface to the drop.	46
5.2	The illustration shows the electrostatic potential $\Psi(z)$ landscape in the proposed system. For an uncharged drop, the potential is flat throughout the substrate (dashed line). For a charged drop (solid line), there is an electric field present in the substrate, reducing the jump in the dielectric displacement and thereby amplifying the potential at the solid-liquid interface.	50
5.3	Comparison between the linear approximation and the full version of the equation shows that the approximation is valid within the uncertainty for low potentials, but deviates with increasing potential.	51
5.4	(a) Drop charge versus slide distance of the 1 st , 2 nd , and 100 th drop, plotted with an exponential fit to obtain characteristic saturation length $L_{sat} = 7.0 \pm 0.3$ mm. (b) Voltage measured at C_{in} for multiple drops. The first jump to 1 V is due to the drop discharge; the following linear increase comes from the ongoing charge separation during drop sliding. We can calculate the initial drop voltage using the scaling factor ($\frac{C_{in}}{C_D} = 1125$) to be 1.1 kV.	53
5.5	(a) Voltage comparison with different substrate thickness (b) Voltage U_D^{max} with increasing KNO_3 concentration	55
5.6	Surface potential of different hydrophobic surfaces	56

5.7	(a) Measured drop charge on PFOTS (dots) and numerical simulation (line) using the model. Parameters used for the simulation are $\Delta t = 1.8$ s, $C_D = 1.2$ pF, $\Phi = -40$ mV, and $\tau = 2.3$ s. (b) Steady-state drop charge (Q) vs. drop interval (Δt), and fit an exponential fit to obtain decay time	57
5.8	(a) Illustration of sliding drop with relevant length scales (b) Simulated drop charge traces of multiple drops	58
5.9	(a) Colour plot surface charge density (b) colour plot drop charge generated using numerical simulation	59
6.1	(a) Discharge current is measured by the direct drop discharge method, where the peak current represents the total accumulated drop charge, and the tail current represents the ongoing charge separation. (b) Voltage is measured in the external capacitor while touching the drop. The initial voltage jump represents the initial drop voltage, and the linear increase represents the ongoing charge separation.	63
6.2	(a) Fitting the discharge time to estimate input capacitor C_{in} . (b) Fitting the voltage signal to obtain U_D^{\max} and I_{mean}	64
6.3	(a) Transfer coefficient with increasing drop velocity for the grounded drop (1mM NaCl) aqueous solution. (b) Transfer coefficient with increasing Pe and the fit with Equation (6.8), where $\lambda_{sol} = 9.7$ nm [64], and $D = 1.6 \cdot 10^{-9}$ m ² /s [110].	66
6.4	(a) Transfer coefficient with increasing KNO ₃ concentration as compared to DI water. (b) Surface charge density in EDL with increasing salt concentration.	67
7.1	(a) Experimental setup to measure a capacitive current of sliding grounded drop. (b) Capacitive current of grounded drop sliding on top of the hydrophobic surface, and the modelled induced current using the model from section 3.2.4.	70

7.2	(a) Capacitive current induced by a grounded sliding drop on glass coated with various hydrophobic surfaces. (b) surface charge density σ , estimate integrating the current curves in (a). We observe that APTES has a positive surface charge density (positive current peak) whereas glass coated with PFOTS and PDMS has negative surface charge densities (negative peak).	71
7.3	(a) Measurement in float glass substrate. Steady-state $\Delta\sigma$ with increasing time between subsequent drops Δt . The first drop, with $\sigma_{in} = 0$, is represented by a blue point. Measured data is fitted using eq.(7.5) (b) Change in surface charge density, $\Delta\sigma$ (red dots) of PFOTS on float glass with increasing drop number and model (blue line). Parameters used for the modelling are $\sigma_{out} = -28 \frac{\mu C}{m^2}$, $\tau = 2.5$ s.	73
7.4	(a) Measurement in quartz glass substrate: Steady-state $\Delta\sigma$ with increasing time between drop Δt . The first drop (blue point) shows the $\Delta\sigma$ after the first drop as red dots shows the $\Delta\sigma$ at different Δt with ionizing air blower (IAB) running in the background. Black dots show $\Delta\sigma$ with increasing Δt but without IAB running in the background. (b) Measured $\Delta\sigma$ (red dots) and model (blue line) on PFOTS on quartz with $\sigma_{out} = -28 \frac{\mu C}{m^2}$, and discharge time of $\tau \approx 100$ s.	74
7.5	(a) Setup to measure capacitive current due to applied voltage (b) Current for 10 s while applying external potential of 200 V	75
7.6	Comparison of modified model with experimental observations	76
7.7	(a) The positive peak and negative curve represent the current flowing towards and away from the ground, respectively. (b) The first drop surface charge distribution. The green curve shows the fit. $L_{sat} = (1.1 \pm 0.1)$ cm is the decay length obtained from the fit.	77
8.1	Mean current at different velocities	99

- 8.2 Drop charge (dots) measured on PFOTS + NTDET. Here, drop charge polarity switches depending on both drop number and drop interval. Drops sliding on these surfaces at an interval of $\Delta t = 2$ s rapidly decrease in charge from +330 pC, down through 0 pC, eventually saturating at -55 pC for the 200th drop. This negative drop charge can be explained by amine groups on the NTDET molecules, which protonate upon water contact. Surprisingly, increasing Δt to 4 s flip the drop charge back to nearly 0 pC , and to +70 pC for $\Delta t = 16$ s. Returning Δt to 2 s at drop number 800 flips the drop charge back to the original negative saturation value of -55 pC. This drop-rate-dependent polarity-switching is impossible to explain within the existing drop charge model. 100

Appendix

Additional figures of chapter 6

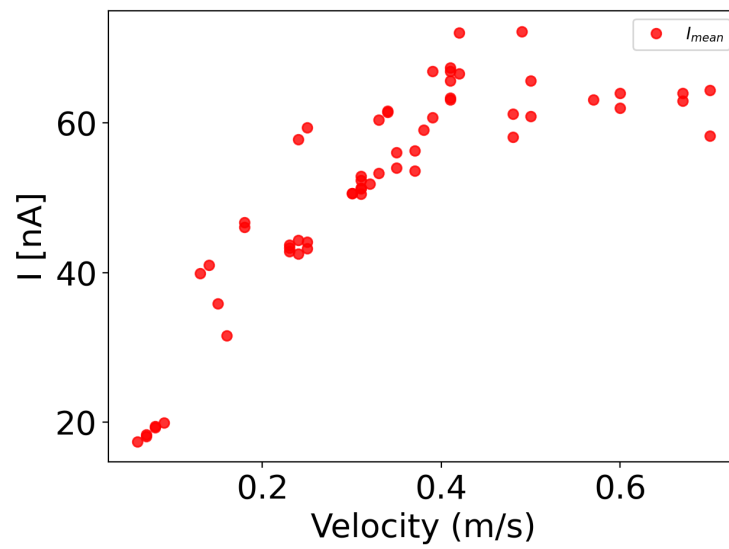


Figure 8.1: Mean current at different velocities

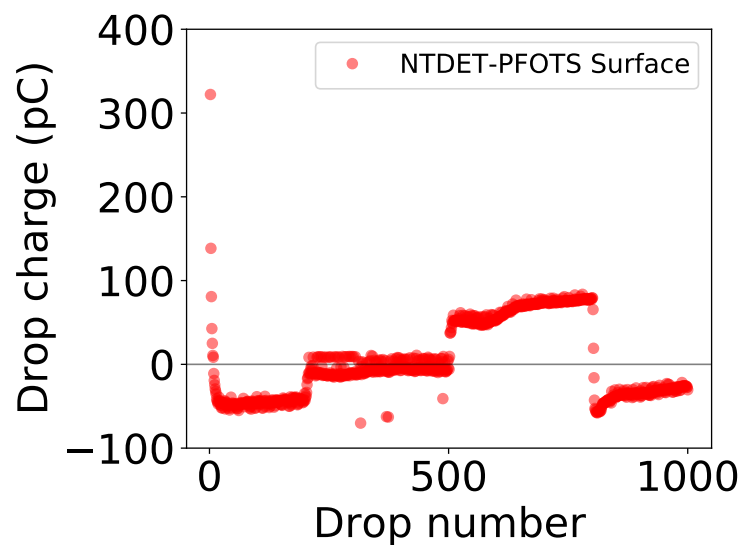


Figure 8.2: Drop charge (dots) measured on PFOTS + NTDET. Here, drop charge polarity switches depending on both drop number and drop interval. Drops sliding on these surfaces at an interval of $\Delta t = 2$ s rapidly decrease in charge from +330 pC, down through 0 pC, eventually saturating at -55 pC for the 200th drop. This negative drop charge can be explained by amine groups on the NTDET molecules, which protonate upon water contact. Surprisingly, increasing Δt to 4 s flip the drop charge back to nearly 0 pC, and to +70 pC for $\Delta t = 16$ s. Returning Δt to 2 s at drop number 800 flips the drop charge back to the original negative saturation value of -55 pC. This drop-rate-dependent polarity-switching is impossible to explain within the existing drop charge model.

Curriculum vitae



Pravash Bista

Personal Information

Date of Birth: March 22, 1992

Address: Bernhard-Winter-Str. 41, 55120 Mainz, Germany

Email: pravashbista@gmail.com

Working Experience

- **Doctoral Candidate:** MPI-Polymerforschung (2021 – Current)

Education

- **M.Sc in Physics:** Johannes-Gutenberg-Universität Mainz (2019 – 2021)
- **B.Sc in Physics:** Johannes-Gutenberg-Universität Mainz (2014 – 2019)
- **Language Course:** Goethe Zentrum Nepal and JGU Mainz (2011 – 2014)
- **School:** Kathmandu Bernhardt College Nepal (2011)

Publications

1. **Surface Charge Density and Induced Currents by Self-Charging Drops**, P Bista, AD Ratschow, AZ Stetten, HJ Butt, SAL Weber, 2024, *Soft Matter*
2. **High Voltages in Sliding Water Drops**, P Bista, AD Ratschow, HJ Butt, SAL Weber, 2023, *The Journal of Physical Chemistry Letters* 14 (49), 11110-11116
3. **How charges separate when surfaces are dewetted**, AD Ratschow, LS Bauer, P Bista, SAL Weber, HJ Butt, S Hardt, 2023, arXiv preprint arXiv:2305.02172
4. **Self-generated electrostatic forces of drops rebounding from hydrophobic surfaces**, *Soft matter* 18.8 (2022): 1628-1635 D Díaz, X Li, P Bista, X Zhou, F Darvish, HJ Butt, M Kappl, 2023, *Physics of Fluids* 35 (1)
5. **Charging of Dielectric Surfaces in Contact with Aqueous Electrolytes the Influence of CO₂**, P Vogel, P Bista, SAL Weber, HJ Butt et al., *Journal of the American Chemical Society* 144.46 (2022): 21080-21087.
6. **Spontaneous charging affects the motion of sliding drops**, X Li, P Bista, AZ Stetten, H Bonart, MT Schür, S Hardt, F Bodziony, et al., 2022, *Nature Physics* 18 (6), 713-719
7. **Tuning the charge of sliding water drops**, WSY Wong, P Bista, X Li, L Veith, A Sharifi-Aghili, SAL Weber, HJ Butt, 2022, *Langmuir* 38 (19), 6224-6230
8. **Charging of drops impacting onto superhydrophobic surfaces**, D Díaz, D Garcia-Gonzalez, P Bista, SAL Weber, HJ Butt, A Stetten, et al., 2022, *Soft Matter* 18 (8), 1628-1635

Symposiums and Conferences

- **Using Artificial Intelligence in Academia**, Max-Planck-Institut für Polymerforschung Group Retreat, Hirschegg, Austria (2023)
- **Solid-Liquid Contact Charge Separation and its Consequences**, Materials Research Society (MRS), Boston, USA (2022)
- **Adaptive two capacitor model to describe slide electrification in moving water drops**, DPG-Tagung der Sektion Kondensierte Materie (2022)
- **Sensing Ultra Low Electric Current**, Max-Planck-Institut für Polymerforschung Group Retreat, Berlin, Germany (2021)

Languages

- **Nepali:** Fluent
- **German:** Advanced
- **English:** Advanced
- **Hindi:** Intermediate